UWB FMCW Radar for Concealed Weapon Detection: RF front-end development

Thesis submitted for the Master of Science in Electrical Engineering, Telecommunications Track

Author: Eugenio Pasqua, student number: 1399136

Supervisor: Prof. Dr. Sci. A.G. Yarovoy

Daily Supervisor: Dr. Ir. T.G. Savelyev

2010-2011

TU Delft

Faculty of Electrical Engineering, Mathematics and Computer Science

Delft University of Technology

UWB FMCW Radar for Concealed Weapon Detection: RF front-end development

THESIS

submitted in partial fulfillment of the requirements for degree of

MASTER OF SCIENCE

in

ELECTRICAL ENGINEERING, TELECOMMUNICATIONS TRACK

by

Eugenio Pasqua,
student number: 1399136

February 8th, 2012

This work has been performed at:
Microwave Technology & Systems for Radar Section
Department of Telecommunications
Faculty of Electrical Engineering, Mathematics and Computer Science
Delft University of Technology

Delft University of Technology

DELFT UNIVERSITY OF TECHNOLOGY
DEPARTMENT OF TELECOMMUNICATIONS

The undersigned, hereby, certify that they have read and recommend to the Faculty of Electrical Engineering, Mathematics and Computer Science for acceptance the thesis entitled "**UWB FMCW Radar for concealed weapon detection: RF-front-end development**" by **Eugenio Pasqua** in partial fulfillment of the requirements for the degree of **Master of Science**.

Dated: February 8th, 2012

Committee Members:

Prof.dr.sci. A.G. Yarovoy

Dr. Ir. T.G. Savelyev

Dr. Ir. G. J.M. Janssen

Abstract

In recent years, the escalation of terroristic threats has caused an increase of security measures at sensible locations like airports and government buildings. Current methods for concealed weapon detection are either ineffective, slow or bulky, limiting their use mainly to security checkpoints. A fast imaging system for Concealed Weapon Detection implemented as a mobile gate, or in general as an easily transportable device, is considered as an ideal solution for fast screening of people at mass events.

In this thesis report, the design of an UWB MIMO 2-D array-based Microwave Radar Imaging system based on a RF-multichannel scheme is presented. Requirements of the design are low power emission and minimization of data acquisition time, cost and complexity. UWB technology is used to obtain high resolution, while MIMO technique helps reducing the number of required antennas in the 2-D array without a net degradation of performance. The final RF-scheme was selected based on the availability of commercially off-the-shelves RF-components.

The performance of the selected RF front-end was evaluated both via mathematical analysis and ADS simulations. The results of the simulations showed that by proper selection and positioning of filter in the basic RF-scheme, it is possible to achieve satisfactory performances in terms of harmonic suppression, detectability of targets and down-range resolution.

Acknowledgements

Hereby, I would like to express my deepest gratitude to a number of people, who supported and helped me in the realization of this thesis work.

First of all, I would like to thank my daily supervisor, Dr. Ir. Timofey Savelyev, for his guidance, support and encouragement. He was always available to listen to my doubts and to give me advice, both on the technical and organizational points of view, and thanks to the enormous patience he had during these months, he helped me get through the difficulties encountered during this thesis work.

Secondly, I would like to thank my supervisor, prof. dr. sci. Alexander Yarovoy, for giving me the opportunity to work at the MTS-R department and for his precious advice and support. His deep knowledge and experience in the subject has been an invaluable asset for the completion of this thesis project.

A special thank goes to Pascal Aubry, Dani Tran and Paul Hakkart, who helped me with many practical and theoretical issues.

My deepest gratitude goes also to the whole personnel of the Telecommunications department, where I felt a warm and friendly environment.

Last but not least, I'd like to thank my family and friends, who always supported me in the good and in the bad moments, and without whom I would have never been able to arrive at this point.

Table of Contents

Chapter 1: Introduction

Since the times of Galileo and van Leeuwenhoek, considered fathers of the telescope and microscope, respectively, man has been obsessed by the desire to see more clearly what was far way or what was very small. For centuries, efforts to capture visions beyond the range of the normal eye have long engaged scientists and engineers. In the 20th century, the development of the first photo camera and successively the discovery of X-rays were only the first of many achievements leading to the development of imaging devices which made possible what once would have been considered "magic", such as the recording of forms of light to which the human eye is essentially blind and the penetration of veils both around us and within us. Nowadays, imaging devices are used as precious supports in many fields (military, medical, security, meteorological, space exploration, etc…), and they affect us in all aspects of life.

In particular, radar has become one of the most ubiquitous of imaging technologies. Today, imaging radars are used to map the Earth and to reproduce weather patterns, they can provide pictures of other planets' and celestial objects' surfaces, and create images of objects buried in the ground, or hidden behind barriers.

One of the applications of imaging radars that has recently emerged is the detection and imaging of objects concealed on humans to improve the security of sensible locations like airport, banks, malls, etc…, due to the increasing threats ranging from the less dramatic knife and gun carriers to the hardened terrorists.

In this thesis report, we investigate the feasibility of an Imaging Radar System for concealed weapon detection, using Microwave Ultra-Wideband (UWB) technology, for fast screening of people flows at mass events. In this chapter, a general overview of the thesis report is given. In the first section, a brief introduction on the main research area of imaging radars is given, and the objectives of the thesis are stated. In section 1.2, a brief overview of state-of-the-art technologies for concealed weapon detection is given, with particular attention to active imaging radar systems. Section 1.3 describes the chosen approach to the research problem, addressing the challenges and the novelties of the thesis work. At last, the outline of the thesis is given in section 1.4.

1.1 Research problem description and objectives

In the last decade, the field of security systems for concealed weapon detection, with particular attention to imaging radars, has been one of the major focuses of the research performed at the department of Microwave Technology and Systems for Radar (MTS-R) of the faculty of Electrical Engineering, Mathematics, and Computer Engineering (EEMCS) at Delft University of Technology (TU Delft). Imaging radars are devices that measure the intensity and the round-trip time of electromagnetic waves that are emitted by the radar antenna system and reflected off a distant target or surface, producing an image whose structure reproduces on a definite scale the spatial arrangement of the target. The challenge in this field is the design of imaging systems that are reliable, safe and cost-effective with no privacy concerns.

Recently, MTS-R department joined the ATOM project (full title "*Airport detection and Tracking Of dangerous Materials by passive and active sensors arrays*"), supported through the European Commission's 7th Framework Programme as a capability project in the area of airport security. The objective of the ATOM project is to study, design and develop a functional prototype of an innovative multi-sensor based system, integrating active and passive radar sensors, with the purpose of improving security of both the terminal and gate areas of airports. The ATOM system will be a non-intrusive but pervasive security system, based on the integration of active and passive radar technology. MTS-R on behalf of TU Delft contributes to this project with the development of an ultra-wideband (UWB) radar technology that provides a high 3-D imaging capability and performs shape-based detection of concealed dangerous objects such as metallic weapons and explosive materials. The project started in 2009 and is currently in process.

Following the ongoing research on the ATOM project at the MTS-R department [5,6,7,8], this thesis project consists of a fundamental study of a mobile scanner and the design of a high-resolution radar sensor based on Microwave UWB technology with particular focus on the minimization of its cost and complexity in terms of electronics and number of antennas.

1.2 State-of-the-art Active Imaging Radars for concealed weapon detection

Currently, the state-of-the-art Active Imaging systems for concealed weapon detection mostly comprises imaging systems working with millimeter waves (MMW), implemented with two fundamentally different techniques, which are also suitable for microwave frequencies [18].

The first technique uses a focal-plane 2-D array placed at the focal point of a lens system, and operates in a manner analogous to optical video cameras. The scattered field is collected at the lens aperture, which focuses the RF energy into small volumes within its field of view. This makes it possible to scan image voxels (volume cells) in front of the lens, and to display a 3-D image in real-time. The major advantage of this technique is the relative compactness of the imaging system. On the other hand, focal-plane array imagers have a number of shortcomings, including a relatively low resolution, a small aperture due to practical constraints in the lens size, and a limited field of view, in addition to the high cost due to the 2-D array.

The other method, conceptually very similar to SAR, consists in a holographic radar imaging technique that allows reconstructing images of targets from data measured at different points of a 2-D aperture. A holographic radar includes a radar transceiver which is scanned over a rectilinear planar aperture to actively illuminate the target. The scattered field is measured coherently (both amplitude and phase of the scattered signal are recorded), and the acquired data are finally used to mathematically reconstruct a focused image of the target without the need for a lens. The stronger points of this technique are near-real time operation, large aperture size allowing a full body view of the person under surveillance, high resolution, and the ability to mathematically focus the reconstructed image at any single depth.

The millimeter-wave holographic-imaging technique has been extensively developed over the last two decades at the Pacific Northwest National Laboratory (PNNL), Richland, WA (USA), where several MMW holographic imaging systems, operating at different frequency bands from 10 to 120 GHz, have been built and tested [18,19,20,21,22].

Among others, they have developed an image-reconstruction algorithm that essentially merges the microwave holographic approach and the SAR approach to form 3-D images of the target from data collected over a 2-D aperture, with the use of a wide frequency bandwidth.

In [19] they show the advantages of wide-band holographic imaging over the single-frequency approach, by comparing the image quality of a 35 GHz single-frequency holographic imaging system with the same system converted to operate in the 27-33 GHz range. The system uses a linear array of sequentially switched antennas with a vertical scan. The array is made of an upper row of 64 transmit elements and a lower row of 64 receive antennas, yielding a horizontal aperture width of about 0.75 m. The array is mounted on a fast mechanical scanner which moves the array over a vertical aperture of 2 m, allowing gathering a full image data set over the entire 0.75x2 m aperture in less than 1 s.

In figure 1.1 are shown the holographic images of a man in front and back view, obtained with both the single-frequency (a and b) and the wideband (c and d) approaches. Wideband images have

a better quality than the single-frequency counterpart, which lacks of focus over many parts of the image. This can be explained by the fact that due to the close-range large-aperture operation, the single-frequency approach has a very short depth of field, which means that images of targets with significant depth, such as the human body, cannot be reconstructed in complete focus. On the contrary, with the wideband approach the use of a large frequency band dramatically improves the down-range resolution of the system, allowing the whole body to be in focus at the same time. In addition, wideband imaging also largely attenuates the effect of speckle, which is due to complex interference from varying reflection points on the target at different ranges, and is thus prevalent in single-frequency coherent imaging systems.

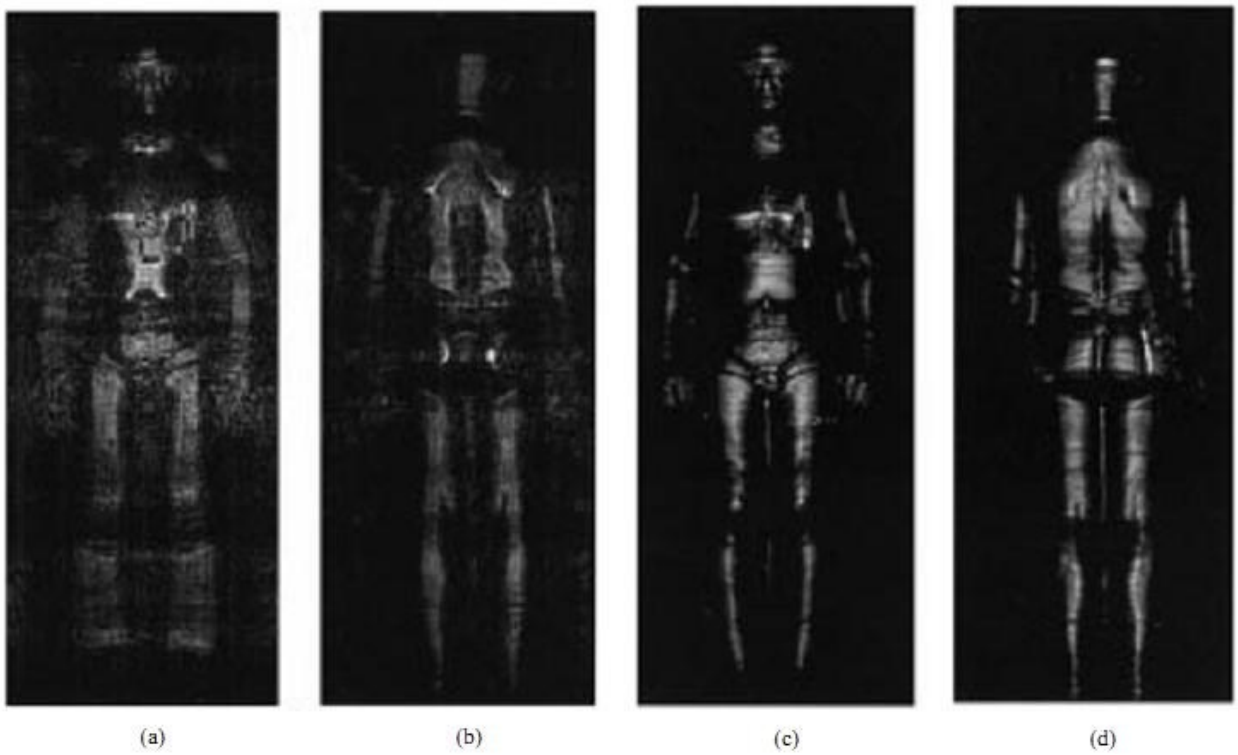

Figure 1.1: Comparison of Single-frequency (35 GHz) images of a man (a, b) and Wide-band (27–33 GHz) images of the same man (c, d), [18].

The MMW holographic imaging systems developed at PNNL have been extensively tested on personnel carrying weapon and other innocuous items, and their imaging results have confirmed how metallic weapons and innocuous items in general show up quite clearly in the images. Concealed threats fabricated with plastic materials such as C-4 explosives and plastic flare guns are also easily detectable in the images, although their reflectivity is lower than metallic items and the human body, and they appear less bright [20]. In [22], it was demonstrated that holographic imaging systems in the 10-20 GHz frequency band are also effective in the detection of biological and

chemical agents in envelopes and the detection and location of sealed containers concealed in body worn clothing fabricated with glass and plastic, which could contain harmful agents.

In [19] and [21] they also demonstrate how polarimetric imaging techniques can be employed to obtain additional information from the target. Polarization dependent reflections can be exploited for personnel screening by allowing differentiation of smooth features, such as the human body, from sharper features present in many concealed items. Additionally, imaging artifacts due to multipath can be identified and eliminated.

Recently, the researchers of PNNL have also developed a wideband holographic cylindrical imaging system which allows forming a complete 3-D reconstruction of the target, by inspecting the target from multiple angles. It uses a vertically oriented linear array scanned over a cylindrical aperture by a mechanical scanner, thus gathering data over the entire 360° around the target.

The cylindrical imaging technique has been licensed to L3-Communications Safeview which has produced a commercial system, ProVision body scanner; this system has already been deployed in some of the major USA and European airports as a checkpoint security system [26].

1.2.1 Other methods for Concealed Weapon Detection

Apart from radar imaging systems, several methods exist and are in use for concealed weapon detection and imaging.

Currently, most of personal screening security systems rely on metal detectors, which have been quite effective but suffer from a number of shortcomings. Metal detectors are able to detect only metal (or, in general, highly conductive) targets, but cannot distinguish an actual threat, like a gun or a knife, from innocuous items such as metal buttons, coins, keys, etc..., thus generating a rather high false alarm rate. Moreover, they are unable to detect non-metallic materials, thus being ineffective against modern threats such as plastic or ceramic weapons and explosives. Metal detectors are detection only systems, and thus provide poor information.

A more effective method to detect weapons concealed under a person's clothes consists in the use of X-Ray imaging systems. Recently, many airports in USA have installed whole body scanners based on X-ray imaging technology. Thanks to the very high frequencies involved, X-ray imagers have a very good spatial resolution, which allows identifying possible threat items of every type of material. These devices make use of low energy x-rays which penetrate a few millimeters into the body tissues, that is not enough to find objects hidden within body cavities or concealed under heavy flesh. However, X-ray imagers for personnel screening have raised some privacy issues, due to the highly detailed anatomical information contained in the images. This problem could be

overcome by altering or blurring parts of the image to hide such anatomical details, but this solution would very likely decrease the image quality and clarity, thus reducing the ability to identify small items and objects concealed in the blurred parts of the body. Moreover, there are also safety concerns due to the fact that x-ray radiation is ionizing. Although the intensity of emitted radiation is much lower than the amount believed to be a threat to health, there still remains preoccupation and distrust of this technology among the public.

A much safer method consists in the use of passive radar imagers. Passive systems do not use an illumination source, and thus they do not pose any health risk for the person being screened. As a matter of fact, a passive radar measures the electromagnetic radiation that is naturally emitted over a broad spectrum by all bodies, forming an image representing the intensity of this radiation. The intensity of the emitted radiation depends on the physical characteristics of the emitting body and its temperature.

At MMW frequencies, for example, the human body has a high emissivity due to its temperature. When a person is screened using a passive system in the MMW region, any concealed item would appear as a dark spot in the image, in contrast to the brighter background of the human body. This difference in brightness is due to the different intensity of the radiation emitted by the concealed item and the human body.

More recently, passive imagers have been realized also in the THz region, where many materials exhibit characteristic terahertz spectral features which can be used to identify them. This leads to the promise of direct detection of threat materials rather than simply inferring their possible presence by detecting an anomaly which has to be resolved through further, physical inspection.

Passive systems have shown their effectiveness in imaging concealed weapons, but their performance can drastically vary when used in different environments: in particular, in outdoor environments with large open space, the image quality is typically better than indoor, where it suffers from degradation due the higher intensity of background emissions.

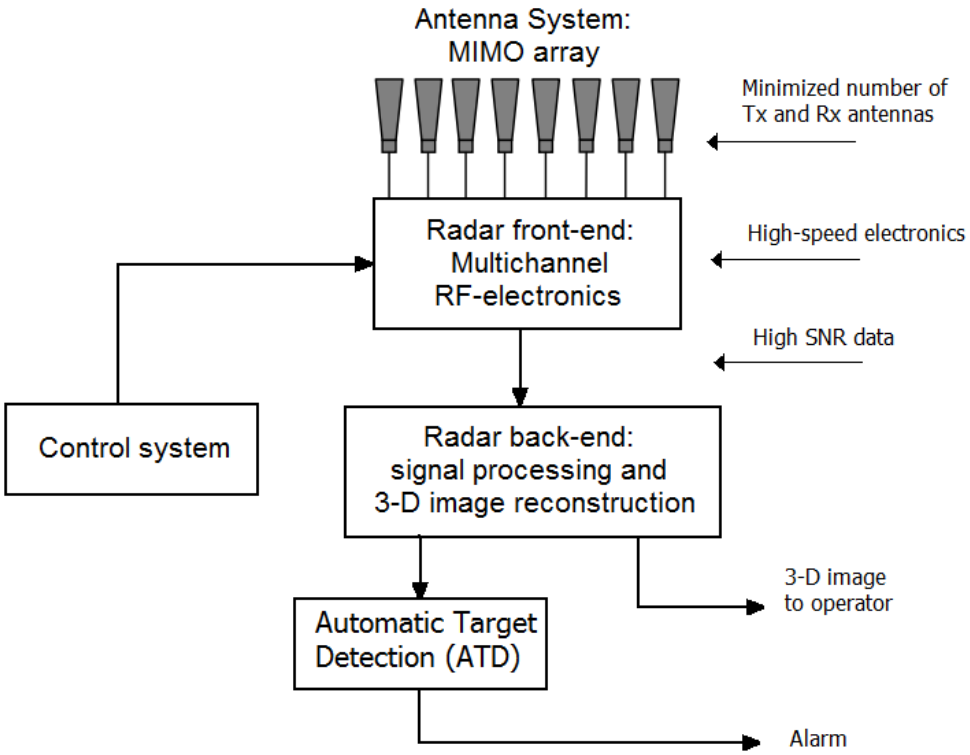

Figure 1.2: Block diagram of a complete radar imaging system.

1.3 Challenges, chosen approach and novelties

The design of imaging systems for security applications is a challenging task, which requires the fulfillment of demands which often go in opposite directions. The main challenge in this field is the design of imaging systems that are reliable, safe and cost-effective with no privacy concerns.

In terms of performances, the radar sensor must provide a fine resolution and a high signal-to-noise ratio for the processing stage, while achieving fast data acquisition and processing times for near-real time sensing of people flows. In particular, the down-range resolution should be high enough to distinguish reflections from a human body and an object attached to it, and to allow for target-shape recognition after the processing stage.

Fundamentally, the design of a complete imaging system is an interdisciplinary task that can be divided into four main parts:

- the antenna system, which must have low sidelobes/grating lobes;
- the radar front-end, that should provide a fine down-range resolution and a high dynamic range and signal-to-noise ratio for detection of strong and weak signals;

- the radar back-end, which should ensure a fast and efficient signal processing and imaging stage;
- the control system, with the task of providing the correct signals to drive the source and the switches;

However, the goal of this thesis is a fundamental study of a mobile scanner and the design of a microwave sensor based on UWB technology, with particular focus on the design of the radar front-end; design of antenna system, radar back-end and control system are not treated in this thesis project, although some assumptions on the antenna system have been be made to come to a proper design of the radar front-end.

In order to obtain the ultimate goals of this project, the first step was to perform a survey of state-of-the-art imaging systems for concealed weapon detection, in order to identify pros and cons of current imaging systems. From this, the need was clear for a safe and reliable imaging system which could achieve high performance and fast data acquisition time while minimizing its overall cost and complexity.

The use of UWB radar technology is crucial to ensure the satisfaction of safety and reliability requirements, thanks to its several advantages:

- high down-range resolution;
- capability of detection and classification;
- very low power radiation which is ideal for human body exposure;
- good coexistence with other existing instruments;
- robustness against interferences.

UWB radar technology has been used in different applications, from ground penetrating radars to medical imaging. Nowadays the state-of-the-art of UWB radar systems are array-based radar systems, either using the Synthetic Aperture Radar concept or an array with sequential operations of identical transmit/receive pairs. In spite of their relatively fast scanning speed and high cross-resolution capability, such systems can hardly fulfill the demand of real-time data acquisition and operation due to practical limitations.

The development of a UWB array-based real-aperture system with multiple-input multiple-output (MIMO) technique would help overcome these limitations, while reducing the element density in the array and decrease the overall cost of the system.

The main novelty of this thesis project consists in the design of a multichannel RF-scheme specifically optimized for a MIMO antenna array, with minimized data acquisition time and

complexity, and designed with the use of commercial off-the-shelves RF-components to keep the overall cost of the system to the minimum.

The final design has been evaluated in terms of performance, both by means of mathematical analysis and simulation with ADS, using real components specifications.

1.4 Overview of the thesis report

This thesis report is organized as follows. In chapter 2, the functional requirements of the UWB sensor for the selected application are discussed and some generic specifications are extrapolated. In particular, selection of appropriate frequency band and UWB technology are treated in this chapter. Successively, after a brief explanation of the theoretical concepts behind it, the number of elements required in the antenna array is estimated.

Chapter 3 begins with an overview of theoretical concepts of FMCW radars, before going into a more detailed analysis of the tradeoffs required to arrive to an optimal RF-scheme. Definitive selection of the multichannel RF-scheme is based on the availability of off-the-shelves RF-components, which were surveyed for this purpose.

Chapter 4 presents the performance estimation of the selected RF-scheme. This includes power analysis, noise analysis and estimation of power budget and dynamic range. A detection analysis for typical targets such as a handgun and a knife is also performed.

In chapter 5, the final multichannel RF-Scheme is simulated with microwave circuit simulator ADS^{TM}. The purpose of the simulation is to investigate the influence of harmonics generated by the radar electronics on the beat signal, and the detectability of typical targets on the background of human body reflections. Verification of down-range resolution of the radar system is also performed via ADS simulations.

Finally, chapter 6 includes conclusions of the thesis report: the obtained results are summarized, and suggestion and recommendations for improvements and future works are at last given in this chapter.

Chapter 2: Feasibility study

In this chapter generic radar specifications for the design are estimated from functional requirements. Section 2.1 introduces the functional requirements derived from the typical application scenario and the purpose of the UWB imaging system. Section 2.2 explains the design choices behind selection of frequency band, describing the fundamental parameters which are affected by this choice. In section 2.3, the different UWB technologies currently available for the realization of radar systems are discussed, and the most appropriate technology for our design is selected. Section 2.4 gives a brief overview of the concepts behind the selection of the antenna array, and an estimation of the number of transmit and receive array elements supposed to be used for the radar system subject of the thesis.

2.1 Functional requirements of the UWB sensor for concealed weapon detection

In order to come to a proper design, it is necessary to define and quantify the functional requirements of the radar imaging system and from this derive the radar specifications.

The UWB sensor is intended for short-range sensing of people at mass events, and its typical application scenario consists in the person under test standing in front of the radar antenna system at a distance comprised between 0.5 and 2 meters, corresponding to the operational range of the radar. In order to be able to scan the whole body at the same time at such short-range, the antenna array is required to have a size comparable with the human body. An antenna aperture of 1 m in width and 2 m in height is thus selected for this purpose.

For any active radar used to scan human beings it is important to keep a low emitted power, due to safety and health concerns. Given the academic purpose of this work, we won't consider the very restrictive safety regulations by FFC for UWB systems, which in our case would limit the EIRP to -41.3 dBm/MHz, but we'll take as our power limit the typical emissions levels from mobile phones, i.e. 1 W (30 dBm).

A crucial requirement for fast operations of the radar is the acquisition time. Since the radar is intended for fast screening of people flows, it should be fast enough to acquire target information in near-real time. For this, it is necessary a data acquisition time of at most 2 s.

Detection of targets attached to the human body requires a fine resolution in order to be able to distinguish reflections from the target itself and the human body. A resolution between 1 and 2 cm is desirable for such purpose.

Furthermore, the ability to detect targets of any kind of material (ceramic, metal, plastic, etc…) requires a solid dynamic range, as the difference in signal strength due to reflection from different materials can be quite high.

Apart from these functional requirements, an important aspect for this design is also represented by the cost and complexity of the radar system that should be both kept as low as possible. The employment of commercial off-the-shelves RF- components for the assembly of the radar system surely helps to keep the cost minimal. Moreover, optimization of the electronics in terms of number of components is also necessary to keep its complexity within bounds and reduce the cost to the minimum.

Once the general requirements and specifications of the radar system have been decided, the following step is to investigate the feasibility of a radar system respecting such requirements. This feasibility study consists in the investigation of optimal frequency band and proper UWB technology to be used for the RF-front-end, and the estimation number of required transmit and receive elements in the antenna array.

2.2 Selection of frequency band

Selection of frequency band is crucial for several aspects of the design. Roughly speaking, the use of microwaves allow complying with most of the aforementioned requirements with more ease than millimeter waves, as it requires a much less dense spatial sampling (and thus less array elements, see section 2.4), consequently reducing the cost of the antenna system, the data acquisition time and the amount of computational power required for data-processing.

Definitive selection of frequency band is usually determined by the required resolution for the intended application. The resolution of the radar measures its ability to distinguish between two closely spaced targets, and it is defined as the minimum resolvable distance between two targets.

For concealed weapon detection, it is desirable to detect and classify weapons of any kind of material (metal, plastic, ceramic, etc…) attached to a human body, without revealing too much anatomical details of the person under test. While millimeter resolution typically results in a photographic-like picture of the naked body, thus breaching personal privacy, centimeter resolution is sufficient to provide enough details of the targets without raising ethical aspects.

For a wideband radar, the resolution in the resulting 3-D image depends on operational bandwidth, central frequency, range to target and the dimensions of the array aperture.

In the down-range dimension, the resolution is purely determined by the radar operational bandwidth, and given by

$$\delta_{\mathrm{dr}} = \frac{\mathrm{c}}{2\,\mathrm{B}} \tag{2.1}$$

where c is the velocity of propagation of the electromagnetic wave in the sensing medium, and B is the operational bandwidth at -10 dB level. As it can be seen from the formula above, high down-range resolution can be obtained with the use of a large bandwidth. The use of UWB technology thus becomes necessary in order to ensure a fine down-range resolution. To obtain the required cm resolution, we must then select a bandwidth of at least 10 GHz, for a 1.5 cm resolution.

On the other hand, the cross-range resolution is typically estimated in the height and width dimensions as:

$$\delta_{\mathrm{cr\_el}} = \lambda_{\mathrm{c}} \frac{\mathrm{R}}{\mathrm{L_{el}}} \tag{2.2}$$

$$\delta_{\mathrm{cr\_az}} = \lambda_{\mathrm{c}} \frac{\mathrm{R}}{\mathrm{L_{az}}} \tag{2.3}$$

where L_{el} and L_{az} represent the length of the effective aperture of the antenna array along the elevation and azimuth directions respectively, R is the range to target and λ_c is the wavelength at the central frequency f_c.

For a MIMO array, the length of its effective aperture is the sum of the lengths of both transmit and receive arrays [5]:

$$\mathrm{L} = \mathrm{L_{tx}} + \mathrm{L_{rx}} \tag{2.4}$$

If we consider identical transmit and receive antenna apertures, the cross-range resolutions become:

$$\delta_{cr\_el} = \lambda_c \frac{R}{L_{el\_tx} + L_{el\_rx}} = \frac{\lambda_c}{2} \frac{R}{L_{el}} \quad (2.5)$$

$$\delta_{cr\_az} = \lambda_c \frac{R}{L_{az\_tx} + L_{az\_rx}} = \frac{\lambda_c}{2} \frac{R}{L_{az}} \quad (2.6)$$

Considering a minimum aperture size of 1 m (azimuth direction), to obtain a cm resolution at 1 m range in the produced 3-D image, a central wavelength of around 2 cm (corresponding to 15 GHz) is necessary. Based on these preliminary considerations, we initially select an operational frequency band between 10 and 20 GHz.

2.3 Selection of UWB technology

UWB radars for concealed weapon detection can be realized based on different UWB technologies, such as video impulse, quasi-random noise, stepped-frequency continuous wave (SF-CW) and frequency modulated continuous wave (FMCW). Selection of optimal technology for our design depends on the functional requirements of the radar, in particular the demand of low power and complexity, fast data acquisition time and high SNR. Based on these requirements, we can make some general consideration on the above mentioned UWB radar technologies, in order to select the most appropriate for our design.

UWB radars can be realized either with Time-Domain and Frequency-Domain technologies. Pulse radars and noise radars are time-domain systems.

Pulse radars physically transmit very short pulses (hundreds of picoseconds) without a carrier, resulting in a signal with an instantaneous ultra-wide bandwidth. Detection of pulses scattered from a target is typically performed via a simple threshold detector, or a more complicated sampler (direct or stroboscopic). The classical block scheme of the UWB video impulse radar is very simple, resulting in a relatively cheap, compact and robust radar design. On the other hand, the energy contained in such short pulses is very low, with the consequence that the peak power has to be very high in order to obtain reasonable SNR performances. Besides, this makes this technology quite sensitive to interferences from other narrowband services and noise, typically resulting in low SNRs. The most serious disadvantage of this technology is that the reception of high instantaneous bandwidth signals requires A/D converters with a very high sampling rate, which are either expensive or very difficult to realize. This problem is typically overcome by the use of stroboscopic

sampling, which requires repetitive measurements to gather enough samples to reconstruct the signal. Such approach mitigates the requirements on ADCs, but causes an increase of the acquisition time and a significant loss of signal energy.

Noise radar technology is typically based on transmission of a continuous pseudo-random sequence of video pulses and correlation processing of reflected radar signals for optimal reception (matched filtering). Continuous transmission of short pulses within a sequence considerably increases the average transmitted power, thus improving the SNR with respect to the video impulse radar. However this also results in a more complex architecture than pulse radars, due to the high number of pulses required for transmission and the complexity of correlation receivers.

UWB frequency-domain radar technologies acquire data in the frequency domain and transmit a continuous wave (CW), whose frequency changes over time. Frequency-domain radars have a solid background, due to the well-developed RF technology and a large selection of commercially available components. This technology typically leads to a higher signal-to-noise ratio due to a higher and more uniform spectral density of the radiated signal and, in principle, it allows the use of a much larger frequency bandwidth than the time-domain approach, and thus higher resolution [1].

There are basically two approaches to realize frequency-domain radars: the stepped frequency approach (or SFCW, Stepped-Frequency Continuous Wave), and the frequency sweep approach (or FMCW, Frequency Modulated Continuous Wave). A SFCW radar transmits a signal whose frequency changes in a step-like fashion, dwelling at each frequency long enough to allow received echo signals to reach the receiver. On the contrary, an FMCW radar, in its simplest form, transmits a signal whose frequency linearly changes with time, covering the whole operational bandwidth.

Both approaches generally make it easier to implement a low power system, thanks to their high duty cycle, and the low complexity in their architectures. However, FMCW has in general a more efficient waveform (duty cycle of 100 %) w.r.t. SF-CW (where the duty cycle is decreased by the dwell time required at each frequency step), and thus FMCW reduces the peak power to the minimum.

In principle, FMCW has a more straightforward implementation in terms of transmission and reception of signal than SFCW, and is thus preferred for our design, as the more convenient way to guarantee a high SNR, while keeping a low complexity in the RF-electronics.

2.4 Estimation of number of antennas

Selection of a multichannel RF-scheme requires knowledge of the number of antennas in the array, in order to optimize the electronics in terms of number of channels, complexity and speed. Before going into a detailed estimation of the required number of antennas, the theoretical concepts behind this estimation are briefly explained.

2.4.1 Data acquisition and spatial sampling

To form a 3-D image of the target under test, the antenna system of an UWB short-range radar has to collect the data over different spatial points within a 2-D aperture in front of the target. Data gathering and the subsequent image reconstruction requires the collected data to be discretized, satisfying the Nyquist criterion.

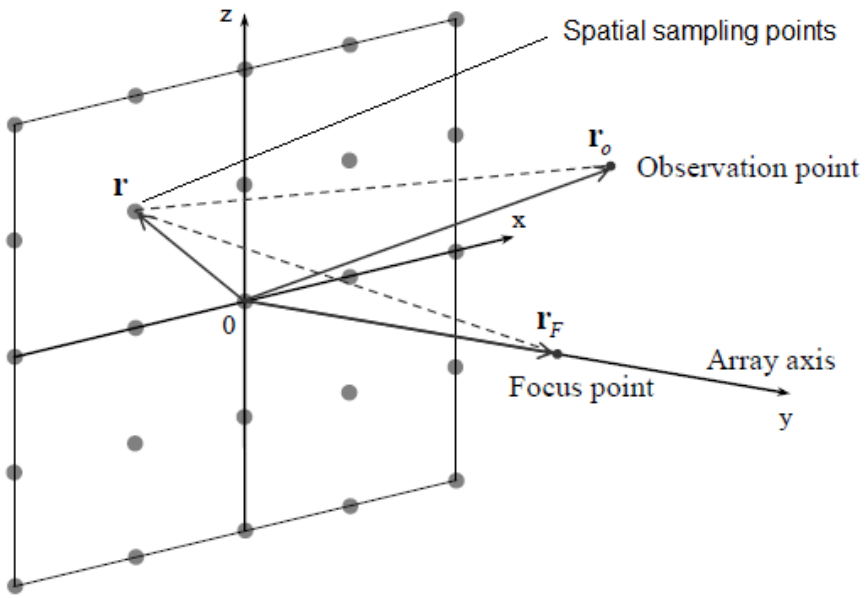

Figure 2.1: Geometry of 2-D planar aperture and positions of spatial sampling points, according to Nyquist criterion [6].

The Nyquist criterion states that in order to prevent unwanted grating lobes in the acquired data, which can severely reduce the contrast or dynamic range for imaging, the phase shift from one spatial point to the next must be less than π rad. The required spatial sampling depends on multiple factors, like size of array aperture and target, wavelength and distance to target. Practical imaging systems often employ spatial sampling in the order of $\lambda/2$.

For a wideband system, the Nyquist criterion needs to be satisfied for the smaller wavelength over the entire operational bandwidth. Thus, once the operational bandwidth and the aperture size are defined, the Nyquist criterion defines the number of spatial points over which the data will be collected, according to the formula:

$$N_{SS\_Nyquist} = \left[\frac{2}{\lambda_{min}} (L_{az} + 1) \right] \times \left[\frac{2}{\lambda_{min}} (L_{el} + 1) \right] \quad (2.7)$$

where L_{az} and L_{el} are the array aperture size in the azimuth and elevation planes respectively, and λ_{min} is the wavelength at the highest frequency. This number refers to the number of required receive antennas, independently from the number of used transmitters.

Data acquisition for array-based imaging radars can be performed with two basic approaches: Real Aperture Radar (RAR) and Synthetic Aperture Radar (SAR).

The RAR approach uses a planar antenna array whose size determines the size of the 2-D aperture. To satisfy the Nyquist criterion, a receive element must be placed on each spatial sampling point within the aperture, making theoretically possible the production of 3-D images in real-time by operating simultaneously all the array elements. On the other hand, this method is often limited by physical constraints such as a limited aperture size and a typically large number of required array elements, often leading to unrealistic costs and electronic fabrication problems. In addition, the simultaneous operation of all the array elements produces a huge amount of data, which would be difficult to handle for real-time operations.

On the other hand, the SAR approach helps to reduce costs at the expense of a longer data-acquisition time. A typical SAR uses a single transmit/receive antenna pair that is mechanically scanned over a set of spatial points (defining the 2-D aperture) to collect the data. In this way, SAR allows synthesizing large 2-D apertures, without demanding a large number of array elements like for RAR approach. This results in a lower cost of antenna array, and requires just a single channel receiver, which makes also the electronics+- part cheaper. On the other hand, this method typically employs mechanical scanners to cover the whole 2-D aperture, resulting in a much larger data acquisition time than RAR, which makes it not feasible for real-time operations. In addition, the scanning procedure could cause errors in positioning of the radar with respect to the target under test, unless a very precise scanner is employed. Positioning errors eventually results in distortions of the image, which can be larger than distortions caused by non-linearities of the radar electronics.

A good compromise between low cost and fast acquisition time consists in a hybrid RAR-SAR approach, realized by replacing mechanical scanning in one direction with a linear array. The array is typically made of identical elementary radiators, and different antenna pairs are sequentially used as transmit and receive antennas. Such approach would require a much lower number of array elements compared to RAR, while achieving a faster acquisition time with respect to SAR, due to one dimensional scanning.

Since the most important requirement in our design is fast acquisition time, the RAR approach is preferable. An antenna array working in the 10-20 GHz frequency band and covering a planar aperture with L_{az} = 1 m and L_{el} = 2 m, according to Nyquist criterion, would then require a total of 135×268=36180 different spatial points over the aperture, for a total of 72360 antenna elements, assuming the case with the same number of transmit and receive elements. An array with so many elements would be very expensive and almost impossible to realize with current technology, and it would require an enormous computational power to process all the data. Array thinning is thus required.

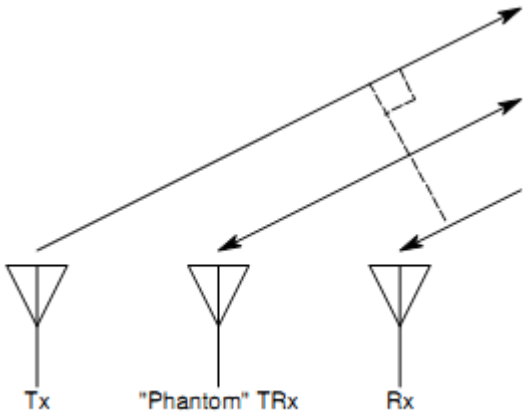

Figure 2.2: Phantom element positioned mid-point between the transmitter and the receiver [13].

2.4.2 MIMO approach and sparse array concept

A good technique for array thinning that has recently emerged also for radar applications is the multiple-input multiple-output (MIMO) approach, which allows to obtain near-field beam patterns comparable to the ones of a dense array, by synthesizing filled apertures ($\lambda/2$ element spacing for both transmit and receive) with a much lower number of array elements than RAR approach. This technique is based on the notion of phantom transmit/receive elements, illustrated in figure 2.2, and

described in [13]. Considering a target in the far-field, signals from a bistatic transmit/receive pair would be identical to signals received from a monostatic transmit/receive element positioned mid-point between transmit and receive elements of the bistatic pair. In a MIMO array, a phantom element is synthesized for each different transmit/receive pair in the array, thus making possible to synthesize a completely filled aperture comprising M×N virtual elements, by using only M transmit and N receive antennas. The total number of antennas will then be minimal by selecting equal number of elements in both transmit and receive arrays. For a wideband system, the number of required spatial sampling points or virtual elements is

$$N_{SS\_MIMO} = \left[\frac{2}{\lambda_{min}}(L_{az}+1)\right] + \left[\frac{2}{\lambda_{min}}(L_{el}+1)\right] \tag{2.8}$$

With a planar aperture with L_{az} = 1 m and L_{el} = 2 m, and a 10-20 GHz frequency band, a MIMO array thus requires 135+268 = 403 elements, while with Nyquist criterion this number would have been 72360, assuming the case with the same number of transmit and receive elements.

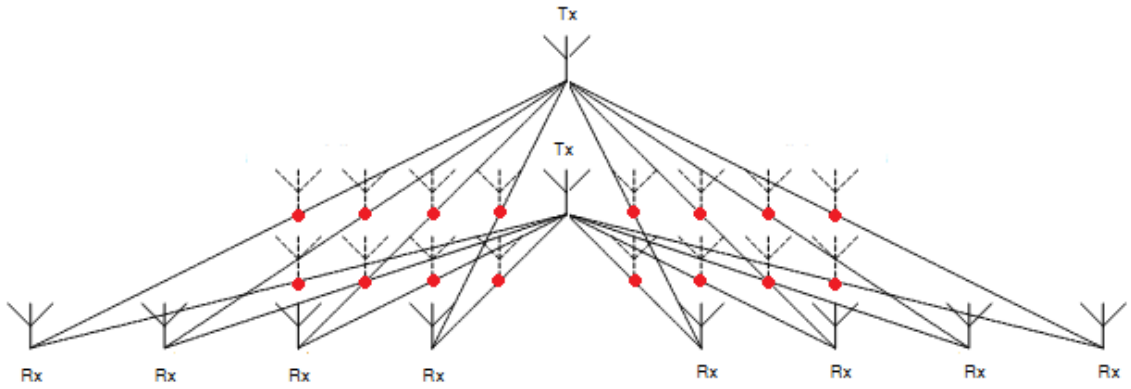

Figure 2.3: Example of 2-D synthesized planar array with 16 phantom elements (in red, using 2 transmit and 8 receive elements [modified from 13].

For a MIMO antenna array, the effective array aperture is equal to the spatial convolution of transmit and receive antenna array apertures. As a result, it is possible to synthesize large and dense arrays while the real antenna aperture and the element spacing can be smaller and coarser. Furthermore, by using spatially distributed multiple transceivers, MIMO radars capitalize on the diversity of target illumination and scattering by viewing the target from multiple aspect angles, improving the detection capabilities and the possibility to reduce clutter. The advantages of MIMO antenna arrays are demonstrated in [9, 10 and 12].

On the other hand, such method has a major drawback: as a matter of fact, array thinning typically results in a dramatic increase of grating lobes, which can severely reduce the contrast or dynamic range available for imaging. Reduction of these grating lobes is necessary to obtain good performances.

The use of UWB signals for transmission is an effective approach to reduce the influence of grating lobes in thinned or sparse arrays. In [6] it is shown how under the condition that the fractional bandwidth of the transmitted signal is at least 100%, where $B \geq f_c$, a majority of the expected grating lobes occurs outside the IR (Interfering Region), thus not enhancing each other and drastically reducing their influence on the array pattern. To ensure the elimination of the entire grating plateau, one must ideally select a 200% fractional bandwidth. As a general rule the higher the fractional bandwidth, the lower the influence of grating lobes, as shown in figure 2.4.

Apart from the signal bandwidth, the distribution and level of sidelobes is strictly related to the array topology. Previous research demonstrates that with aperture thinning and an appropriate array topology, it is possible to obtain a sidelobe level comparable with that of dense arrays with λ/2 element spacing, while drastically reducing the number of array elements [5]. As a matter of fact, a well-done array topology optimization actually redirects side/grating lobes to different positions so that they don't enhance each other.

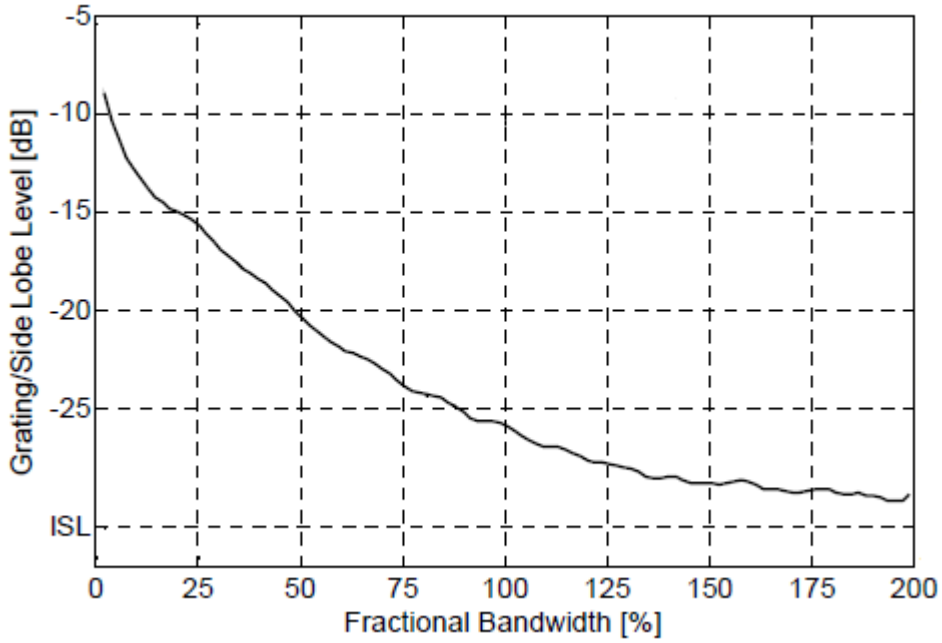

Figure 2.4: Influence of fractional bandwidth on the grating/side lobe [dB]. The aperture size is 100 λ_c with 2.5 λ_c element spacing. Image taken from [6].

Also in [6], a method is described to determine the minimal number of array elements in a UWB array-based imaging system, based on the mainlobe-to-sidelobe ratio required in the resulting images. Under the ideal condition where all grating lobes have been eliminated, the mainlobe-to-sidelobe ratio can be simply estimated by the ideal sidelobe level (ISL) defined as:

$$\mathrm{ISL} = 20\log_{10}\left(\frac{1}{N_E}\right) \tag{2.9}$$

where N_E is the total number of sampling points or virtual elements within the effective aperture. As already mentioned, for a MIMO array N_E represents the product of transmit and receive elements, when no redundancy exists within the effective aperture:

$$N_E = N_{tx} \cdot N_{rx} \tag{2.10}$$

while total number of antennas within the array is

$$N = N_{tx} + N_{rx} \tag{2.11}$$

The ISL is a 1-D approximation of the maximum sidelobe level in the resulting image of a sparse UWB array aperture. However, the achievable sidelobe level in the near field is generally worse than the ideal case, due to spreading loss and near-field effects [6]. The ISL is thus used to derive the minimal number of virtual elements needed along each dimension of the 2-D array aperture based on the required dynamic range in the image. Anyhow, the total number of antennas will be minimal by selecting equal number of elements in both transmit and receive arrays, thus reducing it from N to $2\sqrt{N}$.

In our case, with the typical application scenario consisting of a person standing in front of the array aperture of 1 m azimuth and 2 m elevation, we require 30 dB dynamic range in the azimuth plane, and 40 dB in the elevation plane, due to the larger dimension of human body in that direction. This makes a number of 32 samples required on the azimuth plane and 100 samples along the elevation plane. A conventional 2-D array would then require 3200 spatial samples or elements that, if we consider the case with equal number of transmit and receive elements, with MIMO technique can be reduced to about 114 elements, with 57 transmit and 57 receive antennas. For convenience, we approximate this numbers to 60 transmit and 60 receive elements.

2.5 Conclusions

In this chapter, generic radar specifications for the design of the UWB imaging systems have been derived from functional requirements and discussed. The UWB imaging system is intended for fast sensing of people flows at short distances. In the typical application scenario, the person under test stands in front of the radar at a distance between 0.5 and 2 m, selected as the operational range of the radar. Given its short operational range, the radar is required to emit low power (lower than typical emissions from mobile phones, i.e. 1 W), in order not to raise any health issue.

A crucial requirement for fast operations is the data acquisition time, which should not exceed the 2 s. An antenna aperture of size comparable with the human body was considered ideal in order to entirely scan a person's body at the same time, and thus we selected an antenna aperture of 2 m in height and 1 m in width.

Particular attention was paid to minimization of cost and complexity of the electronics. For this, use of UWB microwave technology is ideal, since it guarantees the centimeter down-range resolution required for detection of targets attached to the human body, while at the same time it helps reducing the cost and complexity of the overall system, when compared to current state-of-the-art Imaging Systems working in the millimeter wave region. Furthermore, a cm resolution was considered sufficient to provide enough details of the targets, without raising the privacy issues that accompany millimeter wave imaging systems. For our specific design, we preliminarily selected a frequency bandwidth of around 10 GHz, to achieve a down-range resolution between 1 and 2 cm.

As to the implementation of the radar front-end, the FMCW technology was selected as the more convenient way to achieve a good SNR while keeping the cost and complexity of the electronics to the minimum.

Use of an Multiple-Input-Multiple-Output (MIMO) antenna array was also considered crucial to respect the above requirements, since a well-designed MIMO antenna array allows reducing the number of antennas in the array without degrading its performance. A lower number of array elements entails a lower cost and complexity in both the antenna system and the RF-electronics, while reducing the amount of produced data and thus the required acquisition time and computational power. Given the requirements of our design, we finally estimated a total number of 60 receive and 60 transmit elements for the MIMO antenna array.

Chapter 3: Development of FMCW multi-channel scheme

In this chapter, a more detailed explanation of design choices and tradeoffs for the selection of the RF-scheme for the UWB FMCW radar is given. In the first paragraph, basic theoretical concepts of FMCW radars are discussed. The second paragraph discusses the design choices and tradeoffs concerning complexity of the multichannel receiver and its data acquisition time that were made in order to arrive to a definitive choice of the RF-scheme. In the third paragraph, selection of off-the-shelves RF-components for the selected RF-scheme is performed, and definitive selection of number of receive channels and computation of data acquisition time for the optimal multichannel RF-scheme are illustrated.

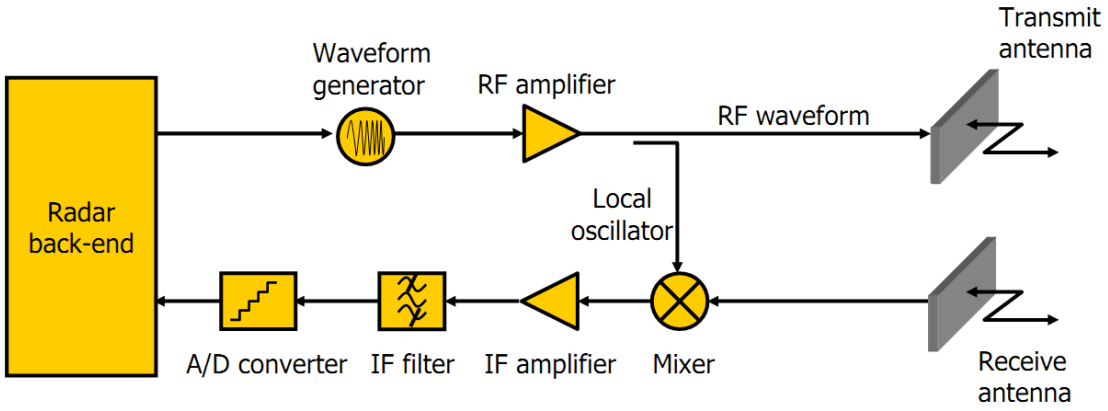

Figure 3.1: Homodyne FMCW radar front-end with separated transmit and receive antennas [17].

3.1 General description of homodyne FMCW radar block diagram

Before going into detailed design of the RF multichannel scheme, it is convenient to give some theoretical concepts of FMCW radars.

An FMCW radar system produces a continuous wave signal which is frequency modulated over a determined bandwidth. The basic ranging principle of FMCW radar consists in measuring the frequency shift caused by the time delay of a reflected signal, when the transmitted signal is frequency modulated by a periodic waveform.

In its simplest form, FMCW radar uses a homodyne receiver which requires a reference signal directly coupled from the transmitter, to be mixed with the echo signal. As a matter of fact, the

signal generated by the radar is split into two parts: a smaller part is allowed to pass into the LO port of the mixer, where it is used as a reference signal for detection of echo signal, while the other, larger portion of the generated signal passes out into the antenna and is transmitted. By mixing the reference signal directly coupled from the transmitter with the echo signal, the receiver performs a direct conversion from RF to zero-IF frequency, extracting the target information in only one conversion stage. A typical FMCW radar front-end is shown in figure 3.1. The transmitted waveform is represented by the equation

$$s_{tx}(t) = A_{tx}\cos(2\pi f_0 t + 2\pi\varphi(t)) \tag{3.1}$$

where A_{tx} is the amplitude of the transmitted waveform, f_0 is the starting frequency,

$$\varphi(t) = \frac{1}{2}kt^2 \tag{3.2}$$

is the phase variation due to the frequency sweep, and k is the modulation rate.

The instantaneous frequency f(t) of the transmitted signal is then obtained by differentiating the instantaneous phase with respect to time:

$$f(t) = \frac{1}{2\pi}\cdot\frac{d(2\pi f_0 t + \pi kt^2)}{dt} = f_0 + kt \tag{3.3}$$

Typically the modulation is linear in frequency, as shown in figure 3.2. This signal is also known as a chirp, named after the sound a bird makes when it increases the pitch of its call over a short period of time. The total time needed for the waveform to cover the entire frequency range B from f_0 to f_1 is the sweep time T_{sweep}.

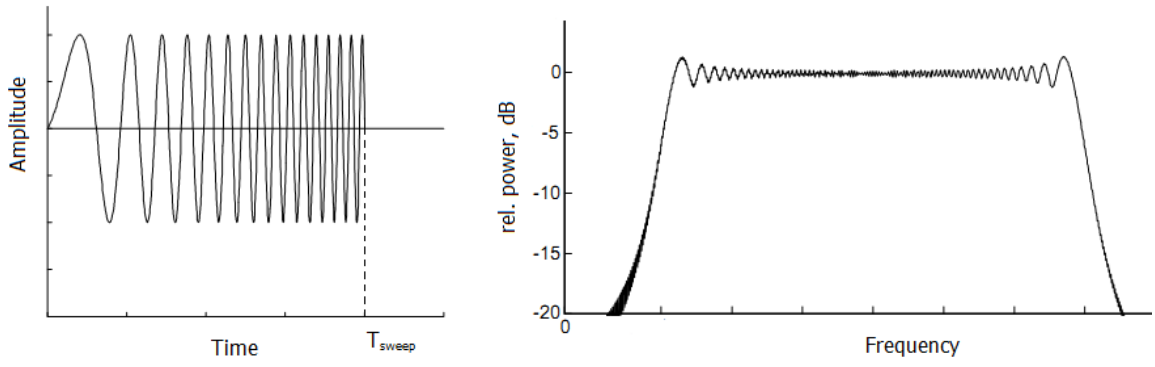

Figure 3.2: Linear chirp signal in time-domain (left) and frequency-domain (right).

The modulation rate k is thus represented as

$$k = \frac{(f_1 - f_0)}{T_{sweep}} = \frac{B}{T_{sweep}} \tag{3.4}$$

After emission from a transmit antenna, the transmitted signal propagates into the air to a target where part of it is reflected back towards the radar. The echo signal is thus an attenuated version of the transmitted signal that is delayed by the time τ needed for the waveform to travel the two-way path between the target and the antenna, expressed as

$$\tau = \frac{2R}{c} \tag{3.5}$$

where R represents the distance between the radar and the antenna, and c represents the propagation velocity of the waveform. The received signal is then expressed as

$$s_{rx}(t) = A_{rx}\cos(2\pi f_0(t-\tau) + 2\pi\varphi(t-\tau)) \tag{3.6}$$

where A_{rx}, the amplitude of the received signal, accounts for propagation losses, target reflectivity and a variety of radar performance parameters.

At the mixer stage the received signal is multiplied with the reference signal that came into the LO port of the mixer. This process produces sum and difference frequency terms. The sum frequencies are in the order of twice the radar carrier frequency, and can be easily filtered out with a low pass filter. The other term represents the difference frequencies between transmitted and

received waveform, and is directly related to the time delay due to the two way path between radar and target, and thus their distance. This difference term, also called beat signal, is represented as:

$$s_{beat}(t) = s_{tx}(t) \otimes s_{rx}(t) = A_{beat}\cos(2\pi f_0 \tau + 2\pi kt\tau - \pi k\tau^2) \tag{3.7}$$

The beat frequency is finally obtained by taking the first derivative of the phase:

$$f_{beat} = \frac{1}{2\pi} \cdot \frac{d(2\pi f_0 \tau + 2\pi kt\tau - \pi k\tau^2)}{dt} = k \cdot \tau = \frac{B \cdot \tau}{T_{sweep}} = \frac{2R \cdot B}{c \cdot T_{sweep}} \tag{3.8}$$

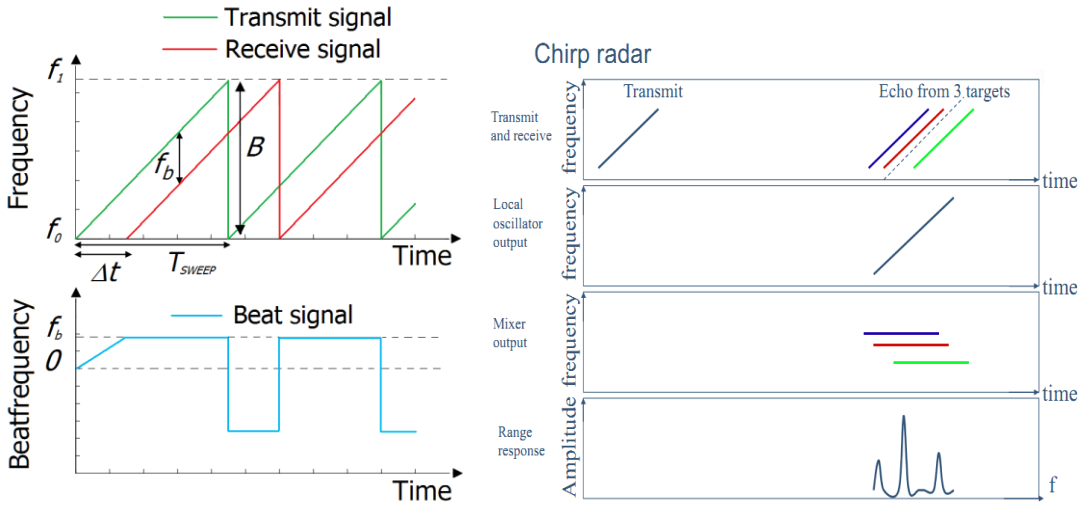

Figure 3.3: Concept of beat frequency (left) and typical signals in FMCW radar (right).

In FMCW radar applications, targets are found by performing Fourier analysis on the mixer's output signal. Using a Fourier transform with a rectangular window of integration extending over a time interval of length T_{sweep} leads to the following representation of the power in the mixer output signal:

$$S_{IF}(f) = P_r \left(\frac{\sin[\pi(f - f_{beat})T_{sweep}]}{\pi(f - f_{beat})T_{sweep}} \right)^2 \tag{3.9}$$

where f is the analysis frequency, and $P_r = A_{beat}^2$ is the power of the target echo. In terms of the standard radar equation, the target echo power P_r can be written as:

$$P_r = P_t \frac{\sigma G_t G_r \lambda^2}{(4\pi)^3 R^4} \quad [W] \tag{3.10}$$

where P_t is the transmitted power (W), σ is the radar cross section of the target (m^2), λ is the wavelength (m), R is the distance to target (m), and G_t and G_r are the transmit and receive antenna gains respectively.

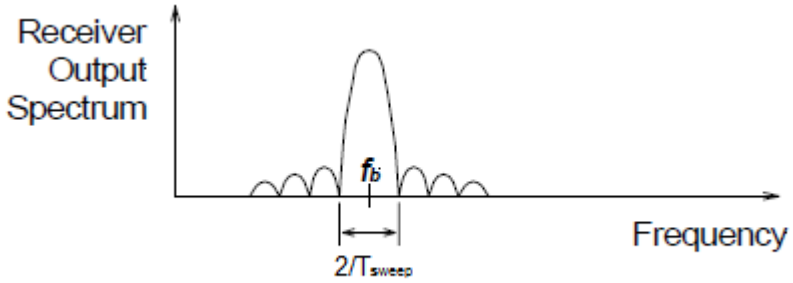

Figure 3.4: Beat signal at mixer output due to single target.

3.2 Selection of the multi-channel RF-scheme

After discussion of the functional requirements and radar specifications in chapter 2, the next step in the design of the UWB radar consists in the selection of an RF-scheme which minimizes acquisition time and number of receive channels to keep a low complexity in the electronics. In particular, acquisition time is an important parameter that characterizes the performance of the radar system. In our application scenario, the UWB radar is used to quickly investigate people at mass events, which requires an acquisition time in the order of seconds.

3.2.1 Tradeoff between data acquisition time and number of receive channels

In our design, the UWB Radar is supposed to be connected to an antenna array in a MIMO configuration. A MIMO antenna system is made of multiple transmit and receive antennas, with transmission and reception performed in the simplest case with one transmit and one receive antenna at a time. For a MIMO array and the basic RF-scheme of figure 3.1 with one transmit and one receive channel, the total acquisition time would then be equal to the sweep time of the YIG

tuned oscillator, multiplied by the product of the number of transmit antennas with the number of receive antennas. However, the acquisition time can be reduced by parallelizing reception with multiple receive channels. Parallel transmission via multiple transmit channels would only be feasible in case of transmission of orthogonal signals, but such approach would severely increase the complexity of the electronics and is not considered. Thus in general the total acquisition time for the multichannel RF-scheme can be computed as:

$$T_{acq} = N_{TX} \cdot \left(\frac{N_{RX}}{N_{CH}} \right) \cdot T_{sweep} \qquad (3.13)$$

where N_{TX} and N_{RX} are the number of transmitting and receiving antennas respectively, and N_{CH} is the number of receive channels.

As already mentioned in chapter 2, the antenna array of the UWB radar is supposed to be made of 60 transmit and 60 receive antennas in a MIMO structure, and given this high number of antennas, parallelization of reception via a multichannel receiver is necessary to keep the data acquisition time within the specified requirement of a few seconds.

Selection of the optimal number of receive channels will be made based on the specifications of available RF-components, and will be treated in the next paragraph.

3.2.2 Selection of commercial off-the shelves components and final selection of number of receive channels.

After selection of the generic RF-scheme, the following step consists in finding the proper components which satisfy the given requirements.

The basic FMCW scheme, with separated transmit and receive antennas, is shown in figure 3.1. The waveform generator represents a key component for the performance of the radar. Typically, a VCO (voltage controlled oscillator) is used to generate the FMCW signal, whose output frequency is determined by the input voltage. Ideally the output frequency should increase linearly with the input voltage, but in practice there are always deviations from the ideal case, as shown in figure 3.5. The most noticeable effect of these deviations is a degradation of down-range resolution. As a matter of fact, the generation of a non-linear frequency sweep results in a non-constant beat frequency for targets at a constant range. The degraded range resolution can be estimated as

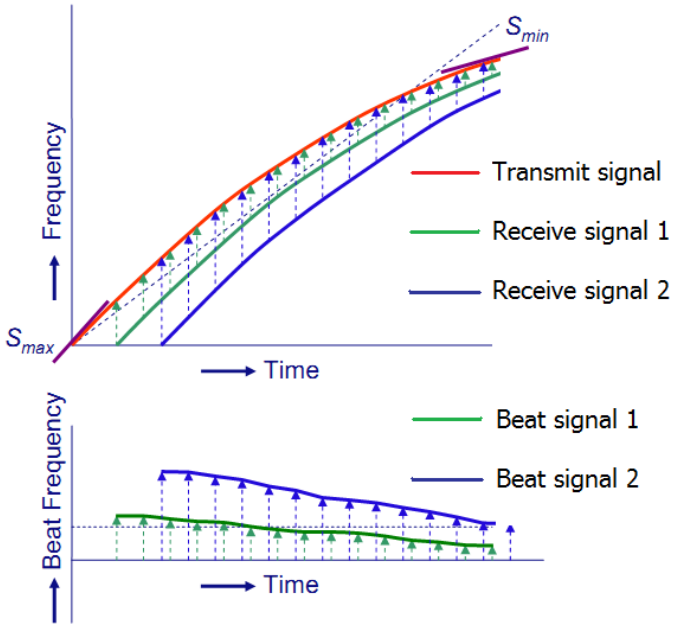

Figure 3.5: Example of nonlinear frequency sweep and resulting beat frequency.

$$\Delta R = \sqrt{\left(\frac{c}{2B}\right)^2 + (R \cdot Lin)^2} \tag{3.11}$$

where *Lin* represents the linearity of the sweep, defined as the change in chirp slope, $S=df/dt$, normalized to the minimum slope:

$$Lin = \frac{(S_{max} - S_{min})}{S_{min}} \tag{3.12}$$

Commercially available VCOs specify their linearity as the deviation of frequency versus input voltage characteristic from the ideal straight-line case. YIG tuned oscillators have excellent linearity characteristics, much better than that of typical VCOs, and are thus the optimal choice as signal generator to reduce problems caused by nonlinearities.

For the sake of high down-range resolution, the UWB radar requires a large frequency band, which was initially supposed to be in the 10-20 GHz range. After a survey of commercially available components, it was not possible to find a proper combination of components within the specified bandwidth to reproduce the RF-scheme, not without the use of multiple filters to adjust the bandwidth. Instead, an RF-scheme working in the 6-18 GHz bandwidth has been considered more

feasible, given the availability of a variety of devices, cables and connectors within that bandwidth. Among these, we have selected the following components as blocks of our UWB sensor:

YIG-Tuned Oscillator (YTO), customized from model n. MLMH-0208, by Microlambda Wireless:

- Frequency sweep: 3-9 GHz;
- Tuning speed: 80 μs/GHz;
- Output power, min.: + 14 dBm min.;
- Harmonic level, min.: -15 dBc min.;
- Spurious output, min.: - 70 dBc;
- Phase Noise level, min.: –100 dBc/Hz @ 10 kHz offset and –120 dBc/Hz @ 100 kHz offset;
- Linearity: ± 0.25%;

The YTO is controlled by means of a driver, a separate device which transforms the tuning voltage into current. For the sake of fast acquisition time, we preferred to select a combination of a fast sweep 3-9 GHz YTO and frequency doubler to produce the 6-18 GHz chirp signal, due to the fact that commercially available YTOs working in the 6-18 GHz band have sweep speeds of around 1 ms/GHz.

N. of receive channels	1	2	3	4	5	6	10	12	15	20	30	60
Acquisition time (s)	1,73	0,86	0,58	0,43	0,35	0,29	0,17	0,14	0,12	0,09	0,06	0,03

Table 3.1: Relationship between number of receive channels and total acquisition time.

With the selected YTO, one sweep is performed in less than 500 μs, which allows achieving a total acquisition time within a few seconds with a relatively low number of receive channels. In table 3.1, is reported for different numbers of receive channels the total acquisition time for the selected MIMO antenna array, with 60 transmit and 60 receive elements, computed with formula (3.13), with one transmission channel and a 500 μs sweep time.

Given the requirement on acquisition time of 2 s, even a single channel receiver would be enough. However, for the sake of an enhanced quality of the gathered data, a higher number of

channels is preferred, as it allows performing repetitive measurements of the same target over the required acquisition time of 2 s, thus improving the SNR, as it will be shown in section 4.4.

A receiver with 10 channels is considered a good compromise between speed, complexity of the receiver and quality of the data: the fast acquisition time (0.17 s per measurement) allows gathering 10 full data-sets for a total acquisition time of 1.7 s, and is thus selected for the RF-scheme.

Apart from the YIG VCO, the other components selected for the RF multichannel scheme are:

- Frequency Doubler FDMP20401 by Teledyne Cougar:
    - Input frequency range: 2-10 GHz;
    - Output frequency range: 4-20 GHz;
    - Conversion Loss: 10.5 dB typ., 12 dB max.;
    - Suppression fundamental frequency: 32 dBc typ.;
    - Suppression 3rd harmonics: 38 dBc typ.;
    - Input power: 10 dBm nominal, 23 dBm max (@ 25°);

- Power amplifier AML618P2301 by AML-Microsemi:
    - RF bandwidth: 6-18 GHz;
    - Gain: 26 dB, min.;
    - Output P1dB: 30 dBm min.;
    - Input/Output VSWR: 2.0:1, nominal;

- Directional Coupler CD-602-183-20S-R by Miteq:
    - RF bandwidth: 6-18 GHz
    - Coupling: 10 dB (Coupling loss: 0.46 dB)
    - Insertion Loss: 1.2 dB
    - Peak Power: 1 W.
    - VSWR: 1.4:1

Now, since each RF-scheme has 10 channels, the LO reference signal coming out from the coupler has to be split over 10 branches, and amplified in order to be used by each channel. This

can be accomplished with the use of a power splitter and 10 power amplifiers. Selected models for our scheme are the following:

- 10-way Power Divider, model n. PS10-11, by Microwave Communications Laboratories, Inc.: Industries, Inc.:

  - Frequency range: 6-18 GHz;
  - Coupling Loss: 10 dB, nom.;
  - Insertion Loss: 3.8 dB, min.;
  - Isolation: 10 dB, min.;
  - VSWR input: 2.0:1, max.;
  - VSWR output: 1.9:1, max.;

- Power Amplifier, model n. A2CP18629, by Teledyne Cougar:
  - RF bandwidth: 6-18 GHz;
  - Gain: 15 dB typ.;
  - Output P1dB: 28.5 dBm min.;
  - Input/Output VSWR: 2.0:1, nominal;

For each receive channel, the following RF-components are selected:

- Low Noise Amplifier, model n. CBL06182825, by Cernex, Inc.:
  - RF bandwidth: 6-18 GHz;
  - Gain: 28 dB;
  - Noise Figure: 2.5 dB;
  - Output P1dB: 15 dBm;
  - VSWR: 2.0:1.

- IQ Mixer model n. IRM0618HC2Q, by MITEQ:
  - RF bandwidth: 6-18 GHz

- IF bandwidth: DC-500 MHz;
- Conversion Loss: 12 dB typical, 13 dB max;
- RF to LO isolation: 18 dB typ., 20 dB max;
- Noise Figure: 10.5 dB;
- Input P1dB: 15 dBm;
- VSWR: 2.0:1.

At both transmit and receive side, the 60 elements antenna array is supposed to be connected to the RF-system via a switching system. For this purpose, the best solution consists in a switching system with one SP6T switch and 6 SP10T switches at transmit side, and a single SP6T switch for each receive channel, as it is shown in figure 3.7. Among the commercially available 6-18 GHz RF-switches, we selected the following models:

- Switch SP6T by G.T. Microwave:
  - RF bandwidth: 6-18 GHz;
  - Insertion Loss: 2.6 dB (reflective) or 3 dB (absorptive);
  - Isolation: 60 dB;
  - Switching time 1 μs;
  - Input power: 30 dBm max;
  - VSWR 2.0:1 max.;

- Switch SP10T by Herley General Microwave:
  - RF bandwidth: 6-18 GHz;
  - Insertion Loss: 4.3 dB (6-12 GHz) or 5.6 dB (12-18 GHz) max.
  - Isolation: 70 dB;
  - Switching time 700 ns max.;
  - Input power: 0.6 W max. (27.78 dBm);
  - VSWR 2.0:1 max.;

For the sake of thoroughness, the total switching time required to gather data for every combination of transmit and receive elements is also estimated.

At reception, for each transmit antenna, the receiver's switches will have to switch 5 times in order to receive with all the 60 receive antennas. Receive switching time is thus:

$$T_{switch\_RX} = 60 \cdot 5 \cdot \left(T_{switch\_SP6T} \right) \quad [s] \tag{3.14}$$

which makes a total of 50 µs, to be added to the acquisition time of a single measurement.

At transmission, for each position of the receive switches, transmitting sequentially with each transmit element will require the SP6T element to switch 5 times, while for every position of the SP6T switch, the downstream SP10T switches will switch 9 times each, thus making the total switch time at transmission equal to

$$T_{switch\_TX} = 5 \cdot \left[5 \cdot \left(T_{switch\_SP6T} \right) + 5 \cdot (9 \cdot T_{switch\_SP10T}) \right] \quad [s] \tag{3.15}$$

which makes a total of 182.5 µs to be added to the acquisition time of a single measurement.

Total switching time is simply the sum of receive and transmit switching times, 232.5 µs, which is 3 orders of magnitude lower than the 170 ms data acquisition time of a single measurement, and is thus negligible.

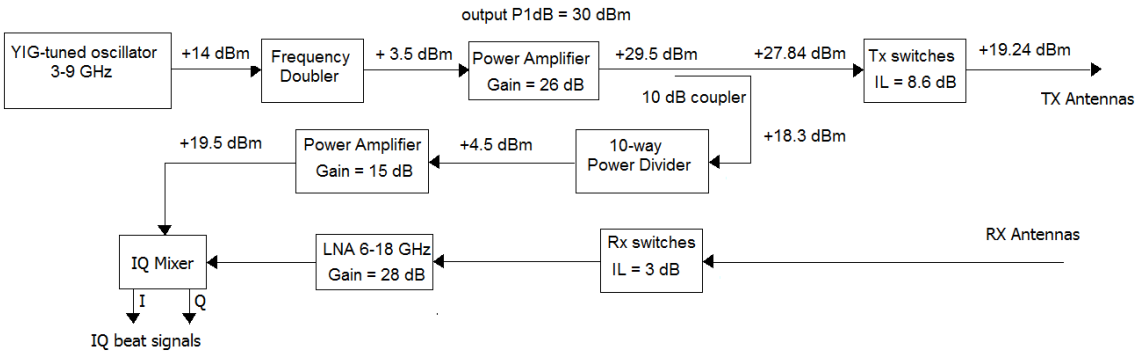

Figure 3.6: RF-scheme with selected components' specifications. For simplicity, only one of the 10 receive channels is reported here.

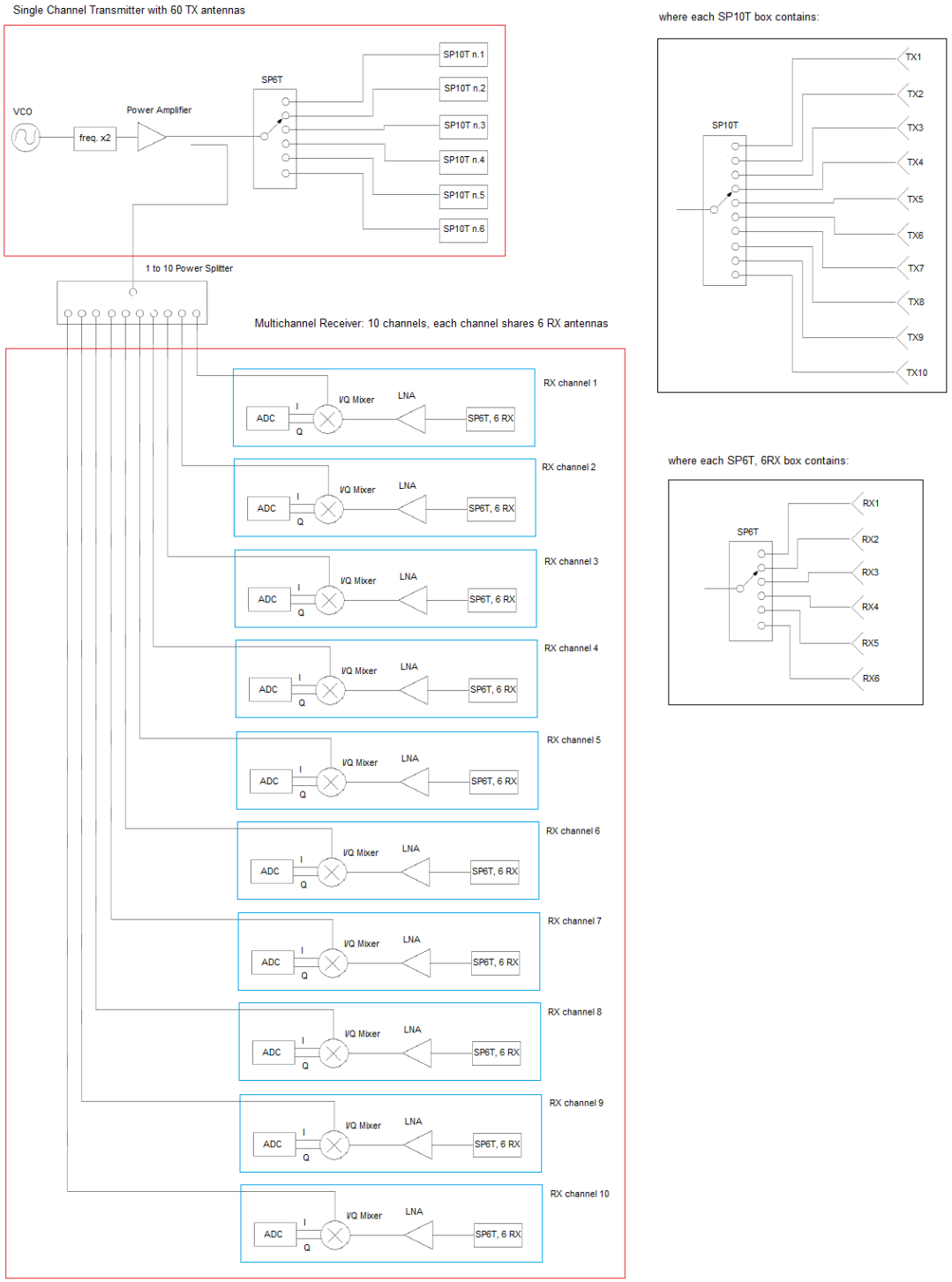

Figure 3.7: Multichannel RF-scheme, with a single transmit channel with 60 TX antennas, and 10 channels receiver, with 6 RX antennas per channel.

3.3 Conclusions

In this chapter, the criteria and the tradeoffs followed for the final selection of the FMCW multichannel RF-scheme have been presented.

In the first paragraph, it was simply presented the set of fundamental concepts of FMCW radars, with particular attention to the homodyne architecture, which was selected for our design because of its simplicity.

Optimization of the RF-electronics in terms of number of channels and achieved data acquisition time was performed based on the number of transmit and receive elements in the MIMO array estimated in chapter 2, and the availability of commercial off-the-shelves RF-components, used to keep the cost to the minimum.

After a survey of commercially available RF-components, the final choice consists of a 6-18 GHz multi-channel RF-scheme with a single transmit channel and 10 parallel receive channels, with the chirp signal generated by a combination of a fast sweep YTO working in the 3-9 GHz band, followed by a frequency doubler which generates the required 6-18 GHz chirp signal.

The RF-scheme is connected to the antenna array via a series of switches, allowing to use any combination of transmit and receive antennas for the acquisition of a full dataset.

The final RF-scheme is characterized by a data acquisition time of 0.17 s, while the total switching time required for each full data-set acquisition is about 1000 times less and thus negligible. Such a low data acquisition time is a very good result, and allows gathering 10 full datasets in a total of 1.7 s.

Chapter 4: FMCW performance analysis

In this chapter, the performance of the selected RF-scheme is evaluated. In the first paragraph, a power analysis is performed; the strongest reflection from a target at minimal operational distance is estimated, in order to investigate the saturation point of the receiver. In the second paragraph, a noise analysis for the RF-scheme is performed. The noise floor of the receiver is estimated, and influence of phase noise on total noise power is also investigated. In the third paragraph, the power budget and dynamic range at the receiver input are estimated. In the fourth paragraph, a detectability analysis of typical targets and analysis of SNR are performed.

4.1 Power Analysis

A proper radar design requires knowledge of the received power from the target signal. In our typical scenario, where the UWB sensor is used to quickly investigate flows of people at mass events, the person under test stands in front of the sensor at a minimal distance of 0.5 m. The stronger received signal will probably be the direct coupling between transmit and receive antennas. Antenna coupling represents a direct signal between transmit and receive antennas, whose magnitude and duration depends on both the type of antenna elements and their configuration. For a FMCW signal, where transmission and reception are performed together, antenna coupling could cause saturation of the receiver and thus hide reflections from targets. It is thus necessary to guarantee that the coupling levels don't exceed the saturation point in the receiver. Then, if the coupled signals can be separated from target responses in the range profiles of each transmit/receive pair within the array, their influence in the resulting image will be minimal. On the other hand, if element coupling and target responses are overlapped, the dynamic range of the imaging system could be significantly reduced.

A possible way to reduce antenna coupling could be the use of transmit and receive antennas with orthogonal polarizations. In this way, direct coupling between each transmit and receive element would be reduced, as the direct signal will have a different polarization than receive antenna. Use of absorbers to decrease the amount of leaking signal is also foreseen to reduce the problem. In any case, coupling compensation should be performed, by measuring the amount of antenna coupling for each transmit/receive pair before-hand, and successively subtract it from the acquired target data.

In addition, other possibly strong signals could be originated by background reflections, but theoretically, if situations with strong reflectors in the vicinity of the radar are avoided, their contribution should be lower than reflections from actual target, and thus could be measured during calibration at the spot and compensated via background subtraction.

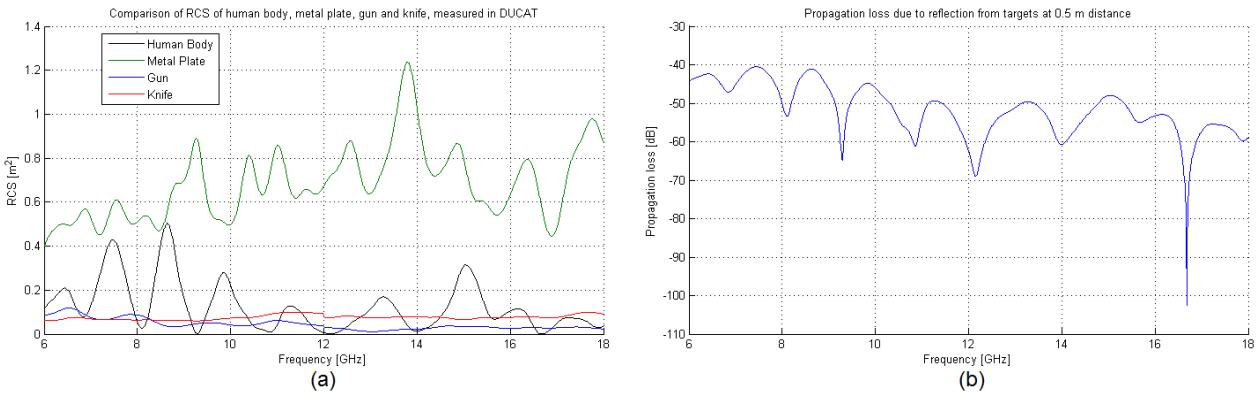

Figure 4.1: a) Estimated reflectivity of human body and metal plate compared with more precise estimation of RCS of a handgun and a knife; b) Propagation loss due to reflection of Human Body at 0.5 m distance.

Thus, if we assume a careful MIMO array design and a well-done calibration procedure, we'll suppose here that the stronger signal comes from a human body at 0.5 m, so the knowledge of the radar cross section (RCS) or the reflectivity of a human body in the 6-18 GHz bandwidth is required.

The reflectivity of a human body has been estimated via near-field measurements in DUCAT, and the measurement setup and the estimation procedure are illustrated in Appendix A. As it can be seen from figure 4.1 (a), the highest estimated value of human body reflectivity is about 0.5 m^2.

Propagation losses in free space associated with the target signal can be then estimated by using the radar range equation:

$$L_{free\_space} = 10\log[\sigma \frac{G_t G_r}{4\pi}(\frac{1}{4\pi R_{tx} R_{rx}})^2] \qquad (4.1)$$

where σ is the RCS of the target; G_t and G_r are the gains of the transmitting and receiving antennas respectively, and are considered here to be both 6 dBi; λ indicates the wavelength; R_{tx} and R_{rx} represent the distance between the transmit antenna and the target and between the target and the receive antenna respectively. The resulting propagation loss due to reflection from human body at

minimal operational distance of 0.5 m over the 6-18 GHz operational band is shown in figure 4.1 (b). By using the peak value of measured reflectivity, the lowest propagation loss in free space is estimated as -40.5 dB.

Next, we can estimate the maximum power at the receiver input, by simply summing this value to the signal power delivered to the transmit antennas. The YTO provides a 3-9 GHz signal with an output power of + 14 dBm, which is then frequency doubled to achieve a 6-18 GHz signal with 3.5 dBm output. The power amplifier increases the signal power to 29.5 dBm. A directional coupler with coupling factor of 10 dB (which means 0.46 dB of coupling loss) and insertion loss of 1.2 dB, allows part of this power to go to the mixer as a reference signal (19.3 dBm), while 27.8 dBm are still available for transmission. However, the use of SP6T and SP10T switches with total insertion loss of 8.6 dB, and of about 1 m long RF-cables (with 1 dB attenuation) to connect the transmitter to the antenna array, further reduces the power delivered to the antenna array to 18.2 dBm.

Signal power at the receiver input will then be given by the sum of the output power (which is a positive quantity) and the propagation loss (negative):

$$P_r = P_{out} + L_{free\_space} \quad [dB] \tag{4.2}$$

The maximum allowed power at receiver input in our homodyne scheme mainly depends on the specification of the LNA and the mixer. Indeed, the maximum power allowed at LNA input is given by:

$$P_{LNA} = P1dB_{MIX} - G_{LNA} = 15 - 28 = -13 \quad [dBm] \tag{4.3}$$

If we also take into account the insertion loss of 3 dB due to the SP6T switches connecting the RF-board to the antenna array, and the 1 dB attenuation due to the 1 m long RF-cable, the maximum received power at the antenna, which causes saturation of the receiver, is -9 dBm. The maximum estimated signal arriving at the antenna is

$$P_{r\_max} = P_{out} + L_{free\_space\_human\_body} = 18.2 - 40.5 = -22.3 \quad [dBm] \tag{4.4}$$

The maximum estimated signal is thus 13.3 dB lower than the saturation point of the receiver.

4.2 Noise Analysis

One of the most important characteristics which determines the radar performance is its signal-to-noise ratio or SNR, which quantifies how much a signal has been corrupted by noise. For an FMCW radar, it is defined as the ratio between received power and noise power:

$$\mathrm{SNR} = \frac{P_r}{N} \quad [\mathrm{W}] \tag{4.5}$$

The total noise power N has different contributions, namely thermal noise, phase noise (or FM noise, from Frequency Modulation) and Amplitude Modulation (AM) noise.

The thermal noise is generated by the random thermal motion of charge carriers inside an electric conductor. For a radar system, it is thermal noise generated by the receiver electronics that matters. The degradation of SNR in a receiver due to this thermal noise can be described by its noise factor F or the noise figure NF:

$$F = \frac{\mathrm{SNR}_{\mathrm{input}}}{\mathrm{SNR}_{\mathrm{output}}} \tag{4.6}$$

$$\mathrm{NF} = 10 \cdot \log_{10}\left(\frac{\mathrm{SNR}_{\mathrm{input}}}{\mathrm{SNR}_{\mathrm{output}}}\right) = 10 \cdot \log_{10}(F) \tag{4.7}$$

where $\mathrm{SNR}_{\mathrm{input}}$ and $\mathrm{SNR}_{\mathrm{output}}$ represent SNR at receiver's input and output, respectively.

The thermal noise power due to environmental temperature alone and measured at receiver's input is defined as:

$$N_0 = k \cdot B \cdot T_0 \quad [\mathrm{W}] \tag{4.8}$$

where $k = 1.38 \cdot 10^{-23}$ J/K is the Boltzmann's constant, B is the operational bandwidth of the radar, and T_0 is the ambient temperature of 290 K. For the 12 GHz operational bandwidth, the thermal noise power due to environmental temperature is -73.2 dBm.

Overall noise power takes into account also the thermal noise due to receiver's electronics. Our receiver consists of LNA with noise figure $\mathrm{NF}_{\mathrm{LNA}}$ = 2.5 dB and gain G_{LNA} = 28 dB, and a mixer with $\mathrm{NF}_{\mathrm{MIX}}$ = 10.5 dB. The RF-port is supposed to be connected to the antenna array via a series of

SP6T switches with 3 dB insertion loss, and about 1 m long RF-cable with 1 dB attenuation, which means NF_{SW} = 4 dB and G_{SW} = -4 dB.

The overall receiver's noise factor can be computed with the Friis Formula for cascaded devices:

$$F = F_{SW} + \frac{F_{LNA} - 1}{G_{SW}} + \frac{F_{MIX} - 1}{G_{SW} \cdot G_{LNA}} \tag{4.9}$$

where all terms are numeric ratios and are not in dB. The overall noise figure for a cascade, expressed in dB is simply

$$NF = 10 \cdot \log_{10}(F) \quad [\text{dB}] \tag{4.10}$$

Another important characteristic of a radar receiver is its noise temperature, which is computed as:

$$T_N = (F-1) \cdot T_0 \quad [\text{K}] \tag{4.11}$$

For the selected components the noise figure equals 6.5 dB, which gives a noise temperature of 1017.2 K. Note that the gain of LNA compensates for the high noise figure of mixer.

From this, the thermal noise power generated by the receiver's electronic and measured at receiver's input can be computed as:

$$N_{Th} = k \cdot B \cdot T_N \quad [\text{W}] \tag{4.12}$$

where $k = 1.38 \cdot 10^{-23}$ J/K is the Boltzmann's constant, B is the operational bandwidth of the radar, and T_N is the noise temperature computed above. The thermal noise power generated by the receiver's electronic is thus -67.7 dBm.

The total noise power at the receiver's input can finally be determined as:

$$N_{RX\_in} = N_0 + N_{Th} = k \cdot B \cdot (T_N + T_0) = k \cdot B \cdot F \cdot T_0 \quad [\text{W}] \tag{4.13}$$

which in this case is -66.7 dBm.

However, in a FMCW Radar, the effect of noise on the received signal is better evaluated at mixer's output, where the time domain beat frequency signal is transformed in the frequency domain via FFT for analysis. This operation essentially consists in band pass-filtering the beat signal with a bandwidth $B_{out} = 1/T_{sweep}$, and it spreads the noise power over all the available range bins, consequently increasing the SNR by a factor equal to the time-bandwidth product of the frequency modulated signal, $B \cdot T_{sweep}$.

Therefore, the total noise power at receiver's output can be computed via:

$$N_{RX\_out\_FFT} = k \cdot F \cdot B_{out} \cdot T_0 \cdot G_{REC} = \frac{k \cdot F \cdot T_0 \cdot G_{REC}}{T_{sweep}} \quad [W] \tag{4.14}$$

where G_{REC} represents the total gain of the receiver:

$$G_{REC} = G_{switch} \cdot G_{LNA} \cdot G_{mixer} \tag{4.15}$$

From this, noise power at receiver's output is -122.5 dBm.

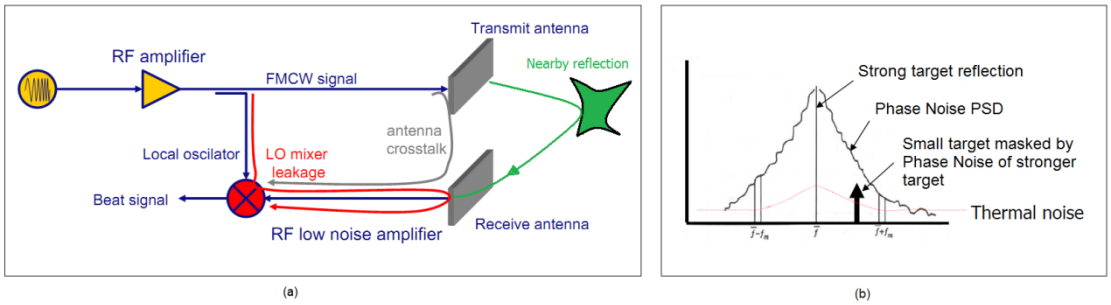

Figure 4.2: a) Typical phase noise contributions of an FMCW radar [17]; b) Example of signal affected by phase noise.

4.2.1 Phase noise estimation

Anyhow, the noise level in an FMCW receiver is often higher than expected from thermal noise alone, due to phase (or frequency modulation, FM) noise and amplitude modulation (AM) noise.

Phase noise is a measurement of phase and frequency perturbations added to the input signals by the receiver's frequency-conversion oscillators. The effect of phase noise is that after the down-mixing stage of the receiver, the signal power is spread to adjacent frequencies in the synthesized

range profiles, resulting in noise sidebands that degrade the receiver's sensitivity, possibly obscuring weaker echoes, as shown in figure 4.2 (b).

However, the frequency of the received signal is partially correlated with the transmitted frequency. The level of correlation decreases over time (decreases with increasing leaking signal path delay). The net effect is that the transmitter phase noise must be weighted by a correlation factor, estimated as:

$$C_{ph}=4(\sin(\pi f_{beat} T_d))^2 \qquad (4.16)$$

where f_{beat} is the beat frequency and T_d is the time delay between the LO and the reflection causing the phase noise.

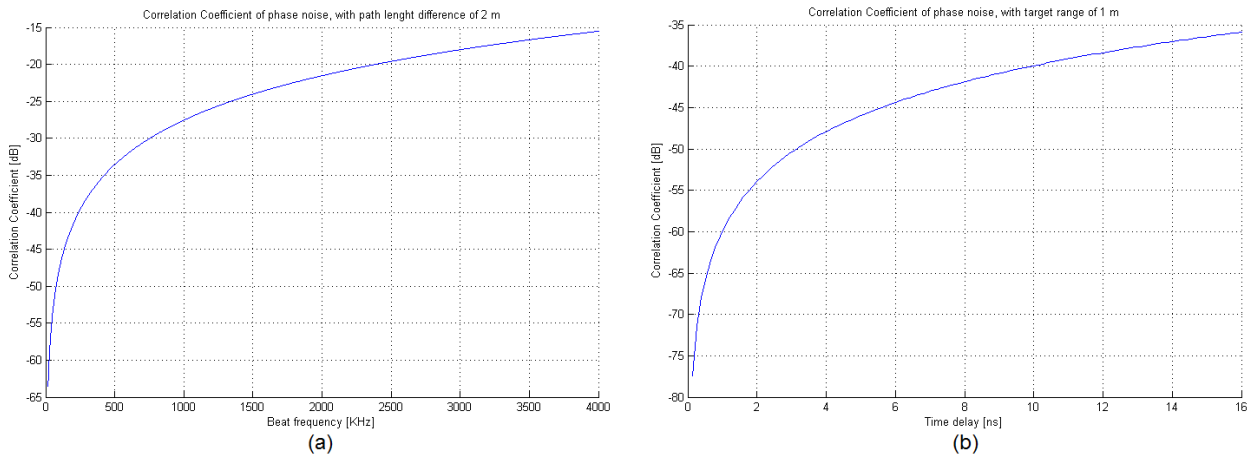

Figure 4.3: a) correlation coefficient vs beat frequency; b) correlation coefficient vs time delay (b).

In a dual antenna FMCW radar, phase noise is mainly caused by signals coupled from the transmit channel into the receive channel, like LO mixer leakage or antenna cross-talk, and by strong reflections at a short distance from the receiver. Phase noise typically decreases with 6 dB per octave.

AM noise levels are typically much lower than FM noise, but their decay is slower (3 dB/octave). In addition, AM noise doesn't have a correlation effect like FM noise.

In the following pages, the influence of phase noise on total noise at receiver's output is investigated.

The YTO by Microlambda Wireless selected for the UWB radar only specifies a phase noise value representing the combined effects of FM and AM noise, and thus we could only estimate their

combined contribution on total noise in the receiver. The manufacturer of the YTO specifies a single sideband phase noise density w.r.t. the carrier of -120 dBc/Hz, at 100 KHz offset.

Minimum beat frequency of interest, corresponding to the minimal target range of 0.5 m, is 80 KHz, and using the 6 dB/octave decay of phase noise, we can estimate it as -117.6 dBc/Hz at 80 KHz offset. Maximum beat frequency of interest, corresponding to the maximum target range of 2 m, is 320 KHz, and using the 6 dB/octave decay of phase noise, we can estimate it as -129.6 dBc/Hz at 320 KHz offset.

Furthermore, use of a frequency multiplier will degrade the phase noise of the YTO by a factor equal to $20 \cdot \log(N)$, where N represents its multiplication factor. In our case, with N=2, degradation of noise floor is about 6 dB, which is accounted in the following computation of each phase noise contribution.

Phase noise due to antenna cross-talk

$$N_{ant} = \frac{P_t \cdot S_\Phi \cdot C_{ant} \cdot G_{REC}}{T_{sweep} \cdot I_{ant}} \quad [W] \tag{4.17}$$

$$C_{ant} = 4\left(\sin\left(\pi \cdot f_{beat} \cdot \frac{\delta_{ant}}{c} \right) \right)^2 \tag{4.18}$$

where

P_t = 18.2 dBm (power driven to TX antenna);

S_Φ = -123.6 dBc/Hz (-129.6 dBc/Hz at 320 KHz offset, plus 6 dB degradation due to frequency multiplication);

C_{ant} = phase noise correlation coefficient for antenna cross-talk;

G_{REC} = total receiver Gain;

I_{ant} = isolation between transmit and receive antennas;

T_{sweep} = 500 μs;

δ_{ant} = path length difference between source-to-LO mixer port and source-to-tx-antenna-to-rx-antenna-to-RF port mixer (m) (grey path in fig. 4.2 (a));

c = speed of light, 3×10^8 m/s

Based on [5], we assume here an isolation of at least 25 dB between each transmit/receive antenna pair, and assume the target at maximum operational range of 2 m; for δ_{ant}, we have to

consider that maximum antenna coupling occurs for the minimal separation between transmit and receive antenna. For our MIMO array, we could estimate such distance as maximum 5 cm, not more.

Furthermore, by careful design of the different path lengths along the RF-board, it is possible to reduce the time delay between direct and leaking signal, thus increasing the correlation factor and reducing the effect of phase noise: if we consider about 1 m long RF-cables to connect radar front-end to antenna system, we would have then a total of 2.05 m between the coupler output and the mixer RF-input via antenna cross-talk; then if the path length between coupler's output at transmit side and the LO input of the mixer is also set to the same length, we can assume a δ_{ant} of a few cm. In this case, the phase noise due to antenna cross talk is estimated as -154.8 dBm, which is much lower than receiver noise of -122.5 dBm and its influence can be considered negligible.

Phase noise due to mixer LO leakage

$$N_{mix1} = \frac{P_t \cdot |\Gamma_{ant}|^2 \cdot S_\Phi \cdot C_{mix} \cdot G_{REC}}{T_{sweep} \cdot L_{cpl,f} \cdot L_{mix,iso}} \quad [W] \tag{4.19}$$

$$C_{mix} = 4\left(\sin\left(\pi \cdot f_{beat} \cdot \frac{\delta_{mix}}{\nu} \right) \right)^2 \tag{4.20}$$

where

P_t = 29.5 dBm (power at coupler's input);

S_Φ = -123.6 dBc/Hz (-129.6 dBc/Hz at 320 KHz offset, plus 6 dB degradation due to frequency multiplication);

$L_{cpl,f}$ = 10 dB (coupling factor);

$L_{mix,iso}$ = 20 dB (mixer LO-to-RF isolation);

C_{mix} = phase noise correlation coefficient mixer;

δ_{mix} = path length difference between source-to-LO mixer port and source-via-mixer-to-rx-antenna-to-RF port mixer (m) (red path in fig. 4.2 (a));

ν = propagation velocity of electromagnetic waves in coaxial cables, 2.3×10^8 m/s (corresponding to 76.6 % velocity factor).

;

For the worst case scenario, we assume the target at maximum operational range of 2 m; for δ_{mix}, we have to consider two-way distance between mixer and farthest receive antenna, which includes 1 m long RF-cable plus distance from center point of the 1x2m array to one of the corners, which we could also assume about 1 m long. The total two way path length δ_{mix} would then be at most 4 m. We assume here the leaking signal is not attenuated in its passage from output to input port of LNA (see red path in fig. 4.2 (a)), due to lack of information, although some attenuation is to be expected from realistic case.

In this case the maximum phase noise due to mixer LO leakage is estimated as -102.4 dBm, which is 26 dB higher than receiver noise and increases the total noise floor to -102.4 dBm.

An additional phase noise contribution due to mixer leakage is due to signal leaking from LO-port of the mixer to its RF-port, and finally converted to IF output. In this case the path length difference δ_{mix} between direct and leaked signal correspond to the internal path of the mixer, which is estimated as 2 cm.

$$N_{mix2} = \frac{P_t \cdot S_\Phi \cdot C_{mix2} \cdot G_{mix}}{T_{sweep} \cdot L_{mix,iso}} \quad [W] \tag{4.21}$$

In this case, the highest contribution is obtained for the higher expected beat frequency (320 KHz), and is estimated as -145.9 dBm.

Phase noise due short-range object

$$N_{obj} = 2\frac{P_t \cdot G_{tx} \cdot G_{rx} \cdot \lambda^2 \cdot \sigma_{obj} \cdot S_\Phi \cdot C_{obj} \cdot G_{REC}}{(4\pi)^3 \cdot L_{cpl,i} \cdot R^4 \cdot T_{sweep}} \quad [W] \tag{4.22}$$

$$C_{obj} = 4\left(\sin\left(\pi \cdot f_{beat} \cdot \frac{2R}{c}\right)\right)^2 \tag{4.23}$$

where

S_Φ = -111.6 dBc/Hz (-117.6 dBc/Hz at 80 KHz offset, plus 6 dB degradation due to frequency multiplication);

G_{tx} = 6 dBi (transmit antenna gain);

G_{rx} = 6 dBi (receive antenna gain);

λ = wavelength (m);

$L_{cpl,i}$ = mainline loss of coupler (insertion loss + coupling loss)

σ_{obj} = object radar cross section (m^2)

C_{obj} = phase noise correlation coefficient short-range object;

For the worst case scenario, we assume a target with 1 m^2 RCS at minimal operational range of 0.5 m (80 KHz beat frequency), and we use the highest wavelength in the operational bandwidth, corresponding to 5 cm (6 GHz). The maximum phase noise due to short-range object is estimated as -149.8 dBm.

Finally, we can estimate the influence of phase noise on total noise power at IF output by simple summation of each contribution.

In the following graphs, we estimated total noise power at mixer's output as a function of range to target. In figure 4.4 (a), the different phase noise contributions are reported for their maximum path length differences δ_{ant} and δ_{mix}, while the target range varies between 0.1 and 2.5 m, while figure 4.4 (b) compares the total phase noise with receiver noise and total noise power.

In conclusion, total phase noise, whose strongest contribution is given by signal leaking from LO port to-rx-antenna-to-RF port mixer (red path in fig. 4.2 (a)), in the worst case scenario increases total noise power by about 20 dB, for a total of 102.4 dBm.

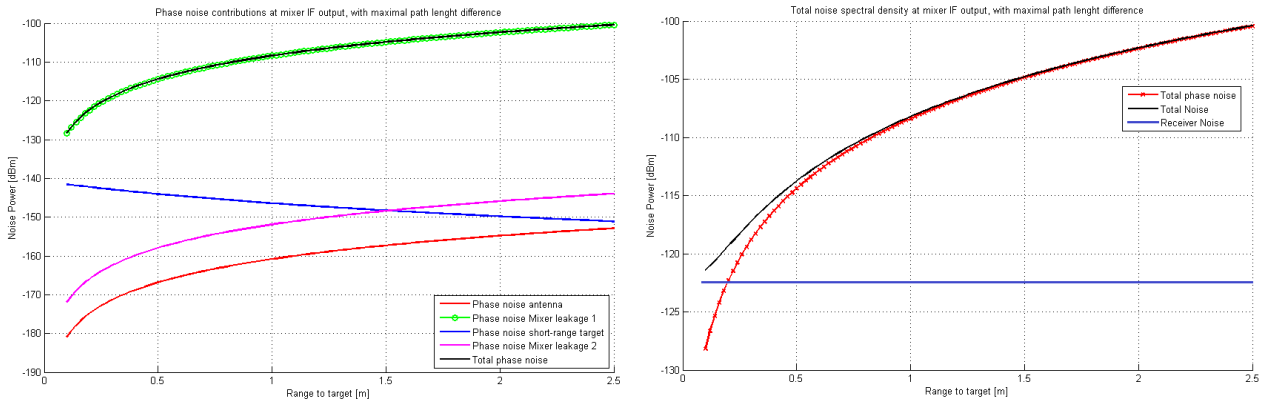

Figure 4.4: a) Phase noise contributions and b) comparison of total phase noise with thermal noise and total noise power vs. range.

4.3 Power Budget and Dynamic Range

The power budget is a characteristic of the radar that accounts for the transmitted power and noise floor of the receiver, and, as such, it defines the acceptable propagation loss of signal power:

$$\text{PowerBudget} = \frac{P_t}{\text{MDS}} \qquad (4.24)$$

where P_t represents signal power driven to the transmit antenna and MDS is the minimum detectable signal. Antenna gain is included into total propagation loss so it is omitted here. Our scheme drives 18.2 dBm of signal power into the transmit antenna, while minimum detectable signal is assumed to be 10 dB higher than noise floor. Then power budget is 110.6 dB at receiver output.

Dynamic Range is an important characteristic of the receiver that defines the range of received power within which the output power depends linearly on the input power. Dynamic Range can be determined at the receiver input in the following way:

$$\text{DynamicRange} = \text{P1dB} - G_{LNA} - G_{SW} - L_{cable} - N_{RX\_in} = P_{sat} - N_{RX\_in} \quad [\text{dB}] \qquad (4.25)$$

where P1dB is the least 1 dB compression point between LNA (output) and mixer (input). P_{sat} indicates the amount of input power which causes a 1 dB compression of the mixer's output.

In our case both the mixer and the LNA have a P1dB of 15 dB, which gives a P_{sat} = -9 dBm and a dynamic range at receiver's input of 57.7 dB.

Since both the power budget and the dynamic range depend on noise power they can be improved by signal processing, in particular by averaging which reduces the noise. Furthermore, FMCW signal processing is based on FFT that spreads the noise power over large frequency band and can be interpreted as averaging.

Actually, it makes more sense in our case to estimate the dynamic range at IF output, after FFT processing. At this stage, the dynamic range can be simply estimated as:

$$\text{DynamicRange}_{IF\_out} = \text{P1dB}_{LNA\_out} - G_{mix} - N_{RX\_out} = 15 - 12 - (-102.4) = 105.4 \quad [\text{dB}] \qquad (4.26)$$

4.4 Detectability Analysis

The estimation of detection capability of our RF-scheme requires computation of the power reflected from typical targets, such as a gun and a knife, at the maximum operational distance of 2 m.

The RCS of the gun and the knife were measured in the TU Delft's Anechoic Chamber (DUCAT), and the measurement setup and data processing are described in Appendix A. The measured RCS values are used to compute the received power, which is then compared to the total receiver noise to verify if the receiver is able to detect the targets. Given a maximum transmitted power of 18.2 dBm, the received power due to the target's reflection can be computed as:

$$P_r = P_t \frac{\sigma G_t G_r \lambda^2}{(4\pi)^3 R^4} \qquad (4.27)$$

where σ represents the RCS values measured in DUCAT. Transmit and receive gains are considered to be 6 dBi. The results over the 6-18 GHz bandwidth for target distance of 2 m and 1.5 m are shown in figures 4.5 (a) and 4.6 (a) respectively, where the noise power at receiver's input of -66.7 dBm is also depicted as a detectability threshold, while figures 4.5 (b) and 4.6 (b) represents the computed SNR at 2 m and 1.5 m respectively

At the maximum operational distance of 2 m, both targets show an acceptable SNR over the whole 6-18 operational frequency band. For the gun, the SNR at receiver input is between 17.5 and -0.3 dB, with an average SNR of 10.1 dB over the 6-18 GHz operational bandwidth, while for the knife the SNR varies between 5.6 and 14.7 dB, with an average SNR of 10.3 dB. Since reliable detection of radar echoes requires Signal-to-Noise Ratios in excess of 10 dB, we can say that the radar should be able to detect such targets at the maximum operational distance, based on their single-measurement SNR averaged over the 6-18 GHz band, although at higher frequencies (from 12 GHz) their SNR is constantly below the desired 10 dB.

Although detection of such target at the maximum operational distance of 2 m seems to be validated by their average SNR, in some cases it could be necessary to reduce their distance to 1.5 m, which would increase both the average and the minimal SNR by 5 dB, , as shown in table 4.1, and ensure a better detection capability. In any case, detection capability of the radar will be investigated also via simulation of the RF-scheme with ADS, and final decision on maximum operational distance will be made based also on the results presented in chapter 5.

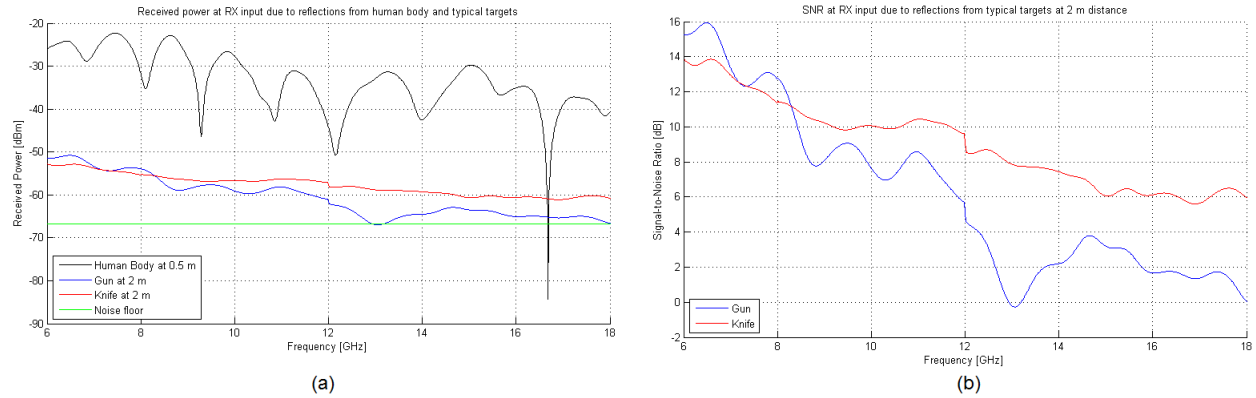

Figure 4.5: a) Received power due to reflection of typical targets at 2 m distance, compared with estimated reflections from human body at 0.5 m distance; b) measured Signal-to-Noise ratio due to reflections of typical targets at 2 m distance.

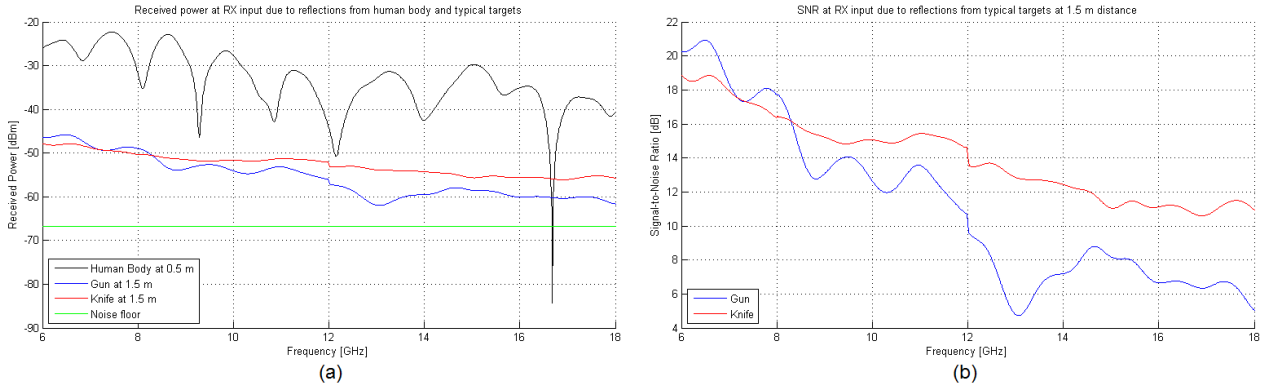

Figure 4.6: a) Received power due to reflection of typical targets at 1.5 m distance, compared with estimated reflections from human body at 0.5 m distance; b) measured Signal-to-Noise ratio due to reflections of typical targets at 1.5 m distance.

Target	Distance (m)	SNR min (dB)	SNR max (dB)	SNR average (dB)
Handgun	1	11.8	29.6	22.2
	1.5	4.7	22.5	15.1
	2	-0.3	17.5	10.1
Knife	1	17.6	26.8	22.3
	1.5	10.6	19.7	15.3
	2	5.6	14.7	10.3

Table 4.1: SNR of typical targets at different distances.

Furthermore, actual detection is performed at signal processing stage, and the SNR at the receiver input can still be improved by acquisition and sequential averaging of a number of sweeps.

We can define the Improvement Factor as

$$IF_{SNR} = 10\log_{10}(N_{av}) \quad [dB] \tag{4.28}$$

where N_{av} is the number of averages or sweeps, practically representing the number of repetitive measurements of the same target. Given a full-dataset acquisition time of 0.17 s, we could consider 10 measurements, for a total acquisition time of 1.7 s, which improves the SNR of 10 dB.

These values can be added to power budget and dynamic range that gives 120.6 dB and 115.4 dB respectively.

4.5 Conclusions

In this chapter a mathematical analysis of the performance of the selected multi-channel RF-scheme has been presented.

The power analysis shows that the output power at the transmitter side is about 18.2 dBm, and the designed radar can thus be considered a low power system. The mathematical analysis of the receiver side, characterized by a saturation point of -9 dBm at receiver's input, demonstrates that the stronger estimated signal at receiver's input, assumed to be due to reflection from human body at 0.5 m distance from the radar, is -22.3 dBm, and it doesn't saturate the receiver.

The noise analysis shows that the receiver has a noise figure of 6.5 dB, while the noise floor is estimated as -66.7 dBm at receiver's input, and -102.4 dBm at receiver output. Phase noise due to the combination of antenna crosstalk, mixer LO leakage and short-range targets was also estimated, and it has a considerable effect on noise power at IF output, increasing it from -122.5 to -102.4 dBm.

The power budget of the selected RF-scheme is 110.6 dB at receiver output, while its dynamic range was computed as 57.7 dB at the receiver input and 105.4 dB at receiver output after FFT.

The detectability analysis of typical targets like a handgun and a knife showed an acceptable average SNR of 10.1 dB for the gun and 10.3 dB for the knife when the targets are at 2 m distance from the radar. Although detection of such target at the maximum operational distance of 2 m seems to be validated by their SNR averaged over the 6-18 GHz band, in some cases it could be necessary to reduce their distance to 1.5 m to ensure a better detection capability. In any case, final selection of maximum operational range will be also based on results of ADS simulations, and is thus postponed to the next chapter.

Chapter 5: Simulation of the RF-scheme with ADS

In this chapter are presented the procedure and the results of the simulations of the basic RF-scheme for the UWB FMCW Radar Imaging system for concealed weapon detection, using Advanced Design System (ADS^{TM}) software.

For simplicity, we set-up a model reproducing the single-receive channel version of the RF-scheme discussed in the previous chapters, with the 6-18 GHz chirp signal generated by the combination of a 3-9 GHz YTO and frequency doubler. The signal power has been adjusted in order to replicate the expected signal power in each channel for the multichannel RF-scheme. As a consequence, the results of the simulations of the single channel receiver correspond to the results that would have been obtained for each channel of the selected 10-channel receiver.

In the first paragraph, a brief overview of ADS is given, explaining the type of simulation performed to evaluate the performance of the RF-scheme. Section 5.2 illustrates the objectives of the simulations and briefly explains which performance parameters have been evaluated through simulations. Section 5.3 illustrates in more depth the modeling process of the RF-schemes to be simulated. In section 5.4, the set-up of the simulation is explained. Section 5.5 gives the simulation results for the investigation on the influence of the harmonics generated by the RF-electronics at beat signal stage, together with solutions to decrease their effect. In section 5.6 a detectability analysis of the weakest estimated targets over the background of human body reflection is presented, while paragraph 5.7 presents the results on the investigation of down-range resolution obtained by the RF-schemes selected in paragraph 5.5. Section 5.8 simply gives the amplitude characteristics of the receiver, showing that strongest and weakest estimated received signals are within the linear characteristics of the receiver.

5.1 Brief overview of ADS

ADS is a software package which enables to simulate circuits and RF systems designed for specific objectives. ADS provides many types of simulators, including DC, AC, S-parameter, Harmonic Balance, Circuit Envelope, Transient and RF-Budget simulations. For our purposes, only one of these types of simulations has been used for this thesis report, namely Circuit Envelope simulations.

The Circuit Envelope simulator simulates high-frequency amplifiers, mixers, oscillators, and subsystems that involve transient or modulated RF signals. Circuit Envelope is highly efficient in analyzing circuits with digitally modulated signals, because the transient simulation takes place only around the carrier and its harmonics.

Circuit Envelope simulation uses a combination of time- and frequency-domain analysis techniques, providing a fast and complete analysis of complex signals such as digitally modulated RF signals. In practice, this simulator permits input waveforms to be represented in the frequency domain as RF carriers, with modulation "envelopes" that are represented in the time domain. For more information about Circuit Envelope simulations, the reader is referred to [29].

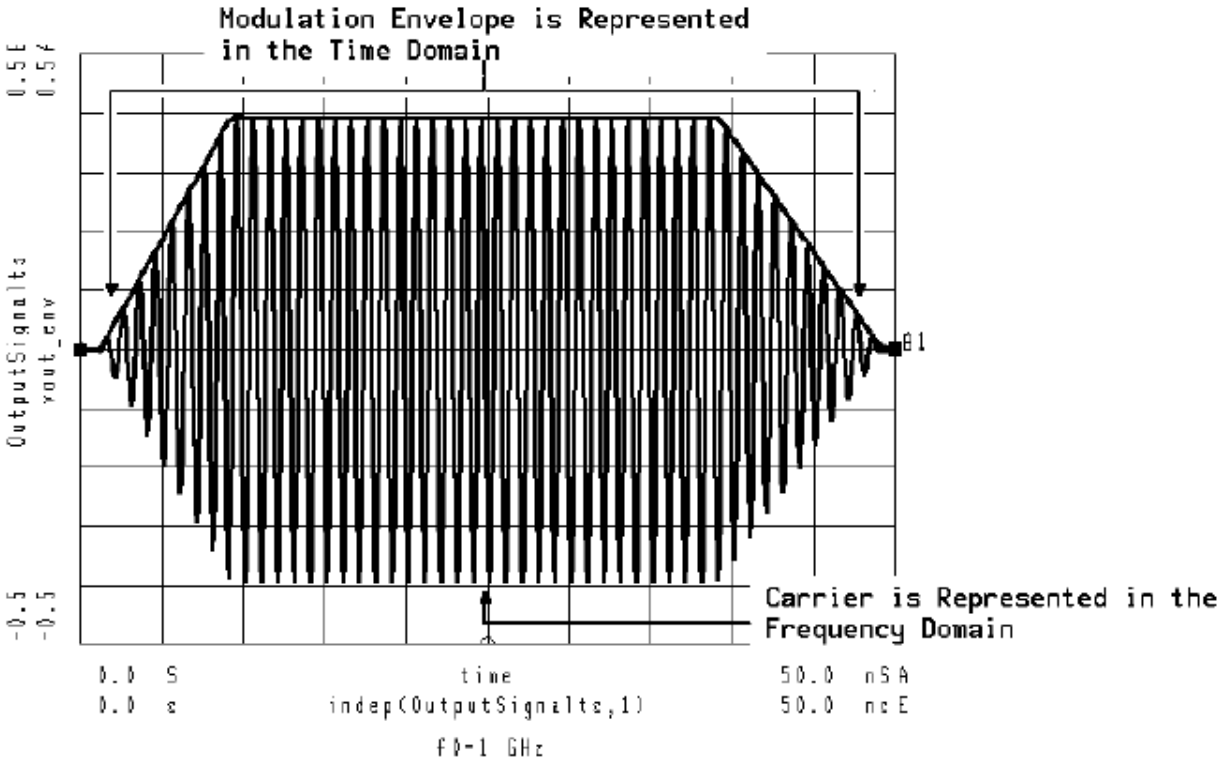

Figure 5.1: Modulated signal in the time-domain [29].

5.2 Objectives of the simulations

Simulations in ADS were performed with the purpose of investigating the influence of harmonics generated by the RF-electronics on the beat signal at receiver's output. The combination of YTO and frequency doubler, used to generate the desired 6-18 GHz chirp signal, also generates harmonics that could be interpreted as additional targets at the beat signal stage. The main objective of the simulations presented in this chapter is to estimate the level of these extra beat frequencies with respect to the fundamental beat signal, in order to speculate on maximum 2nd harmonic level required at the generator to achieve a harmonics-free beat signal and, if necessary, to investigate alternative solutions to suppress their influence at beat signal stage when simulating realistic circuit. As it will be shown later in this chapter, an octave band RF-scheme using a 9-18 GHz chirp signal was also simulated as an alternative to the main multi-octave band RF-scheme, in order to show the difference in harmonic influence between the two cases.

Important properties of the RF-scheme that need verification are the detectability of the weakest estimated reflections from typical targets (a handgun and a knife) and the ability to separate reflection from two close targets, i.e. its down-range resolution.

In addition, we simulated different application scenarios, in order to investigate the saturation point and minimum detectable signal, and determine the amplitude characteristic of the receiver.

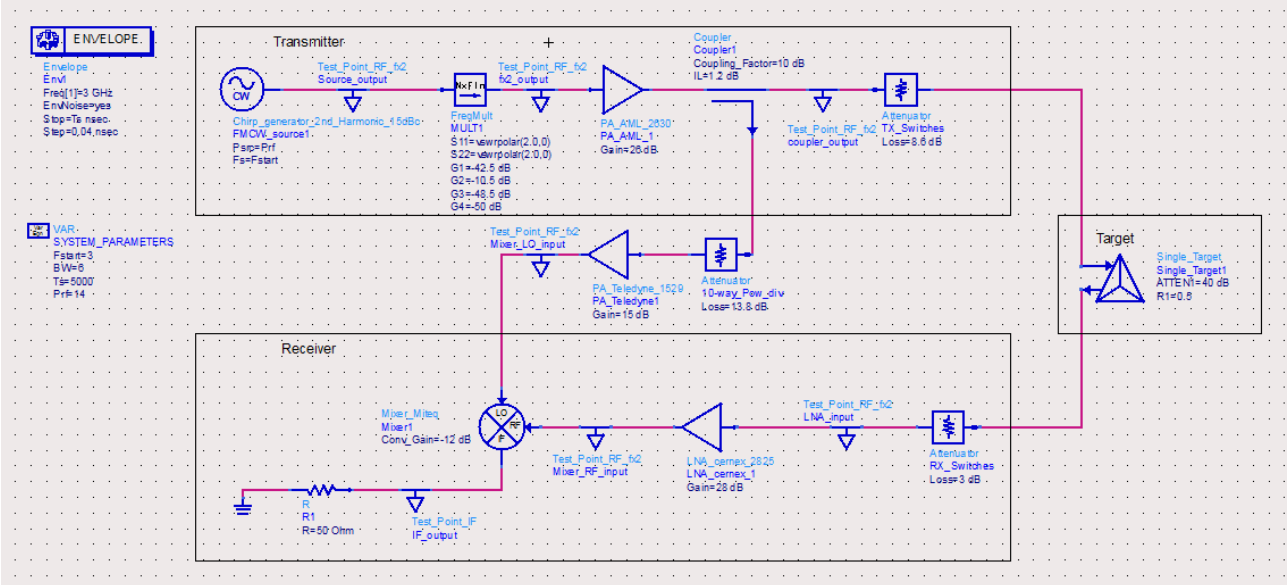

Figure 5.2: ADS model of basic single-channel RF-scheme of the UWB FMCW Radar.

5.3 Modeling of basic RF-scheme for UWB FMCW radar system

The ADS model of the basic RF-scheme of the UWB FMCW radar system is shown in figure 5.2. As already mentioned earlier, we simulated for simplicity a single channel receiver, but the results are representative of each channel of the final multi-channel receiver. The basic RF-scheme is mainly made of three blocks: the transmitter, the target and the receiver.

Every component simulated here reproduces as closely as possible the RF-components that were selected for the RF-scheme in chapter 3. Before going into detailed description, we should introduce some recurring parameters that are going to be used in several instances:

- The sweep time T_s, also representing in our models the total simulation time, that according to real component specifications should be set to 500 μs, but it was reduced to 5 μs due to software limitations.
- The chirp excursion BW, which represents the frequency band of the fundamental chirp signal, set to 6 GHz;
- The start frequency of the chirp F_s, set to 3 GHz.

5.3.1 Modeling of the transmitter

The model of the transmitter basically consists of an RF-signal generator, producing a 3-9 GHz chirp signal with 14 dBm output power, followed by a frequency multiplier which provides the desired 6-18 GHz sweep. The frequency multiplier has the function to generate harmonics of the input signal; the output power of each harmonic signal can then be controlled by changing the gain of the frequency multiplier.

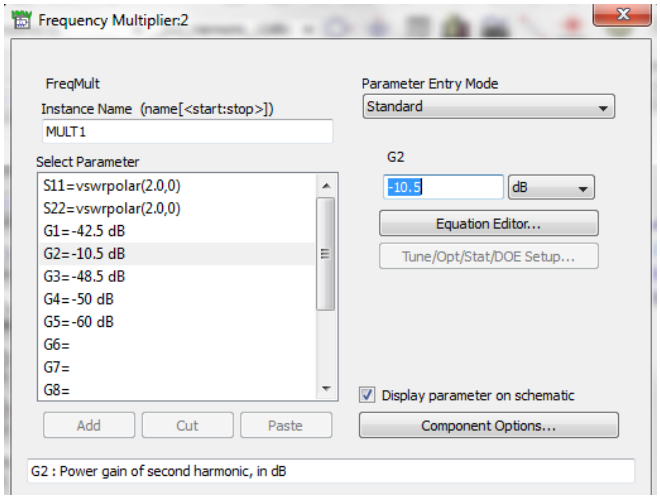

Figure 5.3: Selection of parameters of frequency multiplier

In our specific case, the desired 6-18 GHz output signal corresponds to the second harmonic, and it is decreased by 10.5 dB (representing the conversion loss of the selected frequency doubler) w.r.t the fundamental input harmonic; the other harmonics are suppressed much more, with the fundamental harmonic decreased by 42.5 dB, the third by 48.5 dB, the fourth by 50 dB and the fifth by 60 dB, as shown in figure 5.3. Thus the main signal at the frequency multiplier output is the second harmonic. The frequency doubler is followed by a 26 dB gain power amplifier which increases the main signal power to 29.5 dBm. A 10 dB directional coupler with 1.2 dB insertion loss will then split the signal over two branches, providing both the reference signal for the LO mixer input (18.2 dBm at coupled port output) and the signal to be driven to the transmit antenna, which is further reduced by an attenuator reproducing the insertion loss of the transmit switches (8.6 dB in total). Attenuation due to RF-cables connecting the RF-board to the antenna system at both transmit and receive sides are taken into account in the target model, as an additional attenuation of 1 dB each. The total power coming out of the transmitter block is then 19.2 dBm.

For the chirp signal generator, two different models were realized, one ideal (without harmonics) and one realistic (with -15 dBc harmonics), and they are presented next.

5.3.2 Modeling of ideal chirp signal generator

The ideal chirp generator is simply modeled with a RF Pulse Train power source component, as shown in figure 5.4, on the left. In ADS, this RF pulse power source creates a pulse modulated RF carrier with optional frequency chirping, and by proper setting of width and period of the pulse, it is possible to simulate the transmission of a single chirp signal.

As a matter of fact, rise and fall time of the pulse are set to 1 ns, while width is set to $T_s - 2$ (ns), were T_s represents both the sweep time and the total simulation period. Setting the pulse period equal to T_s ensures the generation of a single chirp signal. The other parameters set for the model are the start frequency of the sweep, F_s (GHz), and the chirp frequency excursion BW (GHz). No harmonics were considered in the modeling of the ideal chirp generator.

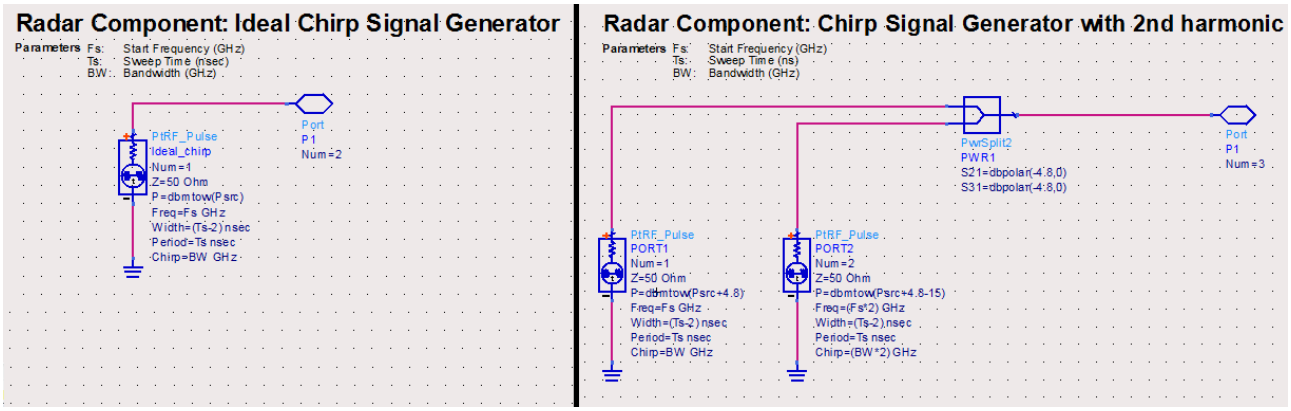

Figure 5.4: ADS Model of ideal chirp generator (left) and realistic chirp generator with -15 dBc second harmonic (right).

5.3.3 Modeling of realistic chirp signal generator

The model of the realistic chirp signal generator is shown in figure 5.4, on the right. As it can be seen, two RF Pulse Train power source components are used for this model: the first one simulates the fundamental 3-9 GHz chirp with an output power equal to P_{src}, which represents the source output power of +14 dBm, while the second one represents the 6-18 GHz 2nd harmonic chirp signal, which was set to a -15 dBc level, thus with an output power of -1 dBm. The start frequency of the 2nd harmonic chirp signal is set as twice F_s and its bandwidth is also twice BW. A power splitter is then used to combine the two signals. The 4.8 dB loss due to power splitting is balanced by the 4.8 dB increment in output power in both power sources.

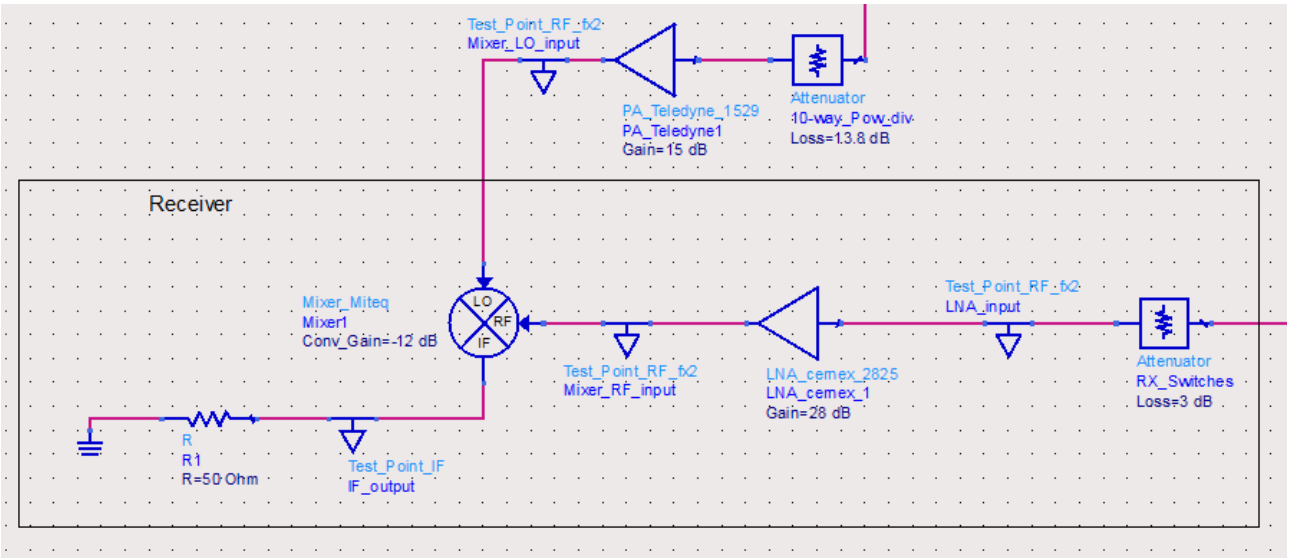

Figure 5.5: ADS model of receive channel.

5.3.4 Modeling of the receiver

The ADS model of the receiver block is shown in figure 5.5. It mainly consists of a cascade of a LNA and a mixer or down-converter: the LNA has the function to amplify the signal at the receiver input, while the mixer is used to deramp the received chirp signal. This is achieved by mixing the RF input of the mixer, corresponding to the received signal amplified by the LNA, with the LO input consisting of the reference signal coming from the transmitter. This mixing process produces the beat signal at the IF output.

The LNA is modeled with the same basic component used for the Power Amplifiers. To reproduce the LNA component selected in chapter 3, we set the gain to 28 dB, the noise figure to 2.5 dB and the output P1dB to 15 dBm.

Although the RF-scheme selected in chapter 3 includes an IQ mixer, for our objectives it is not necessary to simulate such a device, and a simpler down-converter is thus used. This model includes a mixer component, with conversion gain set to -12 dB and noise figure set to 7.5 dB, which corresponds to the double sideband noise figure of the selected IQ mixer, as opposed to the single sided noise figure of 10.5 dB which is given in the component's datasheet. We also set the input P1dB at 15 dBm. In order to take into account the realistic IF bandwidth at the mixer's output, the mixer model also includes a DC-500 MHz low-pass Butterworth filter, as shown in figure 5.6.

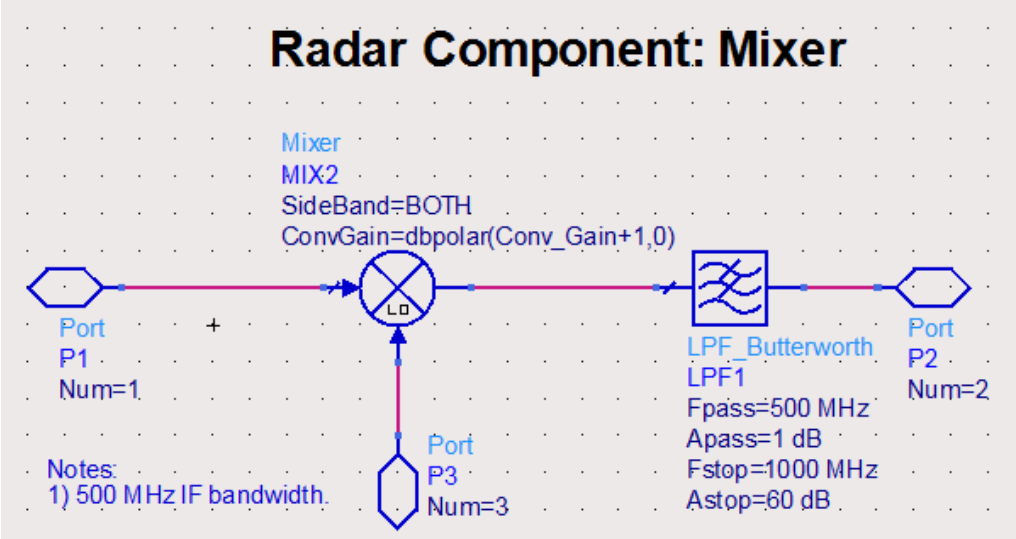

Figure 5.6: ADS model of mixer with DC-500 MHz IF bandwidth.

In order to account also for the insertion loss due to the receive switches, a 3 dB attenuator precedes the LNA in the proposed model. In addition, the reference signal which is input to the mixer LO port, is previously attenuated by 13.8 dB, to take into account the sum of coupling and insertion loss due to the 10-way power splitter used to provide the LO reference signal to each one of the intended 10 receive channels, and then amplified by a power amplifier reproducing the model A2CP18629 described in chapter 3, with 15 dB gain. At LO mixer input, the reference signal is then 19.5 dBm.

5.3.5 Modeling of targets

For the target model, there are mainly two factors to be considered: the attenuation of the received signal w.r.t to the transmitted waveform, due to propagation loss and reflection from the target, and the time difference between transmission and reception due to the two-way travel time of the signal from radar to target and backwards. In ADS, the attenuation can be modeled with an attenuator, while travel time and therefore distance to target is modeled with a Time-Delay component.

Figure 5.7 shows the modeling of a single target (left image), consisting of an attenuator, a Time-Delay component and two isolators. The isolators simply avoid reflections of part of the signal in the opposite direction, and are used here to decrease the influence of targets modeling on transmitter and receiver; in addition, the 1 dB loss of each isolator represents the attenuation due to RF-cables at both transmit and receive side (1 dB each).

Modeling of multiple targets is also possible, with the use of multiple attenuators and time-delays, like shown in figure 5.7, on the right. The parameters of each target can be set independently.

For this model, two important parameters have to be set-up:

- ATTENn [dB, positive value], which represents the attenuation of the signal due to propagation of the electromagnetic wave in free space and reflection from the n^{th} target; the subtraction by 2*4.8 in the Loss parameter is performed in order to balance the losses due to the use of power splitters.
- TDn [nsec], which represents the radar-target two-way travel time from the n^{th} target, and is computed using the parameter Rn [m], which represents the distance between the radar and the n^{th} target.

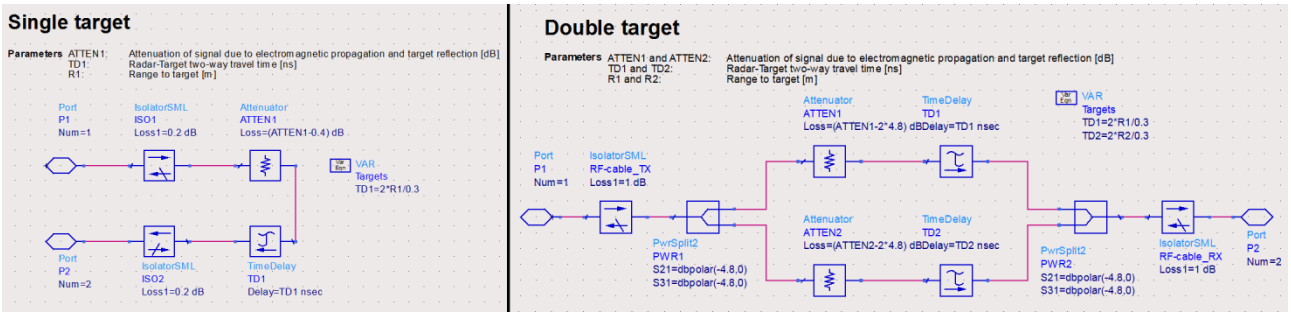

Figure 5.7: ADS models of single target (left) and double target (right).

5.4 Set-up of Circuit Envelope simulations

Once modeling of the realistic RF-scheme is complete, it is necessary to set-up the parameters for the specific simulation to be performed. ADS provides a different controller for each type of simulator, to allow defining several different aspects of the simulation to be performed.

For the circuit envelope simulation, the primary parameters to be set-up are the stop time, which simply defines the time the simulation stops, and time step, which sets the fixed time step that the simulator uses to calculate the time-varying envelopes. In our specific case, the stop time corresponds to the sweep time of the transmitted signal, T_s. This parameter is very important as it also determines the resolution bandwidth of the spectrum. Consequently, it has to be large enough to resolve spectral components of interest. On the other hand, the time step defines the maximum allowed bandwidth (± 0.5/Time step) of the modulation envelope, and is thus required to be small enough to capture the highest modulation frequencies. These relations are illustrated in figure 5.8, on the left.

Another important parameter to be set in the controller is the list of analysis frequencies and their harmonics. In any case, the software requires the analysis frequency to be the same set to F_s, the starting frequency of the source signal, in order to ensure the most precise results. This means that the analysis frequency is 3 GHz for the multi-octave band RF-scheme, and 4.5 GHz for the octave band RF-scheme. It is also important to properly set the number of harmonics to be considered in the simulation, indicated by the frequency order in fig 5.8 (right) and set to 5. This number can be explained by looking at the output signal of the frequency multiplier in the transmitter. For a 3-9 GHz input signal, the desired second harmonic signal (6-18 GHz) at the frequency multiplier's output will contain also part of the 3rd (9-27 GHz), 4^{rth} (12-36 GHz) and 5th (15-45) harmonics signals. In order to consider their effects in the beat signal, we set the harmonic number or frequency order to 5.

For the octave RF-scheme, the analysis frequency is again set to the starting frequency of the chirp signal, in this case 4.5 GHz, while the number of harmonics is set to 3.

Figure 5.8 (right) shows the ADS tab with the EC parameters set-up for the simulation of the multi-octave RF-scheme.

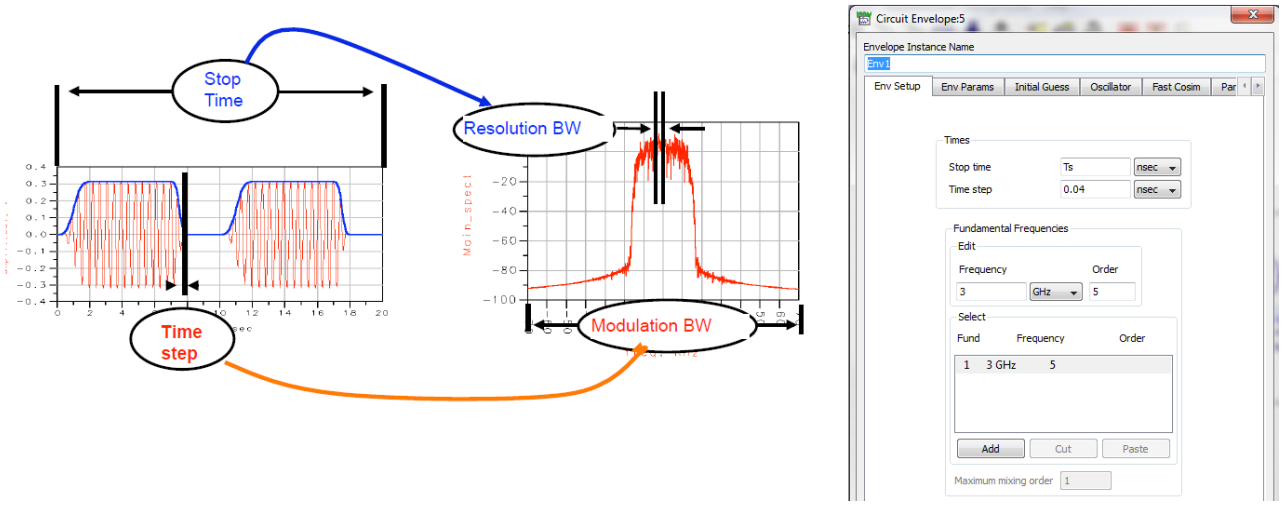

Figure 5.8: Relation between stop time and resolution bandwidth, and between time step and modulation bandwidth (left); Summary of primary parameters set-up for the EC simulation (right).

5.4.1 Technical limitations of the simulations

The performed simulations allow estimating the behavior of the RF-circuit with realistic results, but for some parameters a precise simulation was not possible.

The main limitation involves the stop time parameter T_s, which also represents the sweep time of the chirp generator. According to the selected YTO specifications, the stop time should be set to 500 µs, but due to software limitations, we set a stop time of 5 µs. The consequence on the

simulation results is that the beat signal due to reflections from a target will appear at a beat frequency which is 100 times higher than the true value, according to the formula:

$$f_{beat} = \frac{B}{T_{sweep}} \cdot \frac{2R}{c} \tag{5.1}$$

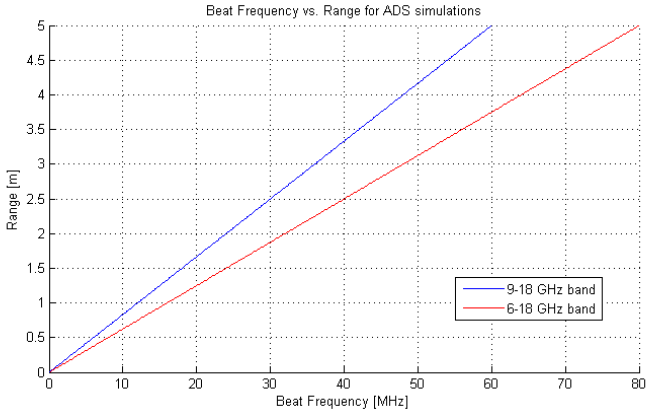

Figure 5.9: Beat frequency versus target range for the ADS simulations for both 6-18 GHz and 9-18 GHz frequency band RF-schemes.

In addition, the noise floor computed by ADS is influenced by the shorter sweep time, and it should thus result 20 dB higher than the total thermal noise power computed in section 4.2. However, the ADS models described here do not take into account the contributions due to phase noise, which actually increase total noise power by about 25 dB. This must be taken into account when evaluating the simulations results.

A more serious limitation is represented by the fact that the simulations don't take into account out-of-band behavior of the selected RF-components. As a matter of fact, the components' specifications used to set-up the RF-circuit to simulate, refer to their behavior in the 6-18 GHz band, while outside from this band these parameters rapidly worsen. Data on out-of-band behavior of selected RF-components was not available, and it was not possible to simulate it. Because of this, the influence of out-of-band harmonics on the simulations results is stronger than the reality, and we must take this into account when evaluating the simulation results.

5.5 Investigation on harmonics influence

In order to examine the radar performance in different situations, we simulated the RF-scheme for different application scenarios. As shown in the following paragraphs, two slightly different RF-

schemes were simulated: the multi-octave band RF-scheme, where a 6-18 GHz chirp signal is simulated, and the octave band RF-scheme, which instead uses a chirp signal covering the 9-18 GHz frequency band.

For both schemes, the simulation models have been designed to investigate the influence of harmonics at the beat signal stage. These harmonic signals are generated by both the YTO and the frequency doubler, and a careful investigation of their effect on beat signal should account their influence separately. Because of this, in the following each RF-scheme has been simulated at first without the frequency doubler, in order to evaluate the influence of only the YTO harmonics on the beat signal, and only then with the frequency doubler.

From now on, we will refer to the RF-schemes without frequency doubler as RF-scheme A1 for the multi-octave band 6-18 GHz sweep, and RF-scheme A2 for the octave band 9-18 GHz sweep. The RF-schemes using the frequency doubler are referred to as RF-scheme B1 for the multi-octave 3-9 GHz sweep, and RF-scheme B2 for the octave band 4.5-9 GHz sweep.

In order to ensure suppression of harmonics for any application scenario, we investigated the influence of the harmonics in the case of strongest received signal, which was estimated in section 4.1 from measurement of reflections from a human body at 0.5 m distance. If their influence is suppressed in such case, then for weaker signals their suppression will be even stronger.

For this, the attenuation in the target model was set to replicate the lower propagation loss for the stronger received signal, estimated in section 4.1 as 40.5 dB, and approximated in these simulations to 40 dB. The results of these simulations are presented in the next paragraph.

5.5.1 Simulation of RF-schemes A1 and A2

The parameters used in these simulations for investigation of harmonic influence are shown in the list below:

RF-scheme	System Parameters			Target parameters	
	F_s (GHz)	BW (GHz)	T_s (ns)	Attenuation (dB)	Range (m)
A1	6	12	5000	40	0.5
A2	9	9	5000	40	0.5

Table 5.2: Settings of the simulation parameters for the two RF-schemes without frequency doubler.

The chirp generator directly generates the full band chirp signal without the use of a frequency doubler. In order to keep a comparable signal power in every simulation, for the RF-schemes A1

and A2 the output power of the source was set to 3.5 dBm, which corresponds to the output power of the selected YTO (14 dBm), minus the conversion loss (10.5 dB) of the frequency doubler. The results for both RF-schemes are presented in the following paragraphs, both for the ideal case with no harmonics and the real case with 2nd harmonics at -15 dBc level in the YTO.

5.5.1.1 Simulation for ideal 6-18 GHz chirp signal: RF-scheme A1

The simulation results for ideal RF-scheme A1 are shown in figure 5.10.

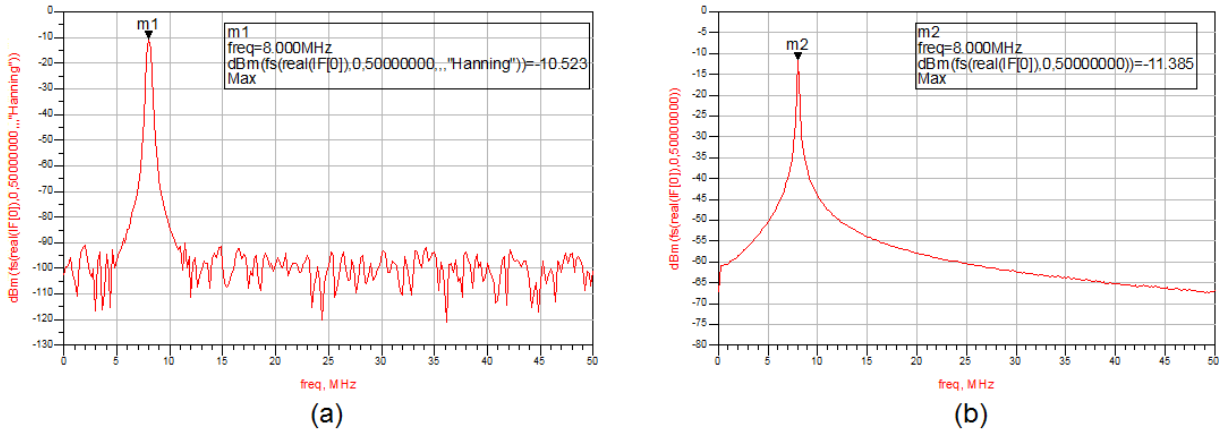

Figure 5.10: Simulation results for ideal RF-scheme A1: a) beat signal for Hanning window; b) raw beat signal.

The peak in the beat signal, corresponding to -10.5 dBm, correctly appears at 8 MHz, resulting from:

$$f_{beat} = \frac{B}{T_{sweep}} \cdot \frac{2R}{c} = \frac{12\times10^{9}}{5\times10^{-6}} \cdot \frac{2\times0.5}{3\times10^{8}} = 8.00 \quad \text{MHz} \tag{5.2}$$

5.5.1.2 Simulation for realistic 6-18 GHz chirp signal: RF-scheme A1

The simulation results for the realistic RF-scheme A1 with -15 dBc 2nd harmonic are shown in figure 5.11.

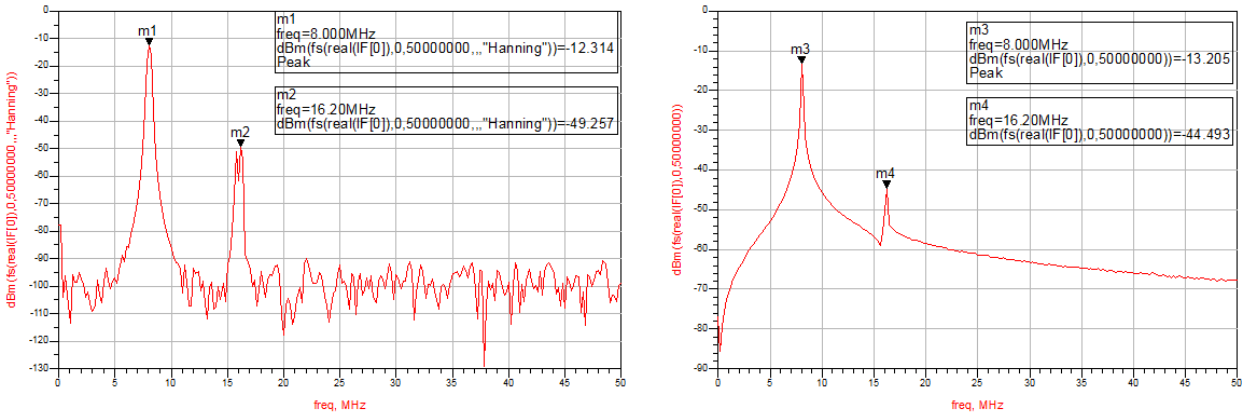

(a) (b)

Figure 5.11: Simulation results for ideal multi-octave RF-scheme, without frequency doubler: a) beat signal for Hanning window; b) raw beat signal.

The main peak in the beat signal (-12.3 dBm) at 8 MHz corresponds to the fundamental harmonic signal, while the second and lower peak (-49.3), appearing at 16 MHz, is generated by the second harmonic produced in the source. At beat signal stage, the second harmonic level is decreased from -15 dB to about -37 dB with respect to main beat for Hanning window.

5.5.1.3 Simulation for ideal 9-18 GHz chirp: RF-scheme A2

The simulation results for ideal RF-scheme A2 are shown in figure 5.12.

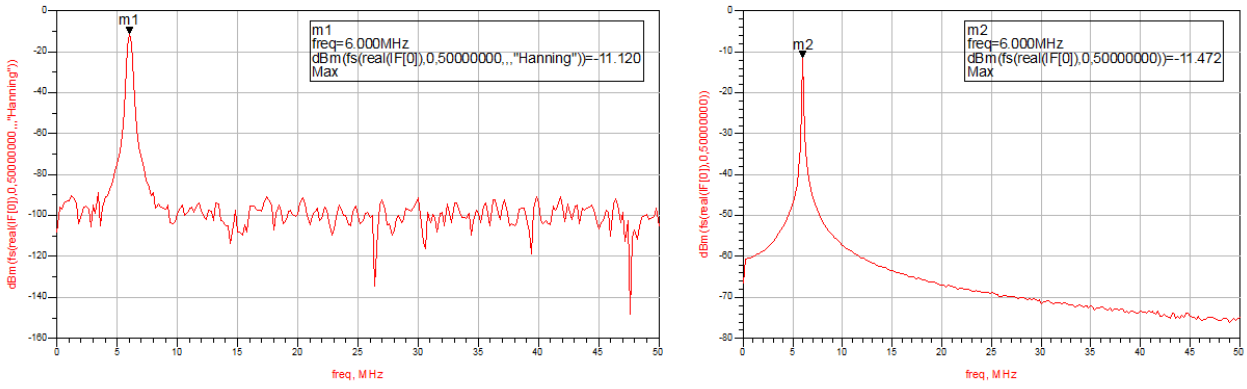

(a) (b)

Figure 5.12: Simulation results for ideal RF-scheme A2: a) beat signal for Hanning window; b) raw beat signal.

The peak in the beat signal, corresponding to -11.1 dBm, correctly appears at 6 MHz, resulting from:

$$f_{beat} = \frac{B}{T_{sweep}} \cdot \frac{2R}{c} = \frac{9\times10^{9}}{5\times10^{-6}} \cdot \frac{2\times0.5}{3\times10^{8}} = 6.00 \quad \text{MHz} \tag{5.3}$$

5.5.1.4 Simulation for realistic 9-18 GHz chirp: RF-scheme A2

The simulation results for realistic RF-scheme A2 are shown in figure 5.13.

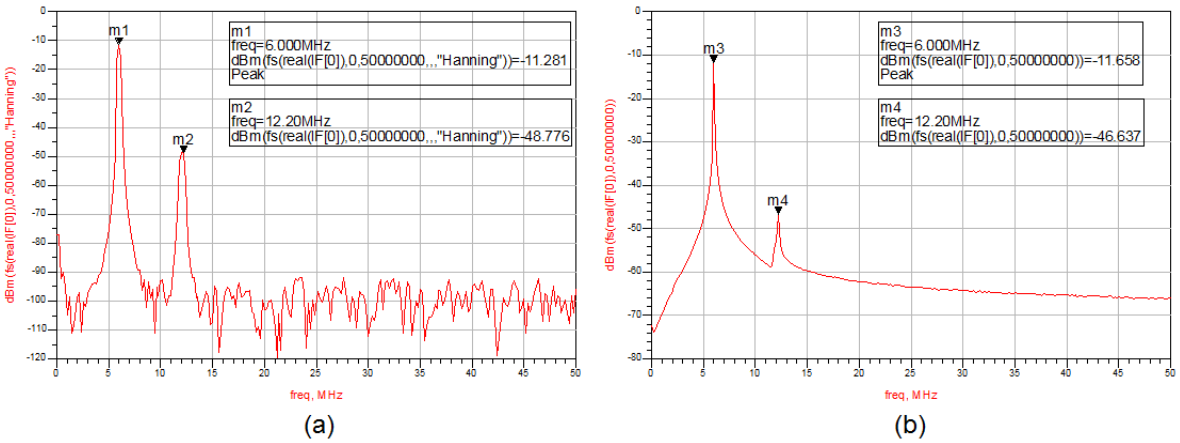

Figure 5.13: Simulation results for realistic RF-scheme A2: a) beat signal for Hanning window; b) raw beat signal.

The main peak in the beat signal at 6 MHz (-11.3 dBm) corresponds to the fundamental harmonic signal, while the second and lower peak (at -48.8 dBm), appearing at 12 MHz, is generated by the second harmonic produced in the source. At beat signal, the second harmonic level is again decreased from 15 dBc to about 37 dBc for the Hanning window.

By comparison, RF-schemes A1 and A2 obtain the same 2nd harmonic suppression, and in both cases the 2nd harmonic generates extra-beat frequencies that can be erroneously interpreted as a target. Thus none of the two schemes is suited to our objectives the way it is.

In order to evaluate the required 2nd harmonic level which would cause the extra-beat frequencies to be at a level comparable with the -102.5 dBm noise floor, we performed simulations with lower 2nd harmonic levels. From this we estimated that in order to get rid of extra-beat frequencies, the 2nd harmonic level in the source should be around -40 dBc, as shown in figure 5.14, where no harmonics pops up above the noise floor:

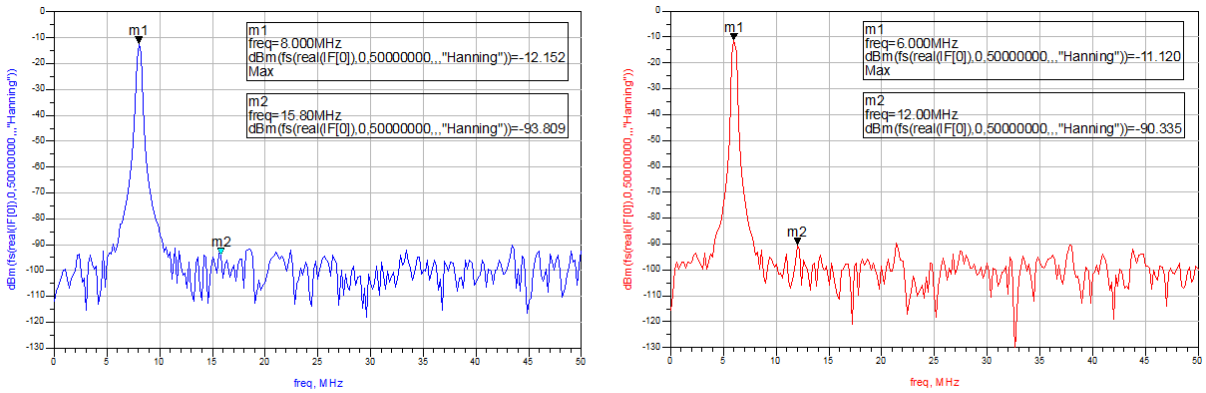

Figure 5.14: Beat signals for Hanning window of realistic RF-schemes, with -40 dBc 2nd harmonic: a) RF-scheme A1; b) RF-scheme A2.

5.5.2 Simulation of RF-schemes B1 and B2

The parameters used in these simulations for investigation of harmonic influence are shown in the list below:

RF-scheme	System Parameters			Target parameters	
	F_s (GHz)	BW (GHz)	T_s (ns)	Attenuation (dB)	Range (m)
B1	3	6	5000	40	0.5
B2	4.5	4.5	5000	40	0.5

Table 5.3: Settings of the simulation parameters for the two RF-schemes with frequency doubler.

The source generates a chirp signal which is then passed through a frequency doubler to achieve the required sweep bandwidth. The results for RF-schemes B1 and B2 are presented next, both for the ideal case with no harmonics and the real case with 2nd harmonics at -15 dBc level in the YTO.

5.5.2.1 Simulation for ideal 3-9 GHz chirp: RF-scheme B1

The simulation results for ideal RF-scheme B1 are shown in figure 5.15.

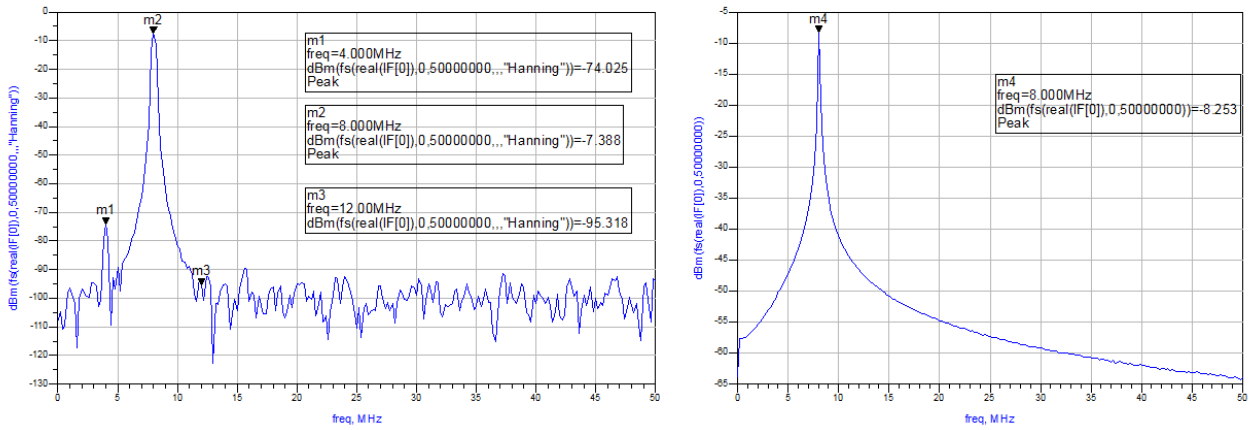

Figure 5.15: Simulation results for ideal RF-scheme B1: a) beat signal for Hanning window; b) raw beat signal.

Given the 3-9 GHz chirp signal, the beat frequency of the fundamental chirp is computed as:

$$f_{beat} = \frac{B}{T_{sweep}} \cdot \frac{2R}{c} = \frac{6\times10^{9}}{5\times10^{-6}} \cdot \frac{2\times0.5}{3\times10^{8}} = 4.00 \quad \text{MHz} \tag{5.4}$$

Due to frequency doubling, the expected main peak in the beat signal appears at 8 MHz, with a magnitude of -7.4 dBm, corresponding to the 2nd harmonic output of the frequency doubler. However figure 5.15 also shows a smaller peak (-74 dBm) at 4 MHz, caused by the fundamental harmonic of the 3-9 GHz chirp signal. This means that also the frequency doubler contributes to generate extra beat frequencies, although its relative influence is much smaller than that of 2nd harmonic generated by the YTO. If the frequency doubler had the ability to suppress the fundamental harmonic in the same way as it does with the third harmonic, there would have been no extra-beat frequency, as shown in figure 5.16.

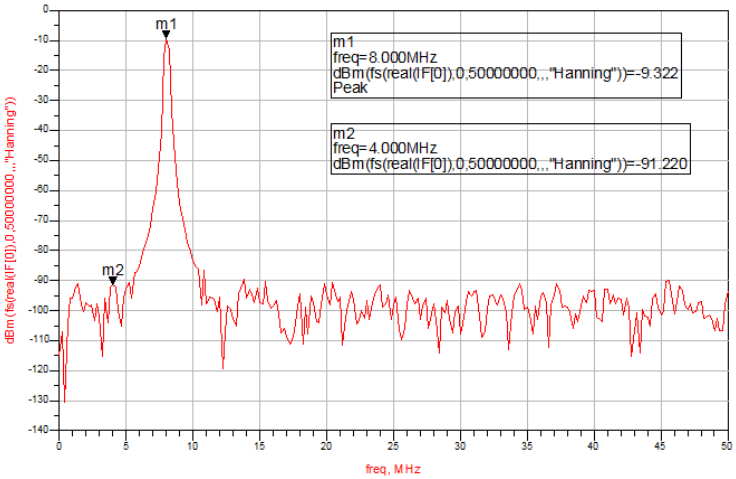

Figure 5.16: Beat signal of RF-scheme B1 with ideal generator and with fundamental harmonic suppression of frequency doubler increased by 6 dB w.r.t real specifications.

5.5.2.2 Simulation for ideal 4.5-9 GHz chirp: RF-scheme B2

The simulation results for the ideal RF-scheme B2 are shown in figure 5.17.

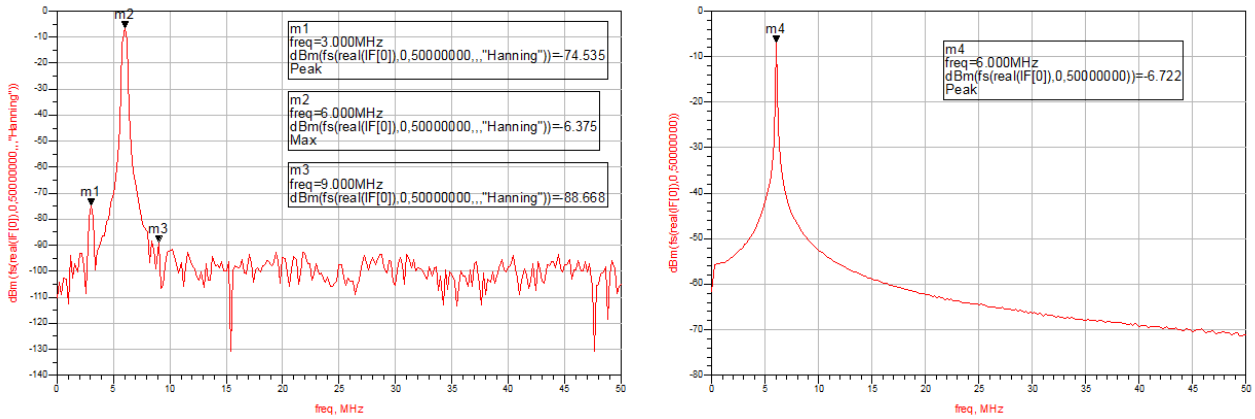

Figure 5.17: Simulation results for ideal RF-scheme B2: a) beat signal for Hanning window; b) raw beat signal.

The results are similar to the RF-scheme B1, with the frequency doubling suppression of fundamental harmonic not low enough.

5.5.2.3 Simulation for realistic 3-9 GHz chirp: RF-scheme B1

The simulation results for realistic RF-scheme B1 with -15 dBc 2nd harmonic are shown in figure 5.18.

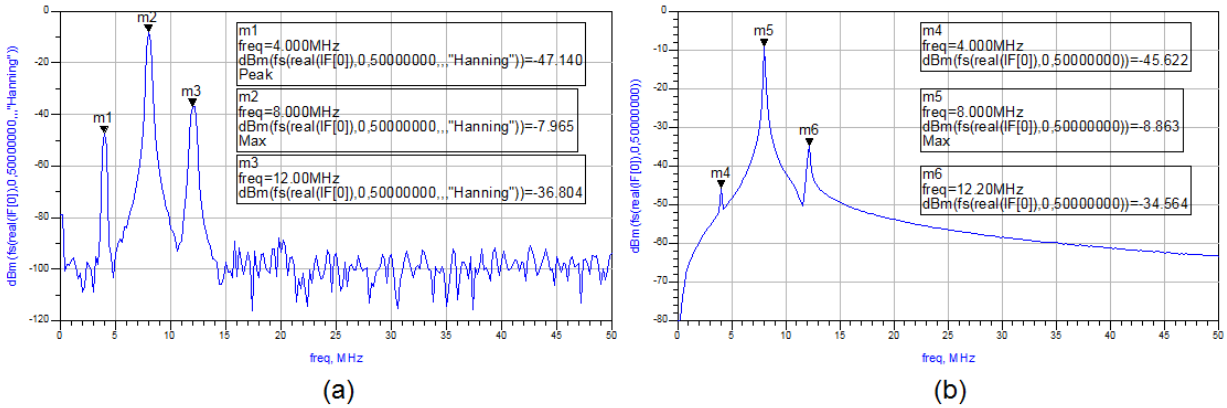

Figure 5.18: Simulation results for realistic RF-scheme B1: a) beat signal for Hanning window; b) raw beat signal.

5.5.2.4 Simulation for realistic 4.5-9 GHz chirp: RF-scheme B2

The simulation results for RF-scheme B2 with -15 dBc 2nd harmonic are shown in figure 5.19.

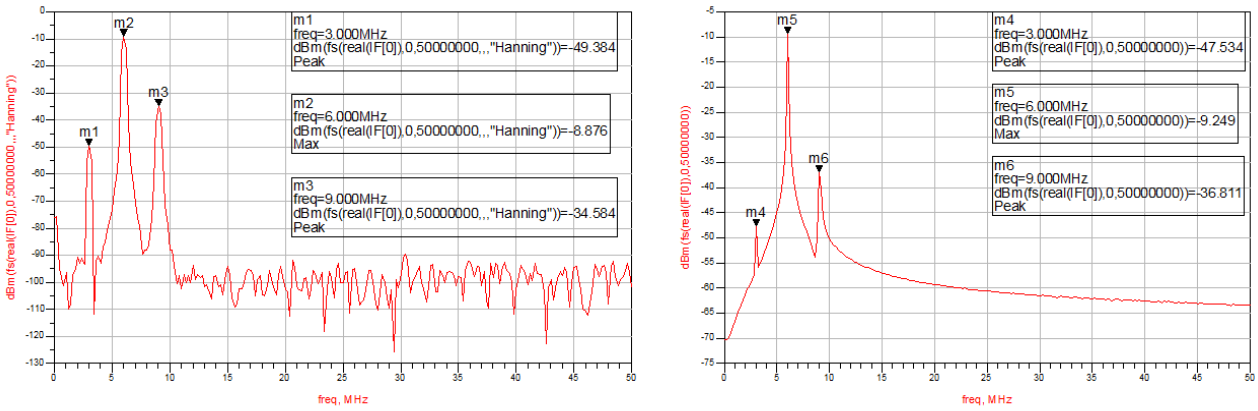

Figure 5.19: Simulation results for realistic RF-scheme B2: a) beat signal for Hanning window; b) raw beat signal.

From a quick comparison of the results, it is evident that both realistic RF-schemes B1 and B2 suffer from extra beat frequencies at relatively high level caused by the fundamental and the third harmonics of the generated chirp signal. As a matter of fact the main peak has a magnitude of -8.9 dBm, while the spurious spikes due to undesired fundamental and third harmonics have a magnitude of -34.6 and -49.4 dBm. Thus also RF-schemes B1 and B2 are not suited for our project the way they are.

An improvement of the RF-schemes is thus necessary to achieve a higher suppression of harmonics and obtain a beat signal free from their influence.

5.5.3 Simulation of improved RF-schemes with harmonics suppression

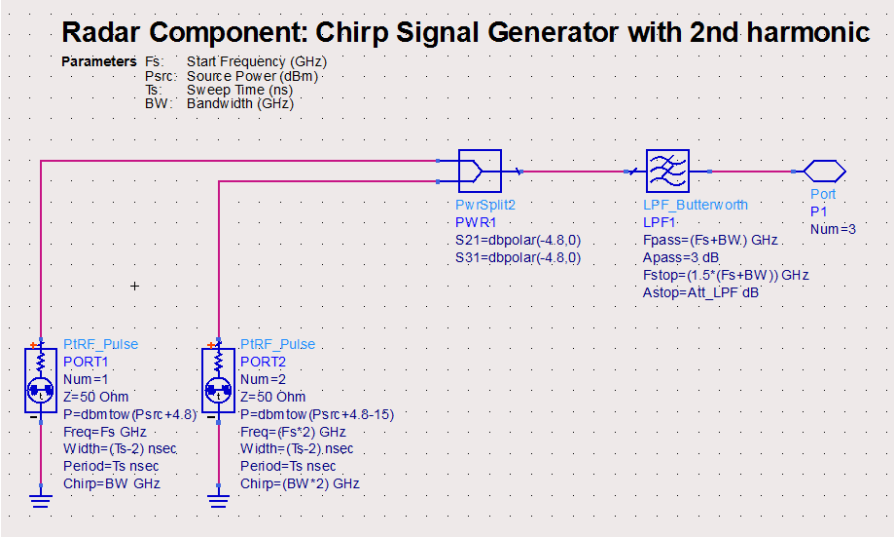

Figure 5.20: Chirp signal generator, with low-pass filter at its output to suppress harmonic.

A practical way to reduce the influence of harmonics caused by the source consists in filtering the output of the chirp generator via a low-pass filter. This method is very efficient when the filtered chirp signal bandwidth is not larger than an octave, since it would not contain in-band harmonics. This is the case when using the 4.5-9 GHz chirp signal, while the 3-9 GHz chirp signal contains also part of its second harmonic (6-9 GHz), which is more difficult to eliminate. The improved RF-schemes B1 and B2, with a low-pass filter inserted at the source output as shown in figure 5.20, will be referred to as RF-schemes C1 and C2, respectively.

The low-pass filter has been designed to suppress the out-of band harmonics, while it does not have any effect on eventual in-band harmonics. A Butterworth low-pass filter was used to for this purpose and its parameters (illustrated in figure 5.21, a) were set as follows:

- Pass-band edge frequency (F_{pass}) was set to the highest frequency of the chirp signal, computed as F_s+BW, and corresponding to 9 GHz in both RF-schemes C1 and C2;
- Attenuation at passband edges (A_{pass}) was set to 3 dB;
- Stopband edge frequency (F_{stop}) was set to 1.5 (F_s+BW), corresponding to 13.5 GHz for both RF-schemes C1 and C2;
- Attenuation at stopband edges (A_{stop}) was set to 55 dB.

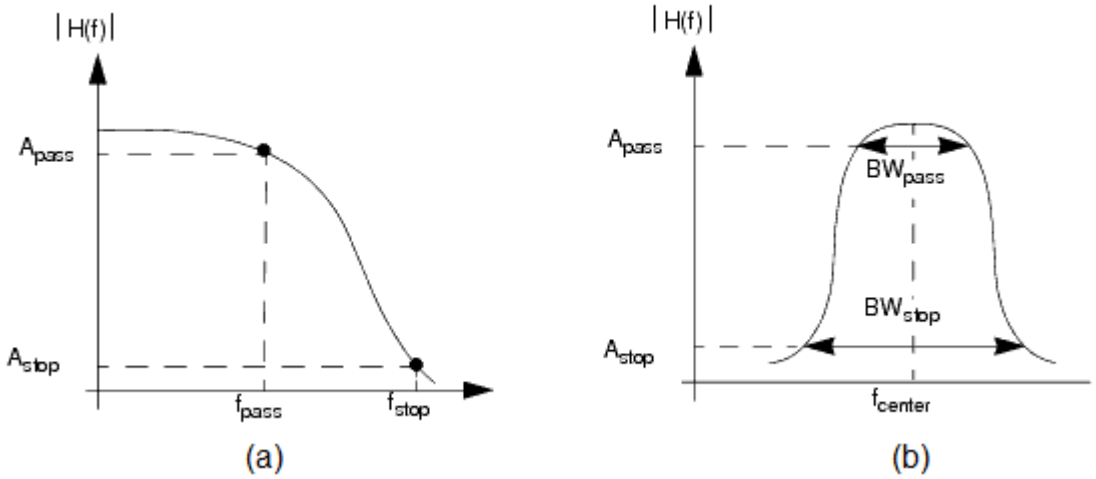

Figure 5.21: Typical transfer functions of low-pass filter (a) and band-pass filter (b).

5.5.3.1 Simulation of realistic RF-schemes C1 and C2

Figures 5.22 and 5.23 show the beat signals of RF-schemes C1 and C2, respectively. As it can be seen, low-pass filtering of the chirp signal improves the harmonics suppression of both schemes, but in a different way.

RF-scheme C1, whose main peak has a magnitude of -11.8 dBm, achieves fundamental and third harmonic suppression of about 53.5 dB and 42 dB, respectively, but the extra spikes due to harmonics are still evident and appear to be larger.

On the other side, the beat signal resulting from RF-scheme C2, whose main peak has a magnitude of -8.5 dBm, is very similar to the one obtained from the ideal case of RF-scheme B2, were the harmonics produced by the chirp generator were not simulated, and shown in figure 5.17. Fundamental and third harmonic suppression is quantified as around 68 dB and 76.5 dB respectively, and it is much higher than for RF-scheme C1. The harmonic rejection of the low-pass filter is much more effective for the RF-scheme C2, where the harmonics are entirely outside the main 9-18 GHz chirp frequency band.

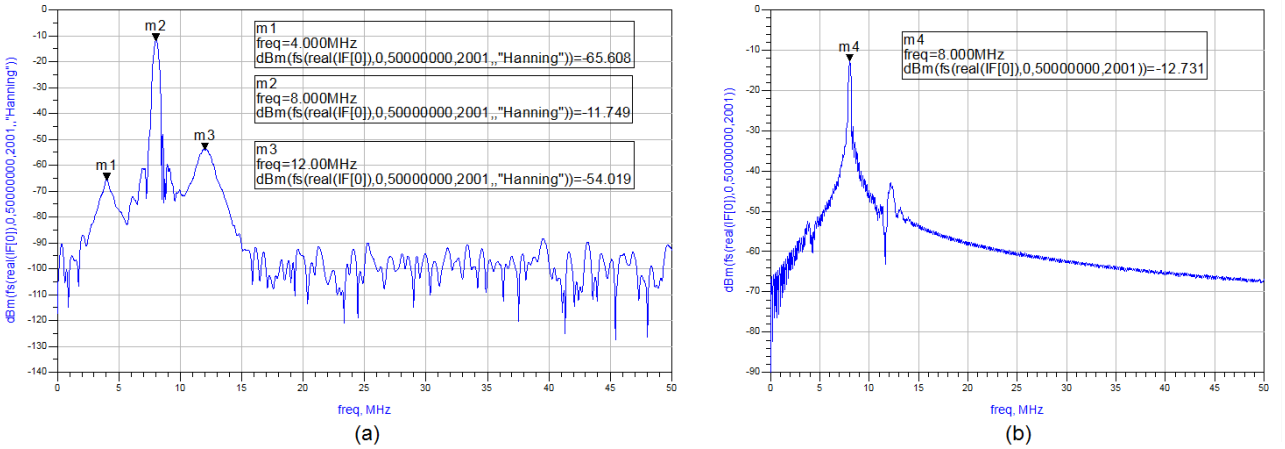

Figure 5.22: Simulation results for realistic RF-scheme C1: a) beat signal for Hanning window; b) raw beat signal.

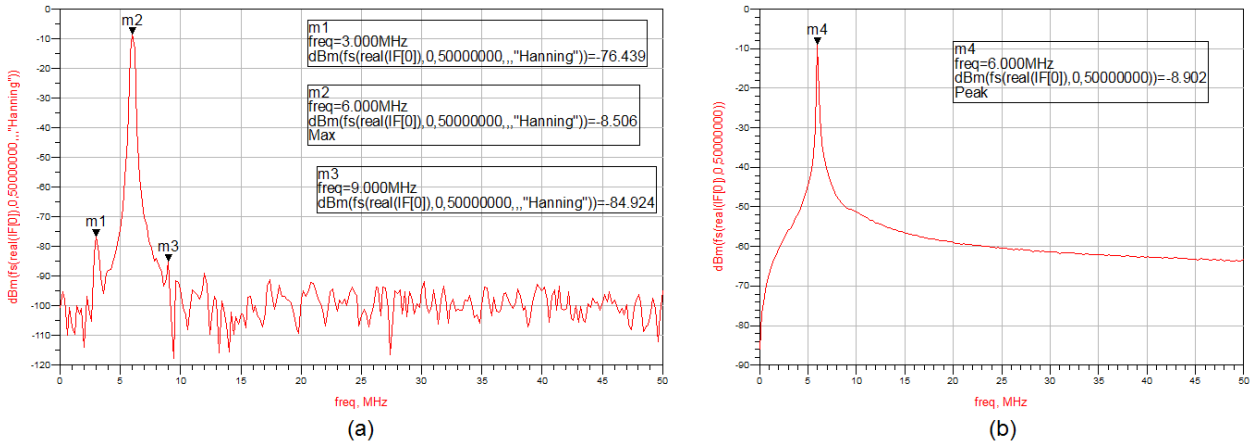

Figure 5.23: Simulation results for realistic RF-scheme C2: a) beat signal for Hanning window; b) raw beat signal.

In spite of improved situation, this harmonic suppression of RF-scheme C2 is still not enough to completely suppress the extra beat frequencies below the noise floor, since they still appear at about -68 and -76.5 dBc w.r.t. the main peak. However, it is important to remember that the results don't take the out-of band behavior of the RF-components into account. In order to show this effect, an additional RF-scheme with band-pass filters (BPFs) in front of both RF and LO ports of the mixer was simulated for both cases with multi-octave band and octave band, to which we refer to as RF-schemes D1 and D2 respectively (fig. 5.24).

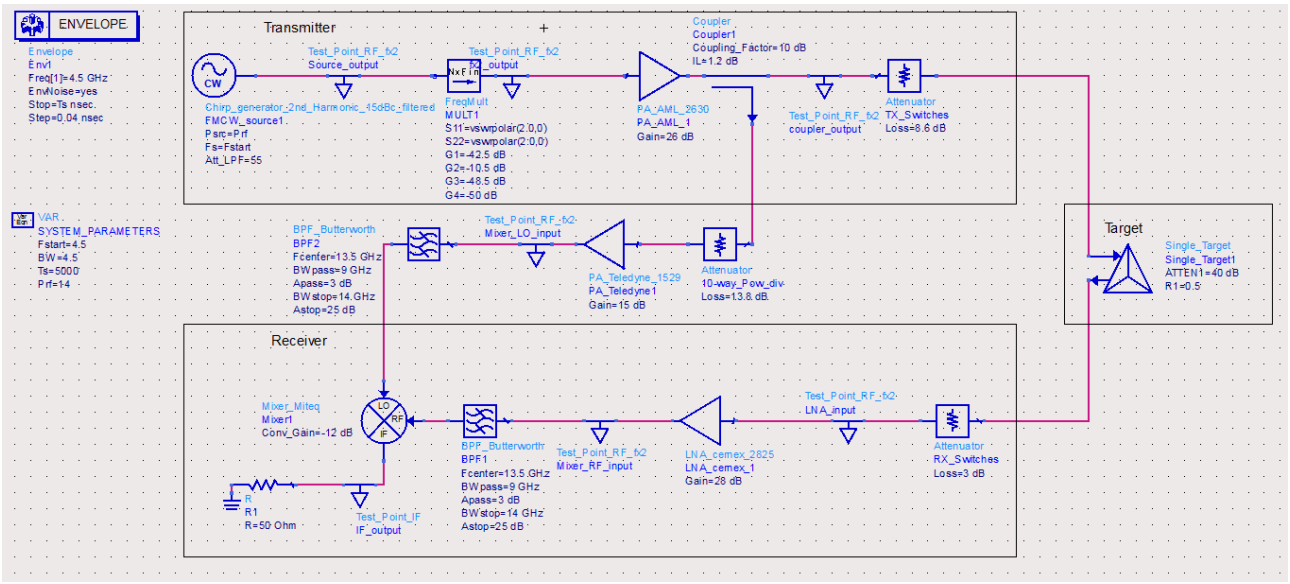

Figure 5.24: RF-scheme D2 in ADS.

5.5.3.2 Simulation of realistic RF-schemes D1 and D2

The band-pass filter for RF-scheme D1 has been set with the following parameters (see figure 5.21 (b) for reference):

- Pass-band center frequency (F_{center}) was set to the center frequency of the 6-18 GHz chirp signal, i.e. 12 GHz;
- Pass-band edge-to-edge width (BW_{pass}) was also set to the chirp signal bandwidth, 12 GHz;
- Attenuation at pass-band edges (A_{pass}) was set to 3 dB;
- Stop-band edge-to-edge width (BW_{stop}) was set to 17 GHz;
- Attenuation at stop-band edges (A_{stop}) was set to 25 dB.

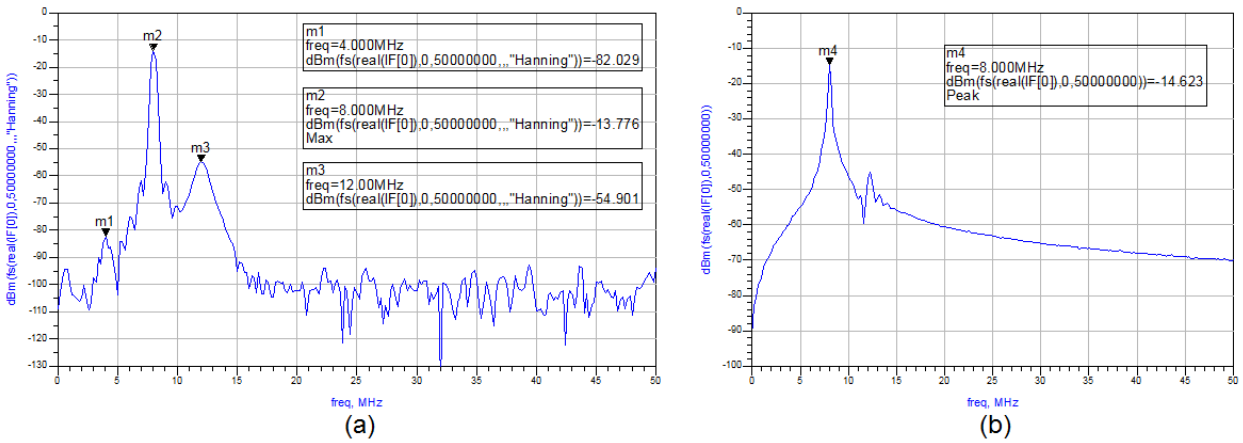

Figure 5.25: Simulation results for realistic RF-scheme D1: a) beat signal for Hanning window; b) raw beat signal.

The simulation results for RF-scheme D1, where the main peak has a magnitude of -13.8 dBm, show a better rejection of the first harmonic, decreasing its level by an additional 17 dB with respect to RF-scheme C1, while no improvement is shown in the suppression of third harmonic, which remains at a magnitude of -54.9 dBm.

RF-scheme D2 was simulated in two different cases: in the first, the BPF has the same settings used in RF-scheme D1, since the selected RF-components are specified for a 6-18 GHz bandwidth. However, the results still show a small peak (-81.5 dBm) due to fundamental harmonic, which means further harmonic suppression is required. Because of this, RF-scheme D2 was also simulated with a 9-18 GHz BPF, with the following parameters:

- Pass-band center frequency (F_{center}) was set to the center frequency of the 9-18 GHz chirp signal, i.e. 13.5 GHz;
- Pass-band edge-to-edge width (BW_{pass}) was also set to the chirp signal bandwidth, 9 GHz;
- Attenuation at pass-band edges (A_{pass}) was set to 3 dB;
- Stop-band edge-to-edge width (BW_{stop}) was set to 14 GHz;
- Attenuation at stop-band edges (A_{stop}) was set to 25 dB.

The results of simulation of RF-scheme D2 with 9-18 GHz BPF are shown in figure 5.25 (b). As it can be seen, the beat signal doesn't have any extra beat frequency in this case, and the influence of harmonics has been totally suppressed.

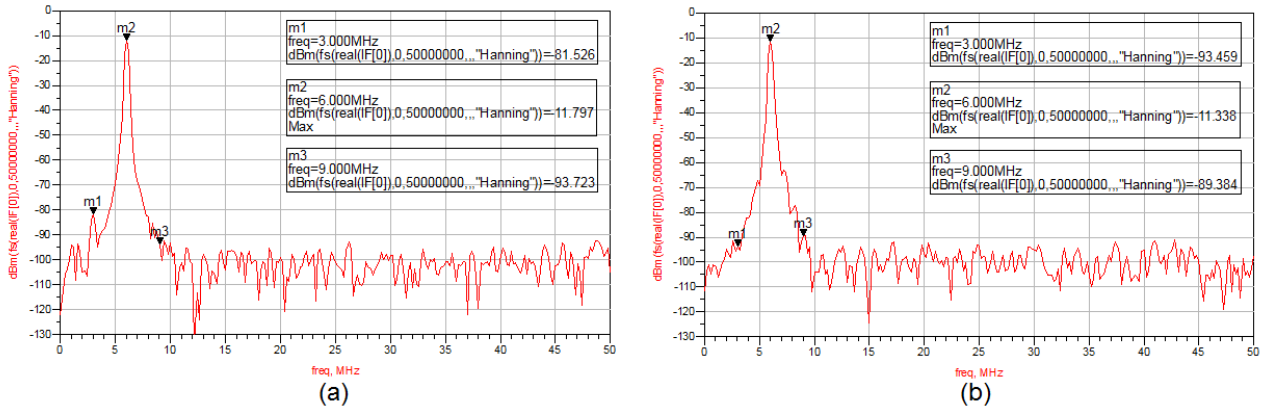

Figure 5.26: Simulation results for realistic RF-scheme D2: a) with 6-18 GHz band-pass filter; b) with 9-18 GHz band-pass filter.

5.5.3.3 Simulation of RF-scheme E1

In order to try to improve the third harmonic suppression of RF-schemes C1 and D1, an additional RF-scheme E1 was simulated. Such RF-scheme includes BPFs in front of also the PAs and the LNA, with the following parameters:

- Pass-band center frequency (F_{center}) was set to the center frequency of the 6-18 GHz chirp signal, i.e. 12 GHz;
- Pass-band edge-to-edge width (BW_{pass}) was also set to the chirp signal bandwidth, 12 GHz;
- Attenuation at pass-band edges (A_{pass}) was set to 1 dB;
- Stop-band edge-to-edge width (BW_{stop}) was set to 17 GHz;
- Attenuation at stop-band edges (A_{stop}) was set to 25 dB.

However, the simulation results do not show any improvement of third harmonic suppression, which remain about 40 dB lower than the -17.1 dBm main spike, which is widened by the use of these filters. In conclusion this solution has only worsened the situation, and based on the other results, the best compromise between complexity of the RF-scheme and suppression of higher harmonics for the multi-octave band case remains the RF-scheme C1.

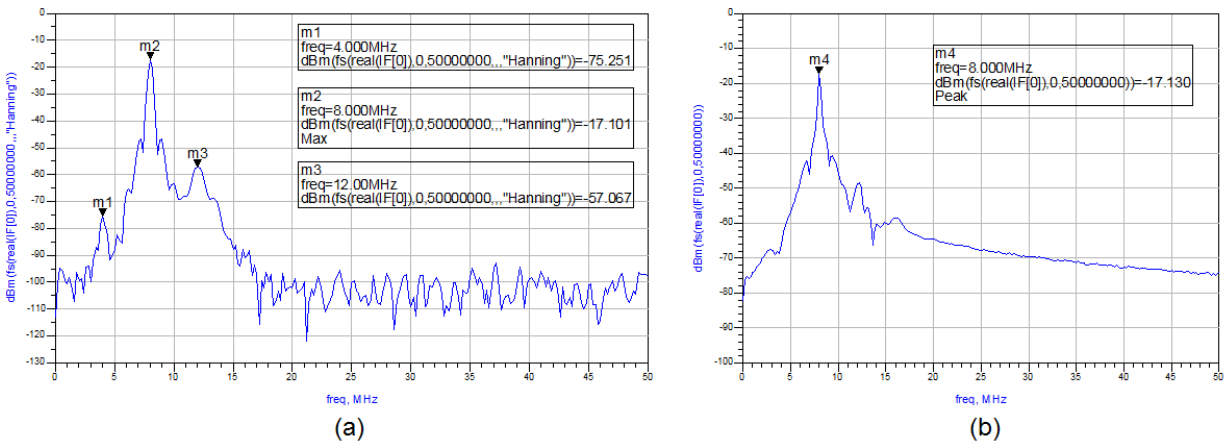

Figure 5.27: Simulation results for realistic RF-scheme E1: a) beat signal for Hanning window; b) raw beat signal.

5.5.4 Summary of harmonic suppression

To summarize, the main purpose of the simulations presented in this paragraph was to investigate the influence of harmonics generated by the YTO and the frequency doubler on the beat

signal. Beginning from the basic RF-scheme presented in chapter 3, where the desired chirp signal is directly generated by the YTO without using any frequency doubling, we simulated in total 5 different types of RF-scheme, and for each type of RF-scheme two different implementations were simulated: implementation 1 uses a 6-18 GHz chirp signal, , while the implementation 2 is characterized by a 9-18 GHz chirp signal.

Simulations of basic RF-scheme A1 and A2, where the chirp signal is directly generated by the YTO without the use of a frequency doubler, showed that the -15 dBc 2^{nd} harmonic of the chirp signal generated by the selected YTO has a consistent influence on the beat signal, generating extra beat signals at a relatively high level (-37 dB w.r.t main peak) which can be detected as additional targets. Further investigations showed that if the 2^{nd} harmonic level of the YTO was not higher than -40 dBc, the extra beat signals would have been below the -102.5 dBm noise floor computed in ADS.

Simulations of RF-schemes B1 and B2, in which the chirp signal is generated by a series of a YTO and a frequency doubler, and is thus represented by the 2^{nd} harmonic signal generated by the latter component, showed that the lever of harmonics generated by the latter alone is much lower than the ones generated by the YTO, but combined with the 2^{nd} harmonic generated by the YTO it causes generation of two strong additional beat signals (at about -40 dB and -31 dB level w.r.t main peak), the first corresponding to the fundamental harmonic generated by the YTO and reduced by the frequency doubler, and the second representing the third harmonic signal generated by the frequency doubler.

In RF-schemes C1 and C2, in order to decrease the level of these additional signals, we tried to reduce the level of the 2^{nd} harmonics generated by the YTO, by adding a low pass filter at its output. For RF-scheme C1, where a 6-18 GHz low pass filter was used, the harmonics suppression was improved but the two additional beat signals, at a level of -54 dB and -42 dB respectively w.r.t main peak, were still evident. The reason for this is to be found in the fact that the chirp signal generated by the YTO (3-9 GHz) also contains part of its second harmonics, and their rejection with the use of a LPF is only partial. On the other hand, in RF-scheme C2, rejection of 2^{nd} harmonic of the YTO is more effective, since the 4.5-9 GHz chirp signal coming out of the YTO does not contain in-band harmonics, which are then totally suppressed by the downstream LPF. As a consequence, the two additional spikes in the beat signal have a much lower level than they had in RF-scheme C1, with a -68 dB and -76.5 dB level w.r.t higher peak.

RF-schemes D1 and D2 contain two additional band-pass filters (with pass bands corresponding to the chirp bandwidth) in front of both the LO and the RF ports of the mixer, with the purpose to suppress the harmonics generated by the frequency doubler. However, the simulation results are

quite different for the two implementations. While RF-scheme D2 finally achieves a total harmonic rejection, RF-scheme D1 doesn't show any improvement in rejecting the third harmonic. The reason for this can be explained by the fact that a big part of the 3rd harmonic signal (9-27 GHz) is contained within the 6-18 GHz 2nd harmonic, and no filters would be useful to suppress it. As a matter of fact, even if we insert additional BPF filters in front of the power amplifiers and the LNA, as we did in RF-scheme E1, the 3rd harmonic suppression is not improved.

In conclusion, the investigation on harmonic influence shows that harmonic rejection is more easily achieved when the chirp signal has a bandwidth not larger than an octave, and doesn't have any in-band harmonics, making it possible to suppress the harmonics below the noise floor, as shown by simulation results of RF-scheme D2.

On the other hand, for the 6-18 GHz multi-octave band chirp signal, the best results are achieved by RF-schemes C1 and D1, with the first one preferred as the best compromise between complexity of the electronics (since it only requires a LPF after the YTO) and minimal harmonic suppression of 42 dB.

5.6 Detectability analysis of weaker targets

After selection of the final RF-schemes, we can now investigate the detectability of typical small targets like a handgun or a knife at the maximum operational distance. In Section 4.4 we performed a detectability analysis at the receiver input for a small handgun and a knife, based on the RCS measurements we performed in DUCAT and illustrated in Appendix A. According to our mathematical analysis, both targets have an average SNR slightly above 10 dB at the maximum operational distance of 2 m from the radar, which should be enough for detection.

The average propagation loss of these targets was computed as -74.8 dB for the gun and -74.6 dB for the knife, when they are placed at 2 m distance from the radar. From figure 5.27, where ADS simulations of RF-schemes C1 and D2 with target set to 2 m distance and 75 dB attenuation are illustrated, we can see how even in these cases the target reflections are widely above the noise floor, with a magnitude of about -46 dBm both, and the weaker targets alone can thus be detected.

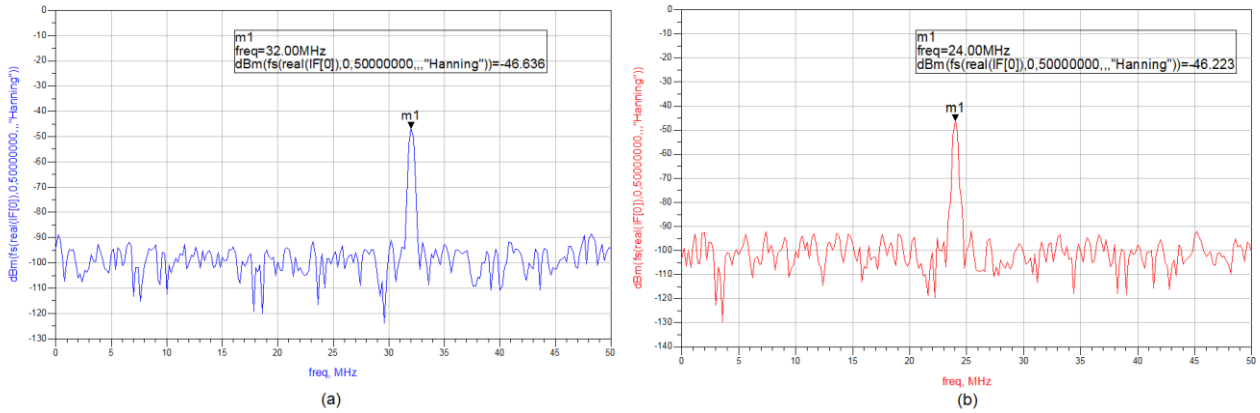

Figure 5.28: Simulation results for a weak target (75 dB attenuation) at 2 m distance: a) RF-scheme C1; b) RF-scheme D2.

However, in a realistic application scenario, the weapons are concealed on a person's body, and the separation distance between the weapons and the human body in the down-range dimension will be quite short, let's say not higher than 20 cm, with the weapons typically closer to the radar than the human body.

Computation of propagation loss due to reflections from a human body and typical weapons, when they are at the same distance from the radar (2 m in fig. 5.29), shows that human body reflections are on average about 4 dB higher than weapons reflections, with a maximum difference of about 20 dB (not considering the evident dips in the propagation loss due to reflections from human body, which are due to near-field measurements of its reflectivity).

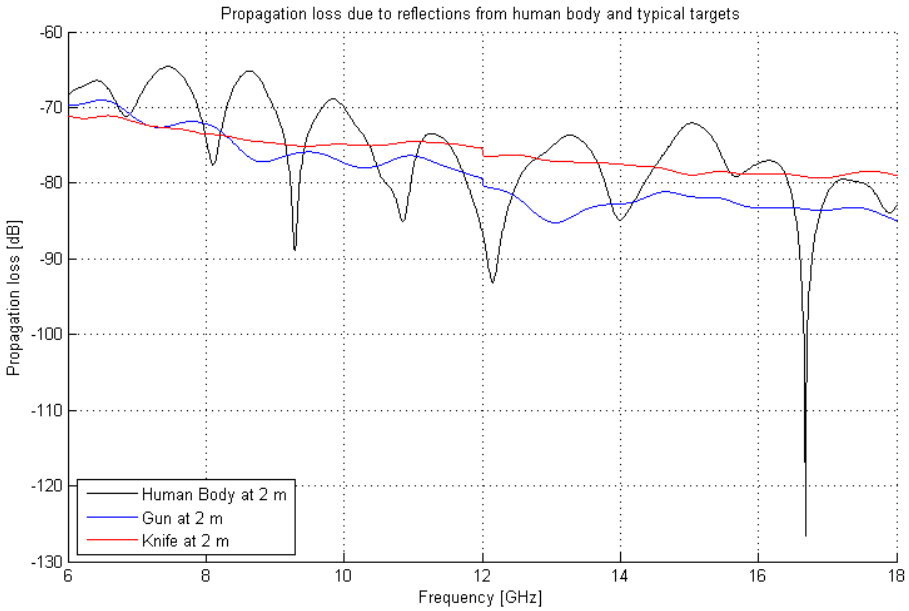

Figure 5.29: Estimated propagation loss due to reflections from a human body, a handgun and a knife, placed at 2 m distance from the radar.

In the case of RF-scheme C1, applying amplitude selection by rejecting everything below -42 dB with respect to the stronger peak (which is likely to be due to reflections from human body), will ensure suppression of harmonics while keeping the reflections from smaller targets concealed on the human body (which will be at most 20 dB lower than human body reflection). Thus, detection of weapons concealed on the human body can be achieved even at the maximum operational distance.

On the other hand, RF-scheme D2 requires a much lower amplitude threshold, set to -90 dBm to avoid contamination from oscillations of the noise floor. With such a low threshold, the detection of weak targets at maximum operational distance is ensured all the more so.

5.7 Down-Range resolution of RF-schemes C1 and D2

An additional series of simulations was performed in order to verify the down-range resolution of the selected RF-schemes C1 and D2. For our purposes, it is important to be able to distinguish reflections from two close targets. According to discussion in section 2.2, down-range resolution of the radar is computed as:

$$\delta_{\mathrm{dr}} = \frac{\mathrm{c}}{2\mathrm{B}} \tag{5.5}$$

which gives a down-range resolution of 1.25 cm for the multi-octave band scheme, and 1.67 cm for the octave band scheme. In practice, we should be able to distinguish reflections from two targets separated by such distances, which should appear as two distinguishable spikes at beat signal level.

However, simulation of RF-scheme C1 with two targets separated by 1.25 cm only show one spike, which means that the two targets are not distinguishable, as shown in fig. 5.30 (a). Further simulations shows how the RF-scheme C1 is able to distinguish the two targets when their minimal separation is 2 cm (fig. 5.31). For the sake of thoroughness, simulations for other target separations were performed, but the results were quite contradictory. As a matter of fact, the simulation results show only one spike when the target separation is increased to 2.5 cm (fig. 5.30 (b)) and again two spikes when it is set to 3 cm (fig. 5.32). Then, for target separations larger than 3 cm, the two reflections are always distinguishable (fig. 5.33).

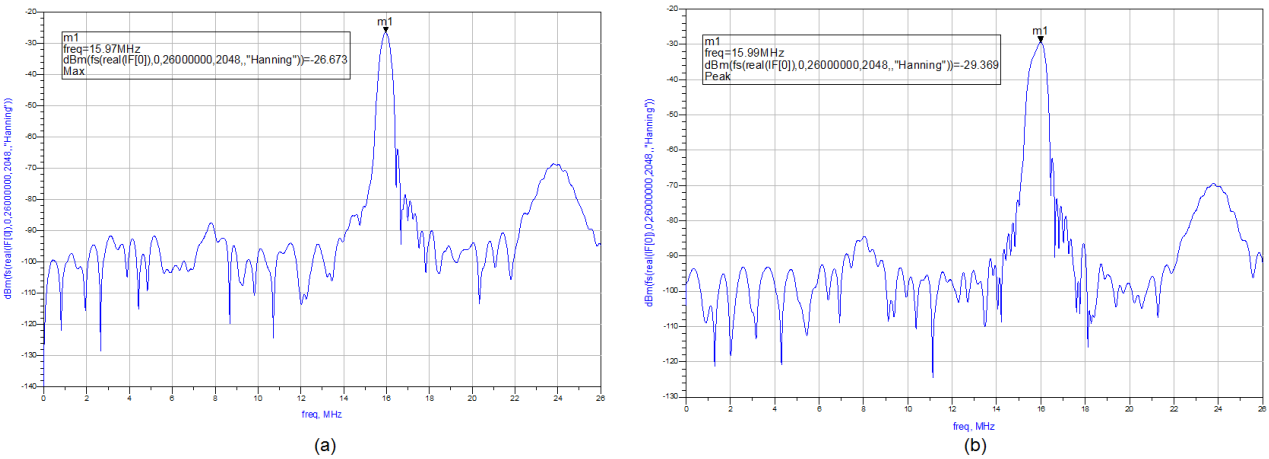

Figure 5.30: Simulation results for RF-scheme C1 with two targets: a) target separation 1.25 cm; b) target separation 2.5 cm.

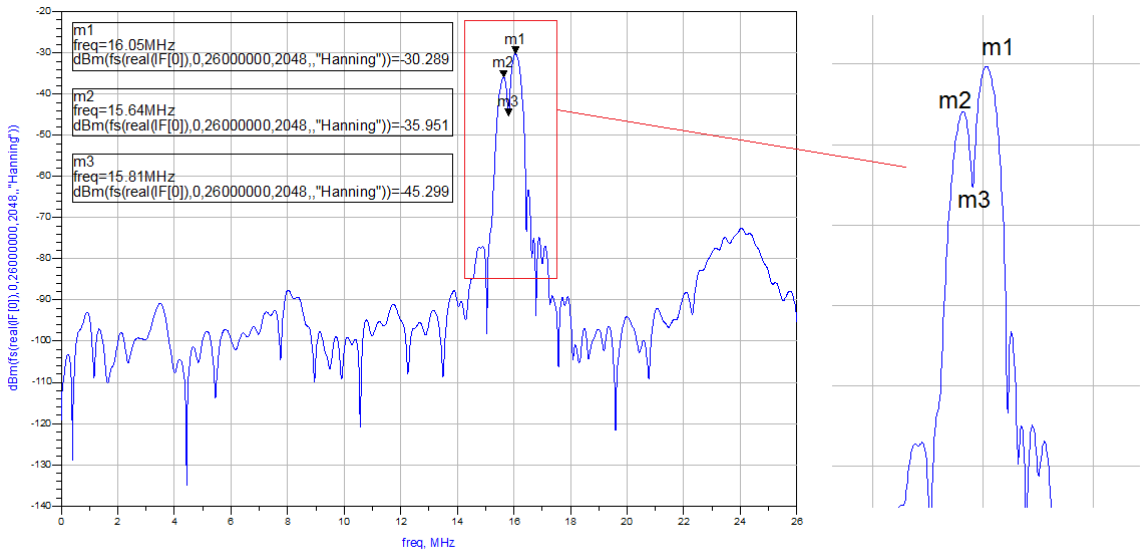

Figure 5.31: Simulation results for RF-scheme C1 with two targets separated by 2 cm.

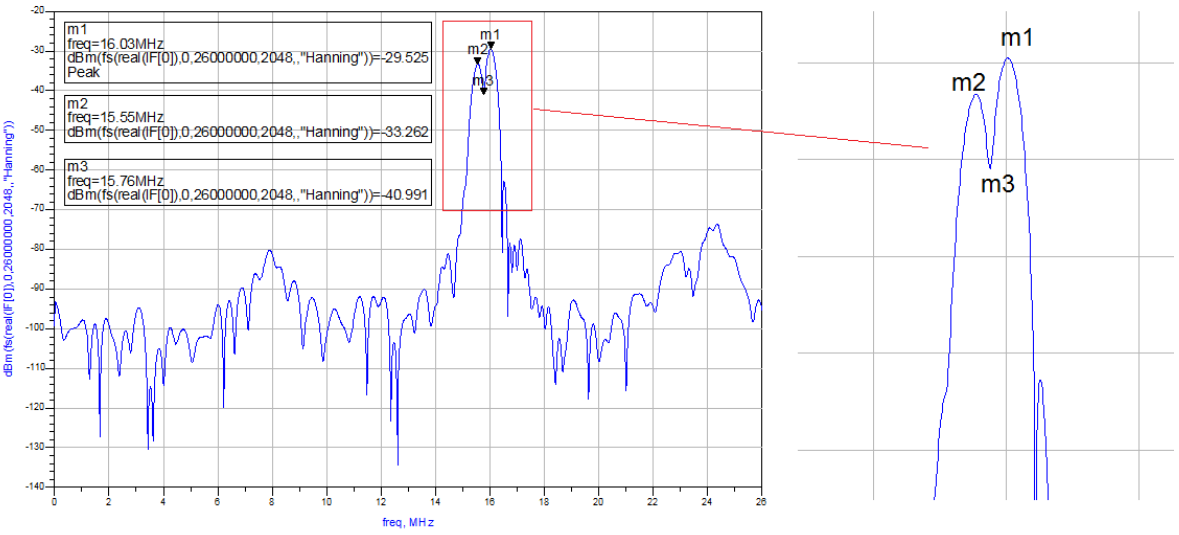

Figure 5.32: Simulation results for RF-scheme C1 with two targets separated by 3 cm.

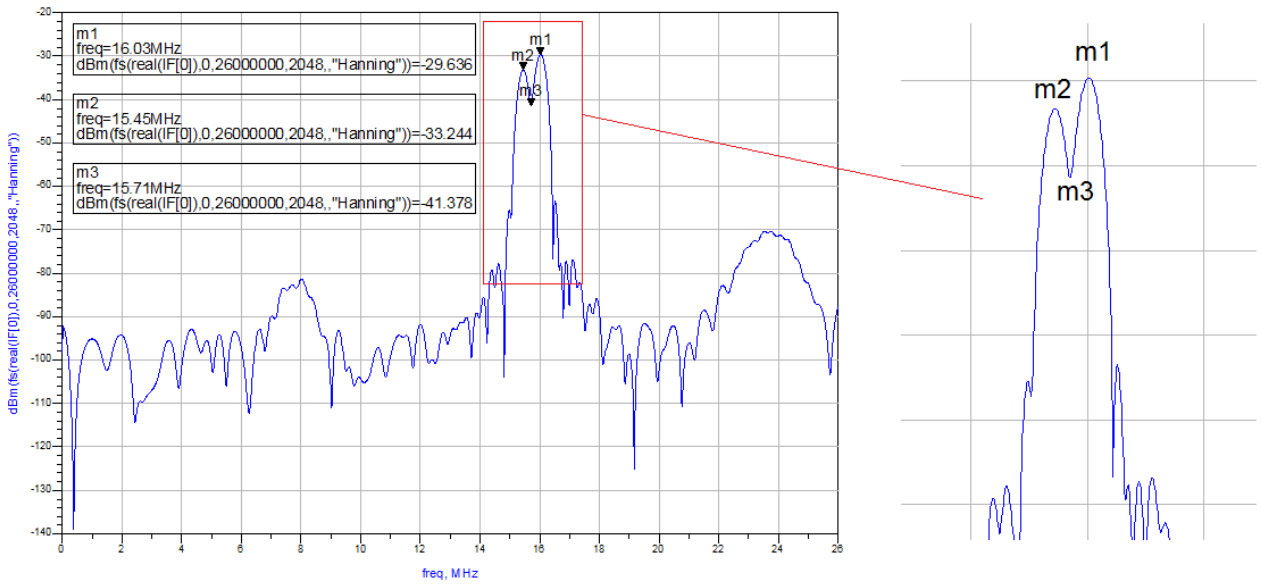

Figure 5.33: Simulation results for RF-scheme C1 with two targets separated by 3.5 cm.

Similar results were obtained from simulation of RF-scheme D2. With 1.67 cm target separation, corresponding to the down-range resolution computed with (5.5), the simulation results show two distinguishable spikes (fig. 5.34). However, simulations of the same RF-scheme with larger target separations also show contradictory results: if we increase the target separation to 2 cm, the two targets become indistinguishable (fig. 5.35), and only when their separation is increased to 3.75 cm we can again see two distinguishable spikes (fig. 5.36). Then, for target separations larger than 3.75 cm, the two reflections are always distinguishable.

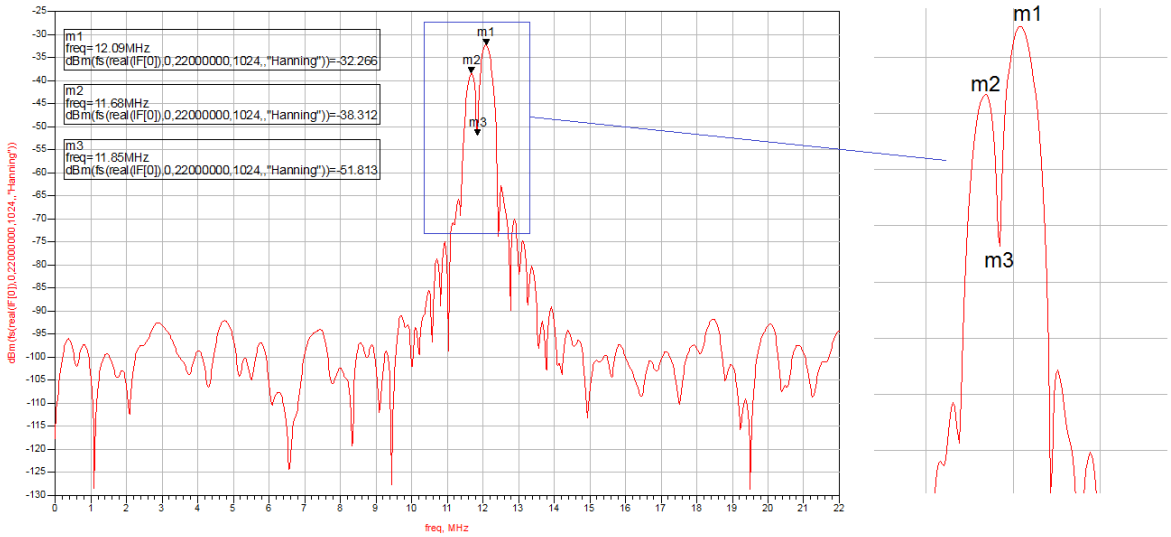

Figure 5.34: Simulation results for RF-scheme D2 with two targets separated by 1.66 cm.

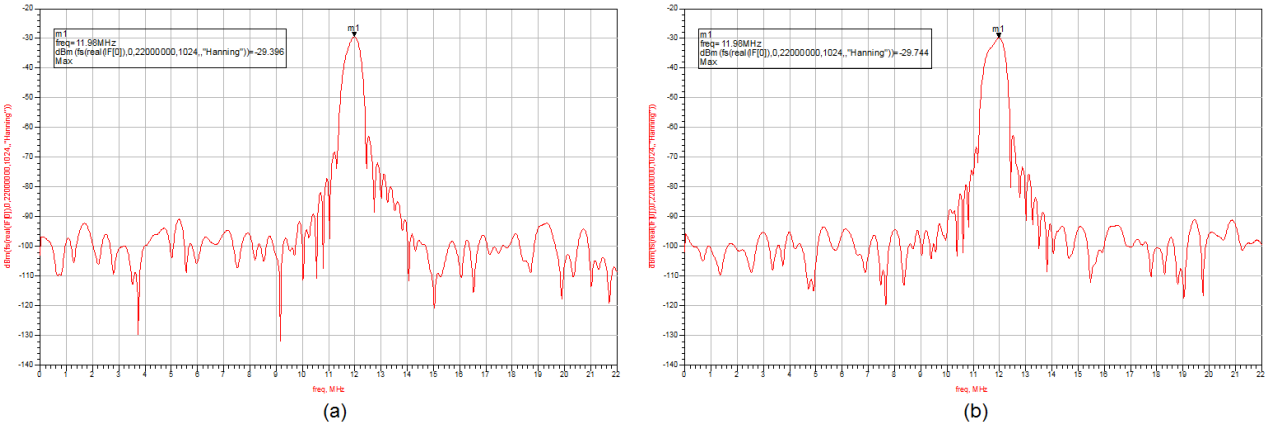

Figure 5.35: Simulation results for RF-scheme D2 with two targets: a) target separation 2 cm; b) target separation 3.33 cm.

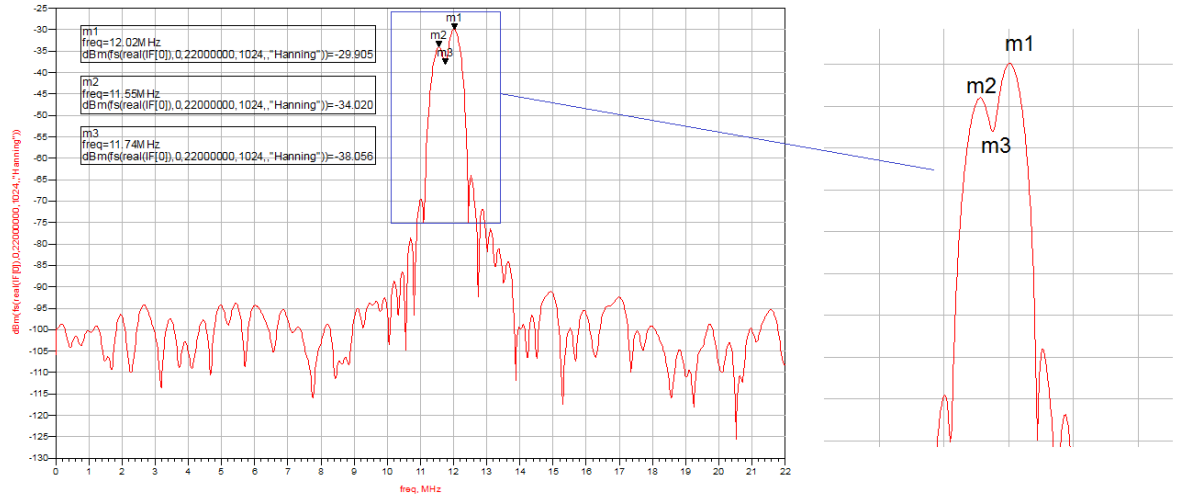

Figure 5.36: Simulation results for RF-scheme D2 with two targets separated by 3.75 cm.

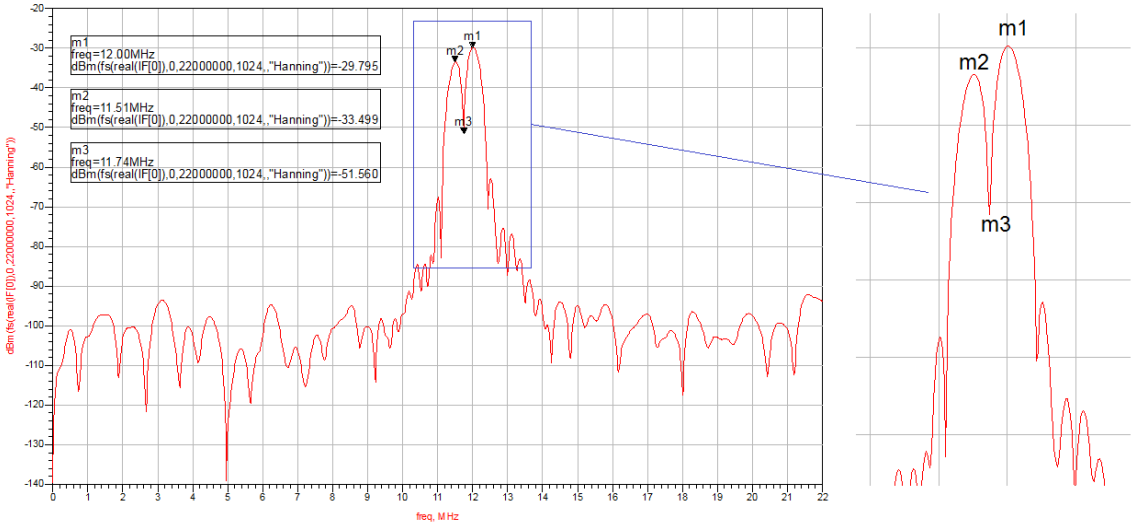

Figure 5.37: Simulation results for RF-scheme D2 with two targets separated by 4 cm.

Even if we increase the number of points for the FFT, quadrupling their number, the results illustrated above remain the same for both RF-schemes.

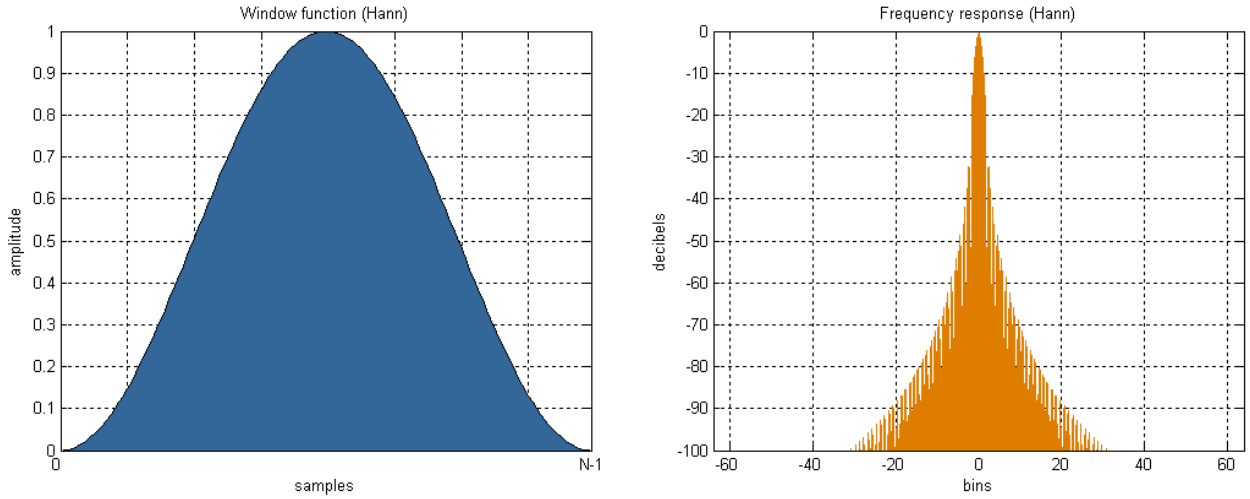

Figure 5.38: Hanning window in time domain (left) and frequency domain (right).

These contradictory results probably originate from the use of a windowing function, which in this case is the Hanning window. As a matter of fact, the Hanning window is used to partially suppress the sidelobes present in the raw signal (for Hanning window, maximum sidelobe level is 32 dB lower than main peak), but at the same time it causes a widening of the main peak, for a decrease of frequency resolution of about 44 % at -3 dB bandwidth, and of around 100% and -6 dB bandwidth [30]. In addition, when we have two close reflections, the sidelobes of the stronger one can overlap with the other reflection, either increasing or decreasing the latter. Use of different

smoothing windows didn't show any improvement, and the results obtained for the down-range resolution were the same.

In conclusion, the ADS simulations show a down-range resolution of 3 cm for the RF-scheme C1 and of 3.75 cm for the RF-scheme D2.

5.8 Amplitude characteristic of the receiver.

In order to investigate the minimum detectable signal and the saturation point of the receiver, and determine its amplitude characteristic, several simulations were performed with different target attenuations. The resulting amplitude characteristic of the receiver for both schemes C1 and D2 is shown in figure 5.39, where also the maximum and minimum estimated signals for typical targets are indicated. The amplitude thresholds used in the two schemes are not considered here, but this doesn't change the fact that both the maximum and minimum estimated signals occur within the linear portion of the amplitude characteristic of the receiver, ranging from a max of about +3 dBm to a min of about -90 dBm, which means that the dynamic range of the receiver is wide enough to detect both strong and weak targets.

However, the dynamic range obtained through simulations appears to be shorter than the value computed in section 4.3. This is due to the peak-to-peak variations of the noise floor, which causes the noise power to oscillate within ± 15 dB w.r.t. the -102.5 dBm noise floor, and thus decreases the dynamic range by about 15 dB.

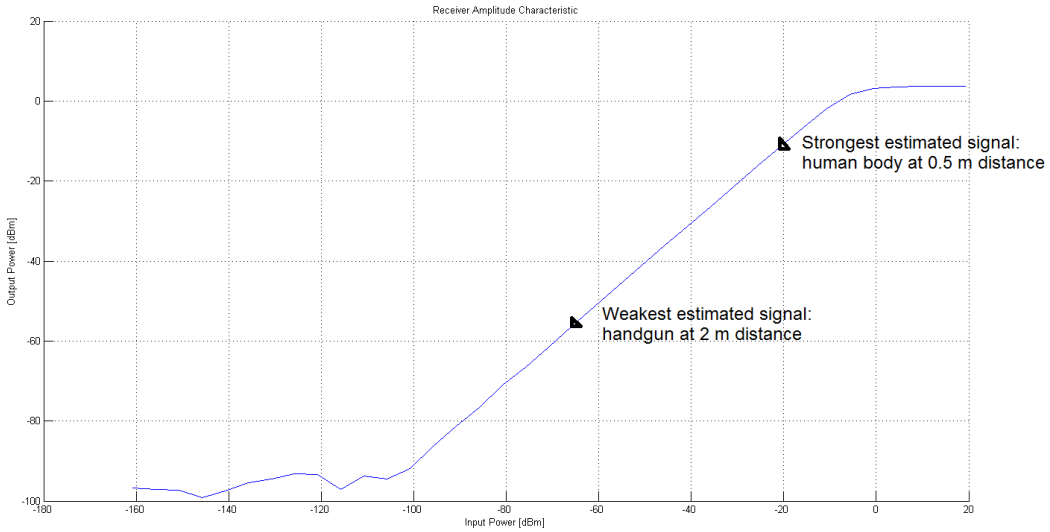

Figure 5.39: Amplitude characteristic of the radar receiver; the stronger and the weaker signal estimated from human body and typical targets, respectively, are also indicated to be within the linear part of the receiver's amplitude characteristics. Input power is measured at RX switch input, output power refers to main peak of beat signal at mixer IF output.

5.9 Conclusions

In this chapter, the procedure followed to simulate the RF-scheme in ADS was presented, along with simulation objectives and results for different versions and implementations of the RF-scheme and different scenarios.

Two main versions of the RF-scheme were discussed and simulated: version 1, which uses a multi-octave band 6-18 GHz chirp signal, and version 2, where the chirp signal occupies the 9-18 GHz octave band for a 66.7 % fractional bandwidth.

The first important result obtained by simulations of the RF-scheme in ADS regards the investigation on the influence of harmonics generated by the YTO and the frequency doubler at beat signal stage. The basic RF-scheme selected for our design, with a cascade of a YTO and a frequency doubler for generating the required chirp signal (RF-schemes B1 and B2), produces a high level of harmonics, generating extra beat signals which can be erroneously interpreted as additional targets, and this makes it unsuitable for this project. Further investigation showed that the insertion of a low-pass filter after the YTO to suppress its second harmonics (RF-schemes C1 and C2) shows better results, achieving a higher harmonic rejection of 42 dB for RF-scheme C1 and 68 dB for RF-scheme C2. This substantial difference in the harmonics suppression is explained by the fact that version 1 uses a multi-octave band chirp signal (6-18 GHz), whose second harmonics partially overlap with the fundamental signal band and can't be completely suppressed by low-pass filtering the frequency content above 18 GHz. On the other hand, this approach is more effective in RF-scheme C2, since the harmonics of the 9-18 GHz chirp signal are not overlapped with the fundamental signal, and consequently they can be completely rejected by the low-pass filter.

Additional simulations of more complex RF-schemes (D1 and E1), with insertion of 6-18 GHz band-pass filters in front of the power amplifiers, LNA and mixer, were also performed, but the 42 dB harmonic suppression achieved with RF-Scheme C1 was not improved. As a consequence, RF-scheme C1 was selected as the best solution to suppress the harmonics of the multi-octave band chirp signal.

As for the octave band version of the RF-scheme, simulations of RF-scheme D2, with an additional 9-18 GHz BPF in front of both the RF and LO ports of the mixer, showed a complete suppression of harmonics below the noise floor, achieving a much better spurious free dynamic range than its multi-octave band counterpart. RF-scheme D2 was thus selected as the best solution for harmonics suppression when using the octave band chirp signal.

Additional simulations were performed for the two selected RF-schemes to evaluate the detectability of weaker targets on the background of a strong reflection (which is likely to be represented by the reflections from the human body). In principle, in order to avoid erroneous interpretation of higher harmonics as an additional target, RF-scheme C1 requires an amplitude threshold of -42 dB with respect to the stronger received signal. This means that its detection ability is limited to targets whose reflected signal power does not differ more than 42 dB from the stronger reflection. Luckily, investigation on the power reflected from typical targets in realistic application scenarios show that the difference between the strongest and the weakest signal is around 20 dB, and the selected RF-scheme C1 is consequently suitable for their correct detection even at the maximum operational distance of 2 m.

All the more so, RF-scheme D2 is also capable to detect weaker targets at the maximum operational distance on the background of a strong reflection, since it has a twice wider dynamic range than RF-scheme C1.

For the sake of thoroughness, we also investigated the down-range resolution achieved by the two schemes via ADS simulations. Results showed in both cases a worse resolution than the ones computed via analytical formula (5.5), probably due to the use of Hanning window which slightly reduces the frequency resolution and whose sidelobes can overlap with a target reflection when two targets are very close. RF-scheme C1 achieves a down-range resolution of 3 cm, while for RF-scheme D2, the ADS simulations showed a minimum down-range resolution of 3.75 cm.

To summarize, ADS simulations have shown satisfactory results and the two selected solutions, namely RF-schemes C1 and D2, are both suitable for our project. In general, RF-scheme D2 achieves a better harmonic suppression than RF-scheme C1, but this doesn't make it better for our project, since both solutions have shown the capability to detect the weakest estimated targets at maximum operational distance with the background of human body reflections. In addition, RF-scheme C1 uses a larger bandwidth and obtains a finer down-range resolution, finally tipping the balance in favor of this latter solution.

In conclusion, RF-scheme C1 is the preferred solution because of its better bandwidth and down-range resolution.

Chapter 6: Conclusions and recommendations

6.1 Conclusions

In this thesis project, an UWB radar front-end for security applications has been designed and simulated. The objectives of this thesis work were to investigate the feasibility of a radar sensor achieving high resolution, fast acquisition speed and high-performance in general, while keeping cost and complexity to the minimum.

After a survey of state-of-the-art Imaging systems for security application, and a fundamental study of the ways to obtain particular performance requirements, we came to the conclusion that a microwave UWB MIMO array-based radar front-end would have been the best solution to the problem. FMCW homodyne architecture was selected for its low complexity in the electronics and the simplicity in the implementation. An antenna system based on the MIMO technique was deemed necessary to reduce the number of elements in the array, with the purpose to reduce its cost both in economical and computational terms, without a net deterioration of its performance. Use of commercially available components was considered in order to keep the costs low. Definitive selection of frequency band was also based on the availability of RF-components, and was selected as 6-18 GHz. Unluckily, we couldn't find any fast YTOs in the 6-18 GHz bandwidth, and in order to achieve a fast data acquisition time, we selected a combination of a fast sweep 3-9 GHz YTO and a frequency doubler to generate the desired 6-18 GHz sweep, for a data acquisition speed 25 times faster than the one we would have obtained by direct sweeping of commercially available 6-18 GHz YTOs.

The selected RF-scheme was finally simulated in ADS to examine its performance. At first, we investigated the influence of harmonics generated by the RF-electronics on the beat signal. As a matter of fact, the combination of YTO and frequency doubler selected to generate the desired 6-18 GHz chirp signal also generated spurious harmonics, which at the beat signal stage appears as extra beat-signals that could be interpreted as additional targets. Simulations in ADS confirmed that the level of these harmonics is relatively high (-26 dB w.r.t main peak at beat signal stage), making the basic RF-scheme unsuitable for our design the way it was. Further investigations on possible ways to reduce the problem showed that the best solution consists in the insertion of a DC-9 GHz low-pass filter at the YTO's output, which allows decreasing the level of such harmonics down to -42

dB w.r.t the main peak at the beat signal stage. Total suppression of harmonics was not possible due to the fact that the main 6-18 GHz chirp signal contains in-band harmonics that cannot be rejected via filtering, and the use of an amplitude threshold to reject everything 42 dB below the strongest peak was deemed necessary to avoid detection of harmonics as additional targets.

An alternative solution was represented by the use of a shorter chirp signal in the 9-18 GHz frequency band. Such signal does not contain in-band harmonics, and this makes it possible to suppress the harmonics generated by the RF-electronics via filtering. This was also confirmed via ADS simulations, which showed a total harmonic suppression with the use of a low-pass filter at YTO's output, and 9-18 GHz band-pass filter at the input of both LO and RF port of the mixer.

ADS simulations also showed that the 42 dB spurious free dynamic range of the 6-18 GHz RF-scheme is wide enough to detect the weakest targets (represented by a handgun and a knife) on the background of human body reflections even at the maximum operational distance of the radar, set to 2 m, thus validating this RF-scheme for our project. All the more so, the 9-18 GHz harmonic free solution, given its wider dynamic range, is also capable to detect the weakest targets in the background of human body reflection. Additional investigation on their ability to separate reflections from two close targets showed a 3 cm down-range resolution for the 6-18 GHz RF-scheme, and 3.75 cm for the 9-18 GHz RF-scheme.

RF-scheme	BW	Fractional BW	Harmonic suppression achieved	Acquisition time	Down-range resolution
C1	6-18 GHz	100%	-42 dB	0.17 s	3 cm
D2	9-18 GHz	66.7%	-80 dB	0.13 s	3.75 cm

Table 6.1: Comparative table of the two selected solutions.

To summarize, ADS simulations have shown satisfactory results, which are reported in table 6.1, and the two possible solutions, namely RF-schemes C1 and D2, are both suitable for our project.

However, the differences between the two RF-schemes are substantial: first of all, RF-scheme C1 has a larger bandwidth, corresponding to 100% fractional bandwidth against the 66.7% fractional bandwidth of RF-scheme D2. Considering the requirements on fractional bandwidth given in chapter 2, where a fractional bandwidth of at least 100% was required in order to reduce the number of elements in the MIMO array without loss of performance, RF-scheme C1 is to be preferred.

In general, RF-scheme D2 achieves a better harmonic suppression than RF-scheme C1, but this doesn't make it better for our project, since both solutions have shown the capability to detect the

weakest estimated targets at maximum operational distance in the background of human body reflections. In addition, RF-scheme C1 obtains a finer down-range resolution, finally tipping the balance in favor of this latter solution.

In conclusion, RF-scheme C1 is the preferred solution because of its better bandwidth and down-range resolution. This RF-scheme achieves good performance, and generally speaking, it allows achieving the objectives of this thesis.

6.2 Recommendations, remarks and future work.

The definitive RF-scheme with 6-18 GHz signal bandwidth meets the general requirements of this project, but there is still room for improvement of its performance, although this mainly depends on the availability of better RF-components.

The major improvement would be achieved with the use of a fast and direct 6-18 GHz sweep generator (instead of the combination of a 3-9 GHz YTO and frequency doubler) with a lower level of 2^{nd} harmonics. According to the simulation results, if the 2^{nd} harmonics generated by YTO were around -40 dBc, no amplitude threshold would have been required. Moreover, such solution would also exclude the use of frequency doubler and filters, thus further reducing the complexity and cost of the electronics. However, a YTO with these characteristics is not available on the market, and a quick investigation of the possibilities to have it custom-made excludes such solution in the very near future. It is likely that a proper YTO for the ideal RF-scheme will be realized within the next few years, so I guess it's just a question of time.

On the other side, the results obtained by ADS simulations didn't take into account out-of-band behavior of the selected RF-components, due to lack of data. A better characterization of the selected RF-components would certainly give more precise results.

Another possible improvement on the work presented in this thesis report would be represented by the investigation of detectability for a wider variety of targets. As a matter of fact, we performed a detectability analysis of a handgun and a ceramic knife as typical targets, but the variety of possible threats is much wider, spacing from plastic and ceramic guns and knives to different types of explosives. An investigation on the capability of the selected RF-scheme to detect also these targets would certainly be useful to further validate the usefulness of this solution.

Moreover, some assumptions were made on the MIMO array about the antenna coupling levels when estimating maximum received signal and about the ISL for the estimation of number of

antennas. Although these assumptions are realistic, a deeper study on the feasibility of such results is suggested to further validate the results obtained by this thesis project.

Last but not least, the estimation of phase noise in section 4.2 was made in the worst case scenarios, but a careful design of the path length differences and optimization of RF-cable lengths could help decrease the total phase noise and thus the total noise power at receiver output.

To conclude, the work presented in this thesis report shows the feasibility of a high resolution UWB radar sensor for concealed weapon detection working in the 6-18 GHz frequency band, with minimized acquisition time, cost and complexity.

References

[1] A.G. Yarovoy, "Ultra-Wideband Systems", Proc. of 33rd European Microwave Conference, Munich, Germany, 2003.

[2] A.G. Yarovoy, X. Zhuge, T.G. Savelyev, L.P. Ligthart, "Comparison of UWB Technologies for Human Being Detection with Radar", Proc. of 4th EuRAD, p.p. 295-298, 2007.

[3] T.G. Savelyev, X. Zhuge, A.G. Yarovoy, L.P. Ligthart, B. Levitas, "Comparison of UWB SAR and MIMO based short-range imaging radars", in Proc. EuRAD 2009, Rome, October 2009, 109-112.

[4] X. Zhuge, T.G. Savelyev, A.G. Yarovoy, L.P. Ligthart, J. Matuzas, B. Levitas, "Human Body Imaging by Microwave UWB Radar", in Proc. EuRAD 2008, Amsterdam, October 2008, 148-151.

[5] X. Zhuge, "Short-range Ultra-Wideband Imaging with Multiple-Input Multiple-Output Arrays", PHD Thesis, TU Delft, dec. 2010.

[6] T.G. Savelyev, X. Zhuge, B. Yang, P. Aubry, A.G. Yarovoy, L.P. Ligthart, B. Levitas, "Comparison of 10-18 GHz MIMO-based short-range imaging radars", in International Journal of Microwave and Wireless Technologies, 2010, 2(3-4), 369-377.

[7] Zhuge, X. and Yarovoy, A.G., "Near-field ultra-wideband imaging with two-dimensional sparse MIMO array", Proceedings of the 4th European Conference on Antennas and Propagation (EuCAP), 2010, pp. 1-4.

[8] Zhuge, X. and Yarovoy, A.G., "MIMO-SAR based UWB imaging for concealed weapon detection", Proceedings of the 8th European Conference on Synthetic Aperture Radar (EUSAR), 2010, pp. 194-197.

[9] B. Yang, A. Yarovoy, P. Aubry, and X. Zhuge, "Experimental Verification of 2D UWB MIMO Antenna Array for Near-field Imaging Radar", Proc. of 39th European Microwave Conference, 2009, Rome, Italy.

[10] T.G. Savelyev, X. Zhuge, A.G. Yarovoy, "FMCW RF-Board Design and Analysis", Scientific Report on Project "PROBANT", No. IRCTR – S – 022 – 07.

[11] X. Zhuge, A.G. Yarovoy, "Sparse multiple-input multiple-output arrays for high-resolution near field ultra-wideband imaging", IET Microwaves, Antennas & Propagation, 2011, Vol. 5, Iss.13, pp. 1552-1562.

[12] X. Zhuge, A.G. Yarovoy, "A Sparse Aperture MIMO-SAR-Based UWB Imaging System for Concealed Weapon Detection", IEEE Transactions on Geoscience and Remote Sensing, Vol.49, No.1, January 2011

[13] A.G. Yarovoy, "Ultra-Wideband Radars for High-Resolution Imaging and Target Classification", Proc. of 4th European Radar Conference, Munich, Germany, Oct. 2007.

[14] A. Martinez-Vazquez, J. Fortuny-Guasch, "UWB MIMO Radar Arrays for Small Area Surveillance Applications", Proc. of 2nd EuCAP, 2007.

[15] G. R. Lockwood and F. S. Foster, "Optimization of Sparse Two-Dimensional Transducer Arrays Using an Effective Aperture Approach", Proc. Ultrasonics Symposium, p.p. 1497-1501, 1994.

[16] B.J. Donnet, I.D. Longstaff, "MIMO radar, techniques and opportunities", in Proc. of the 3rd European Radar Conference, Manchester, England, September 2006.

[17] A. Huizing, "FMCW Radar", presentation given during European Microwave Week, Rome, 28th Sept. – 2nd Oct. 2009.

[18] D.M. Sheen, D.L. McMakin, and T.E. Hall, "Three-dimensional millimeter-wave imaging for concealed weapon detection," IEEE Trans. Microwave Theory Tech. 49, 1581–1592 (2001).

[19] D.M. Sheen, D.L. McMakin, and T.E. Hall, "Near-field three-dimensional radar imaging techniques and applications",

[20] D.M. Sheen, D.L. McMakin, H.D. Collins, T.E. Hall, and R.H. Severtsen, "Concealed explosive detection on personnel using a wideband holographic millimeter-wave imaging system", Proc. SPIE Aerosp./Defense Sens. Contr., vol. 2755, pp. 503 - 513, 1996.

[21] D. M. Sheen, D. L. McMakin, W. M. Lechelt, and J.W. Griffin, "Circularly polarized millimeter-wave imaging for personnel screening," Proc. SPIE 5789, pp. 117–126 (2005).

[22] D.L. McMakin, D.M. Sheen, J.W. Griffin, N.B. Valentine, W.M. Lechelt, "Personnel and Mail Screening with Millimeter Waves", Proc. SPIE 5778, pp. 160–168 (2005).

[23] R.W. McMillan, N.C. Currie, D.D. Ferris, Jr., M.C. Wicks, "Concealed Weapon Detection using Microwave and Millimiter-wave sensors", in Proc. Microw. Millimeter Wave Technol. (ICMMT'98), 1998, pp. 1–4.

[24] Guan Fu-hong, Yang Ming-hui, and Xu Jie, "A high sensibility wideband millimeter wave receiver for imaging concealed objects application", The 6th European Radar Conference, Rome, Italy, Sep.30-Oct.2, 2009: 826-829.

[25] R.Doyle, B.Lyons, A.Lettington, et al., “Stand-off detection of hidden threat objects on personnel at checkpoints and in public areas using active millimetre-wave imaging", Proc. SPIE, Vol. 5619, 90-97, 2004.

[26] L3-Communications Safeview, ProVision System, available online: http://www.sds.l-3com.com

[27] G. M. Brooker, “Understanding Millimetre Wave FMCW Radars”, International Conference on Sensors and Technology, November 2005.

[28] M.I. Skolnik, “Introduction to Radar Systems”, 2nd ed., McGraw-Hill, NY (1980).

[29] Agilent Technologies, “Circuit Envelope Simulations”, user’s guide available online at Agilent Technologies website.

[30] National Instruments, "Characteristics of Different Smoothing Windows", LabView 8.2 Help, August 2006

Appendix A: Radar Cross Section Measurements

A.1 Estimation of RCS of typical targets

The analysis of the detection capability of the RF scheme requires the knowledge of the radar cross section of some typical targets, such as a gun and a knife, in the 6-18 GHz bandwidth. The scattering of these targets was studied by frequency-domain measurements. The Telecommunication Research Center of TU Delft is provided with an anechoic chamber for antenna measurements up to 26 GHz, called DUCAT, where we had the opportunity to perform these measurements.

Initially we performed measurements of some reference targets with different antennas, in order to check how close the measured RCS would be to the RCS computed with the far-field formulas (physical optics approximation).The best results were obtained with a dual polarized wideband horn antenna in a monostatic configuration, which gave good results with a dihedral corner reflector as reference target, positioned at 3.5 meters distance from the antenna. Successively, the same setup was used to measure the scattering from a gun and a knife, placed at 1 m distance from the antenna. The results are shown in figures A.2 and A.3.

The monostatic measurement setup is shown in figure A.1. The data were acquired in the frequency domain, between 5 and 18 GHz. The horn antenna was connected to a Vector Network Analyzer (VNA), which saved amplitude and phase of the 2-Ports scattering parameters of each target in a Touchstone file. These data were finally processed with MATLAB to compute the RCS of the targets.

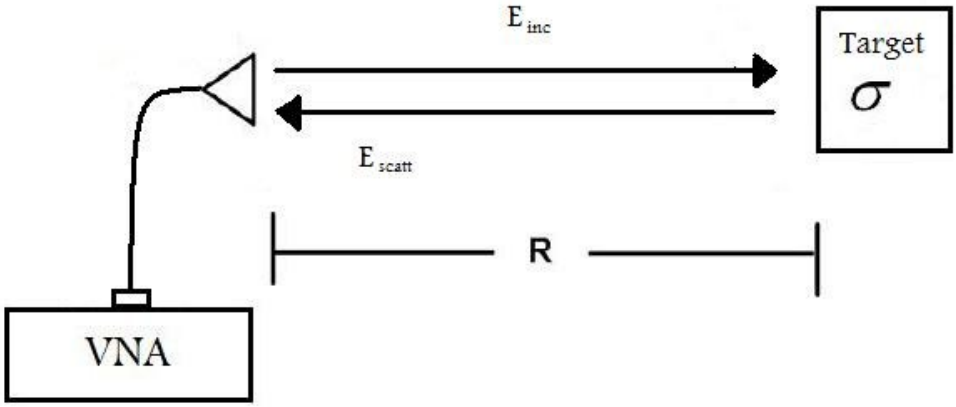

Figure A.1: Monostatic setup used for RCS measurements.

A.1.1 Description of the data processing

A.1.1.1 Background subtraction

The scattering parameters measured for each targets actually represent the phasor sum of the target plus the contribution of the chamber background. One simple technique for reducing the clutter is "background subtraction". The scattering parameters resulting from an empty chamber are also measured and saved, and successively subtracted from the ones measured from the targets. The resulting data is considered to represent the scattering characteristics of the target alone. This technique assumes that there is no shadowing of the chamber by the target and its support, so that the background contribution is not affected by the presence of the target.

A.1.1.2 Time-domain processing of the data

In order to improve the quality of the data, proper pre-processing is required. The frequency domain data are at first transformed into time domain via FFT. Windowing and time gating of the time-domain signal are then applied, in order to avoid ringing and other anti-causal artifacts. The time-domain signals after pre-processing and time gating are shown in figures A.2 and A.3. The pre-processed data are finally re-converted into frequency-domain via IFFT, and successively used to compute the RCS of the targets.

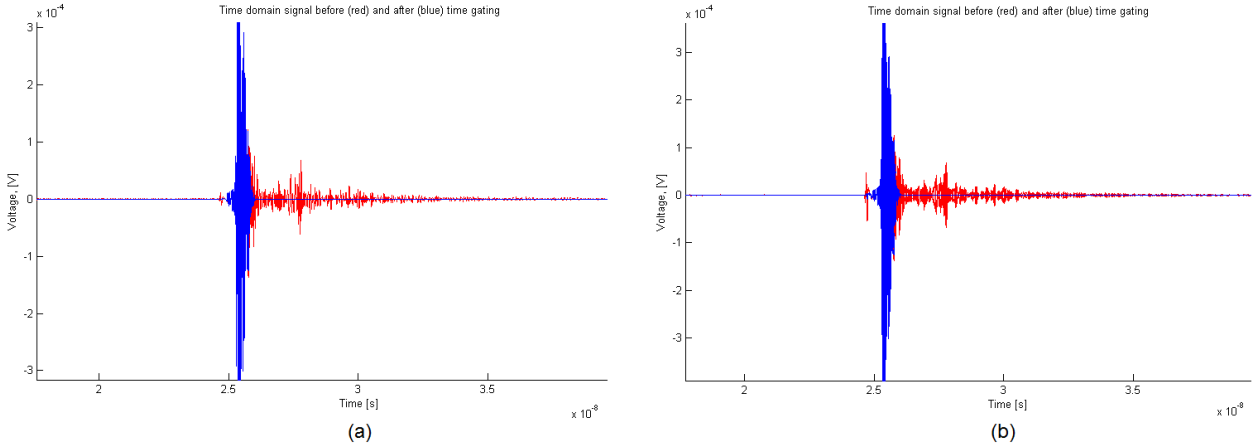

Figure A.2: Time domain signal of dihedral corner reflector, before and after time gating: a) V Polarization; b) H polarization.

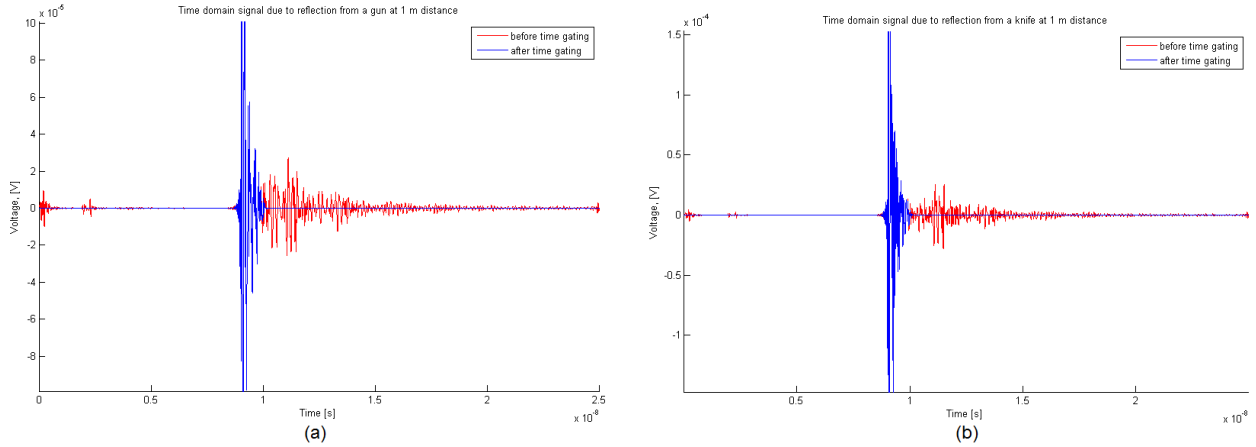

Figure A.3: Time domain signal of typical weapons at 1 m distance, before and after time gating: a) gun; b) knife.

A.1.1.3 Computation of the RCS

The RCS of a target can be computed with the formula:

$$\sigma = \frac{P_{refl}}{P_{transm}} \cdot \frac{(4\pi)^3 R^4}{\lambda^2 G_{rx} G_{tx}} \qquad (A.1)$$

If we consider our measurement setup as a 2-ports Network , the measured scattering parameters represent the voltage ratio of the wave reflected from the target and the transmitted wave:

$$S_{ij}* = \frac{V_{i\_refl}*}{V_{j\_transm}*} \qquad (A.2)$$

where the subscripts "ij" represents respectively input and output port. If we take the squared absolute value of each scattering parameter, we'll obtain the ratio of reflected and transmitted power, like in the RCS formula:

$$|S_{ij}|^2 = \frac{P_{i\_refl}}{P_{j\_transm}} \tag{A.3}$$

In our monostatic setup the horn antenna represents both the ports, which means we need the S11 or S22 parameters, which, given the symmetry of our setup, are theoretically identical. Thus we can choose S11 for the computation of the RCS:

$$\sigma = |S11|^2 \frac{(4\pi)^3 R^4}{\lambda^2 G_{rx} G_{tx}} \tag{A.4}$$

The gain of the Dual Polarized Wideband Horn antenna was measured and used in the computation, and it is shown in figure A.4.

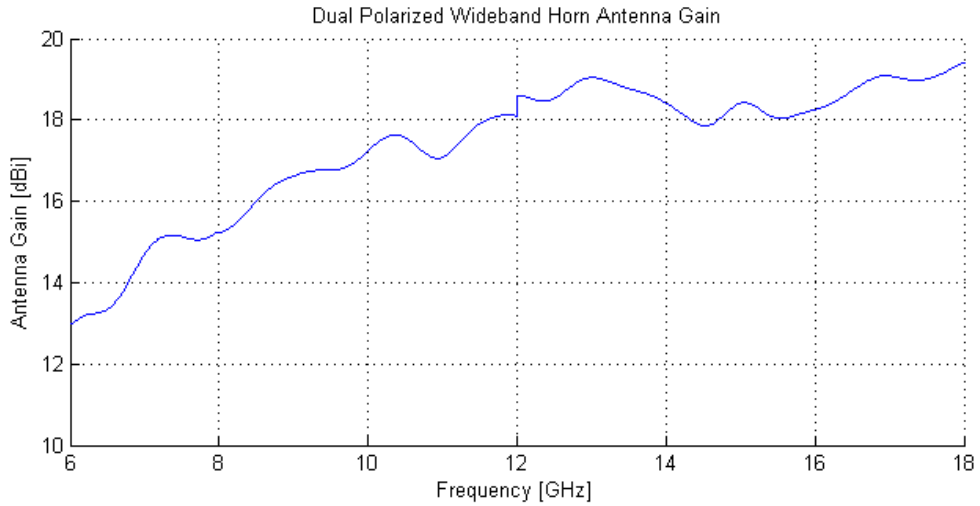

Figure A.4: Dual Polarized Wideband Horn Antenna Gain (dBi).

A.1.1.4 Results

The measured RCS for the dihedral corner reflector, the gun and the knife are shown in figures A.5 and A.6. For the dihedral corner reflector, the measurements were performed both in vertical and horizontal polarization, with the target placed at 3.5 meters distance. From figure A.5 we can

see that the measured RCSs are in average about 2 dBsm higher than the RCS computed with the physical optics formula.

For the gun and the knife, the measured RCS are shown in figure A.6. The RCS of the gun oscillates between a min of -19.4 dBsm and a max of -9.3 dBsm, while the RCS of the knife varies between a min of -12.76 dBsm and -10.02 dBsm. As it can be seen, between 6 and about 8.5 GHz the gun shows a slightly higher RCS than the knife, while from about 8.5 to 18 GHz, the knife response becomes stronger than the gun. Over the 6-18 GHz frequency range, the average RCS of the gun is thus -13.55 dBsm (0.044 m^2), while for the knife we have -11.22 dBsm (0.076 m^2).

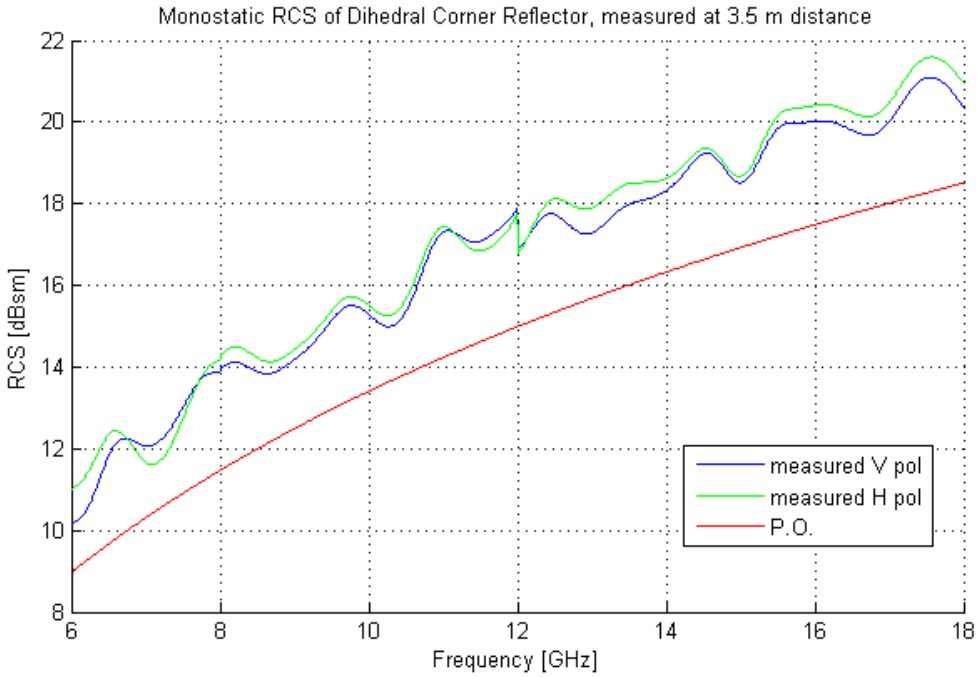

Figure A.5: Comparison of RCS of dihedral corner reflector measured at both polarizations, with the RCS computed with the physical optics formula.

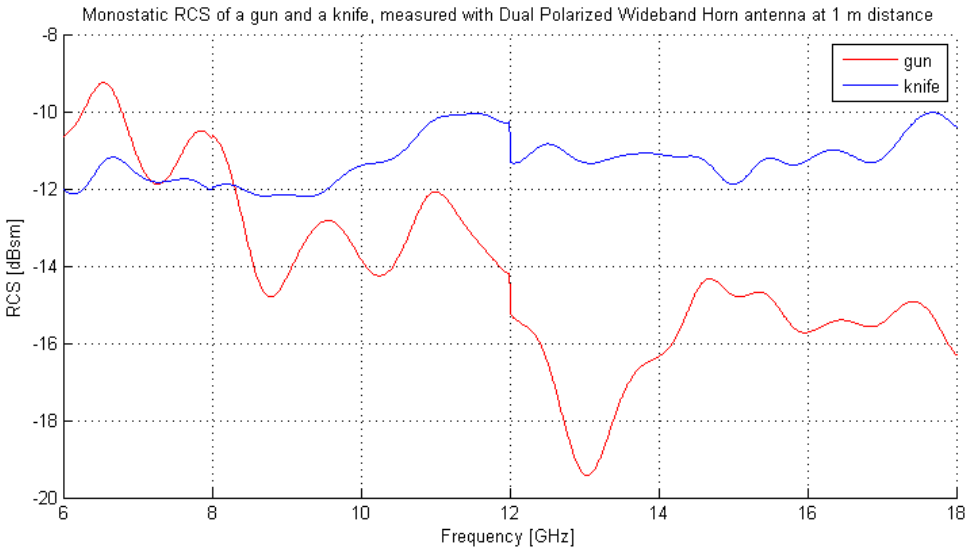

Figure A.6: Radar cross section (dBsm) of a knife and a gun measured at 1 meter distance from the antenna.

A.2 Estimation of reflectivity of human body

In DUCAT, we also performed measurements of human body and metal plate positioned at 0.5 m distance from the Vivaldi antenna used to acquire the data.

The main objective was to measure the reflectivity of the human body in the 6-18 GHz frequency band, in order to estimate the maximum received signal in section 4.1. The procedure followed to process the measured data is very similar to the one used in the previous paragraphs for the weapons, and it will only be briefly reported for simplicity. Anyway, the MATLAB code used to perform these operations is reported in Appendix B.

A.2.1 Processing of measured data

The first operation performed on the measured data was the background subtraction, explained in section A.1.1.1; successively, time gating of the data was performed. As it is noticeable in figure A.7 (c and d), the time-domain signal before processing contains two strong signals: one at about 3-5 ns, corresponding to a distance of about 0.5 m, which is caused by reflections from human body, and another reflection at about 95 ns (14 m distance), representing an unwanted reflection or signal of indiscernible origin, as the maximum size of DUCAT is about 6 m. In any case, this second signal does not represent the reflection from human body, and only the signal at around 3 ns was taken with time gating. Successively, FFT was performed on the time gated signal, obtaining a

signal in the frequency domain. Finally, the reflectivity was estimated via the far-field formula for RCS:

$$\sigma = S_{FFT} \cdot \frac{(4\pi)^3 R^4}{\lambda^2 G_{rx} G_{tx}} \tag{A.5}$$

where S_{FFT} represents the squared absolute value of the resulting frequency-domain signal after FFT.

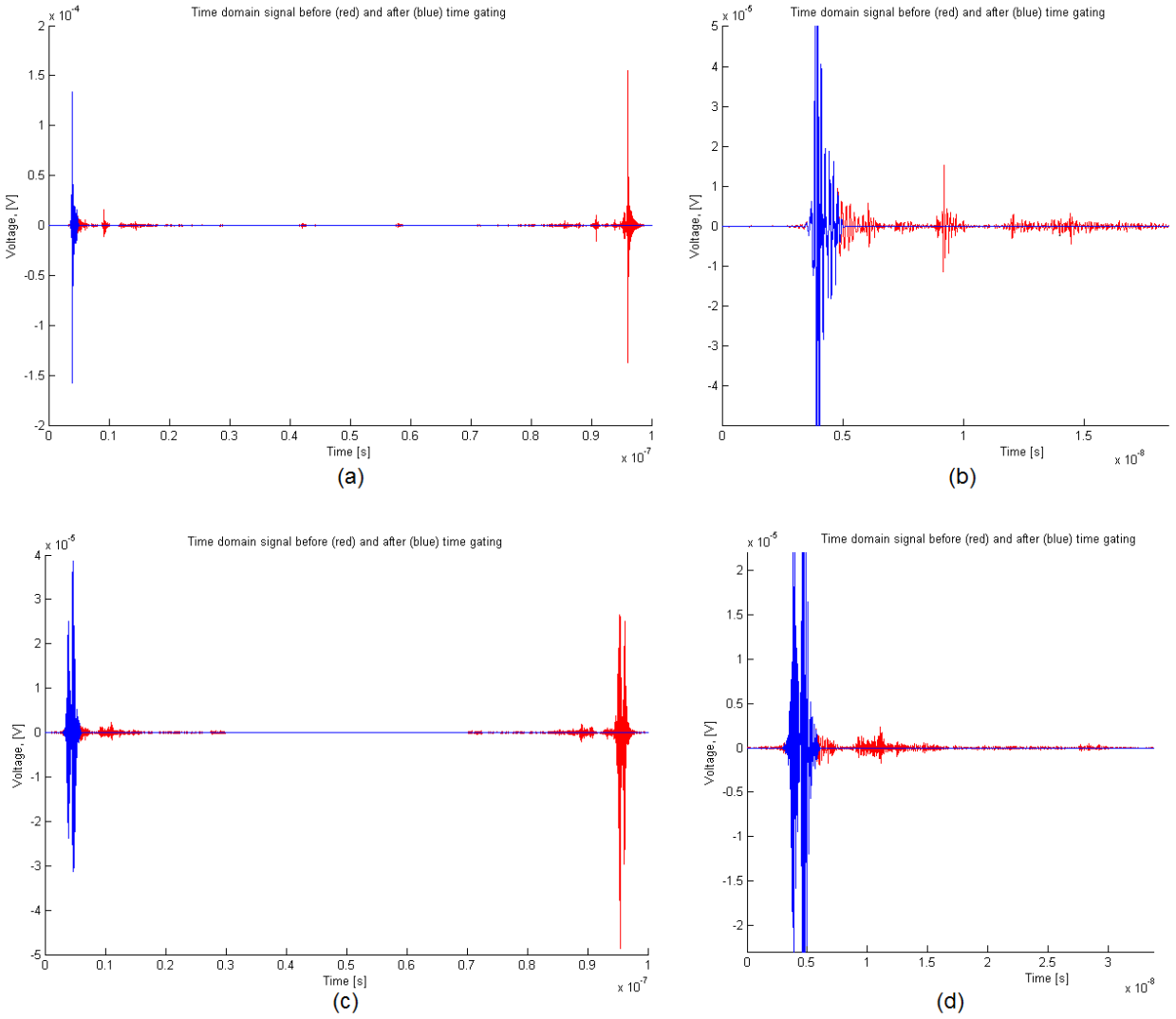

Figure A.7: Time domain signal from reflections at 0.5 m distance: a) and b) metal plate; c) and d) human body.

However, although formula (A.5) is typically used to compute RCS of far-field targets, the data used to estimate human body reflectivity was measured in the near-field, and the RCS computed in this way oscillates a lot. Thus we will use its peak value to estimate the reflectivity of human body, to be used in section 4.1 to estimate stronger signal at receiver's input.

Figure A.8 shows the gain of the Vivaldi antenna used to perform the measurements of human body and metal plate, while A.9 shows the RCS of the gun and the knife and the estimated reflectivity of human body and the metal plate, both computed with (A.5).

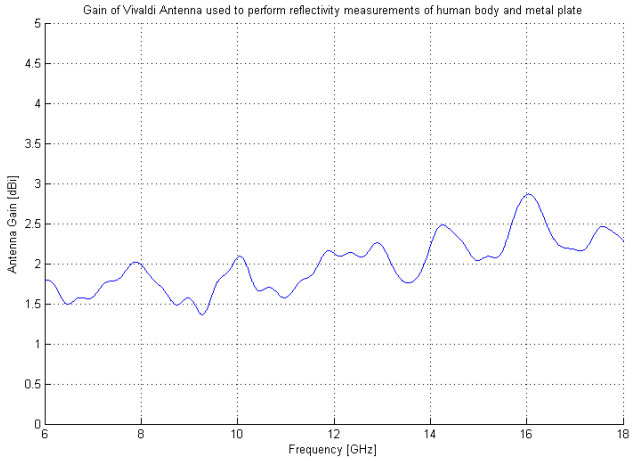

Figure A.8: Gain of Vivaldi antenna used for RCS measurements of human body and metal plate.

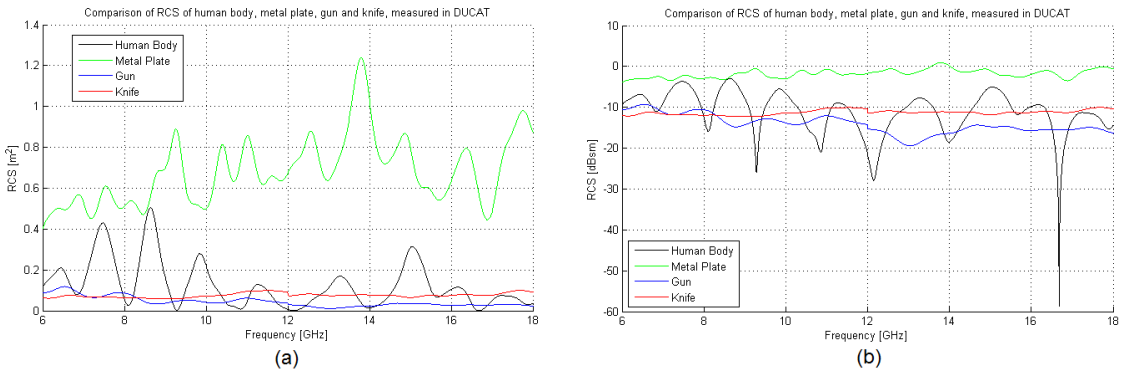

Figure A.9: Comparison of RCS of gun and knife, with estimated reflectivity of human body and metal plate: a) in m^2; b) in dBsm;

As we can see, RCS of weapons appears to be quite close to the magnitude of reflections from human body. However the human reflectivity measured here oscillates a lot due to the near field measurements, and we thus only take its peak value, corresponding to -2.98 dBsm or 0.5 m^2.

Appendix B: MATLAB codes

B.1 RCS measurements in DUCAT: data processing

B.1.1 Function process_gun

```
function [RCS_gun, freq] = process_gun

%% Read and save S-parameters

[BG_S,Nport,freq]=readsp2('BG S11 Gun @1m.s2p',2);
[S,Nport,freq]=readsp2('S11 Gun @1m.s2p',2);

%% Background subtraction

S_NoBG = S - BG_S;

%% Preprocessing

[s,t,Sp_full,ff,H,ph,fh]=tim_freq2time(S_NoBG(:,1,1),1e9,26e9,3e9,5e9,18e9,20e9,
4);
win = ETWin(20808, 1750, 1850, 2050, 2150);
s_win = s.*win';

 % plot the results
figure(1);
hold on;
plot (t,s,'r');
plot (t,s_win,'b');
ylabel('Voltage, [V]')
xlabel('Time [s]')
title('Time domain signal due to reflection from a gun at 1 m distance');
legend ('before time gating', 'after time gating')

% FFT
S_processed = 2*fft(s_win);

%% Compute RCS

load ('Gain_DPWH.mat');         % Gain is in linear scale, for computing RCS
R = 1;                          % Measurement distance [m]
S11 = S_processed(501:1801);    % Only consider values in 5-18 GHz band
freq = ff(501:1801);
Antenna_Gain = g_dpwh;
lambda = 3e8./freq;

RCS_gun = abs(S11).^2.*((4*pi)^3*R^4)./(Antenna_Gain.^2.*lambda.^2);

figure(2);
```

```
hold on;
plot(freq/1e9, 10*log10(RCS_gun))
xlim([6 18]);grid;
xlabel('Frequency [GHz]');ylabel('RCS [dBsm]');
title('Monostatic RCS of a gun, measured with Dual Polarized Wideband Horn
antenna');

save ('Measured_MoRCS_gun_DPWH', 'RCS_gun', 'freq')
```

B.1.2 Function process_knife

```
function [RCS_knife, freq] = process_knife

%% Read and save S-parameters

[BG_S,Nport,freq]=readsp2('BG S11 knife @1m.s2p',2);
[S,Nport,freq]=readsp2('S11 knife @1m.s2p',2);

%% Background subtraction

S_NoBG = S - BG_S;

%% Preprocessing

[s,t,Sp_full,ff,H,ph,fh]=tim_freq2time(S_NoBG(:,1,1),1e9,26e9,3e9,5e9,18e9,20e9,
4);

win = ETWin(20808, 1750, 1850, 2050, 2150);
s_win = s.*win';

 % plot the results
figure(3);
hold on;
plot (t,s,'r');
plot (t,s_win,'b');
ylabel('Voltage, [V]')
xlabel('Time [s]')
title('Time domain signal due to reflection from a knife at 1 m distance');
legend ('before time gating', 'after time gating')

% FFT
S_processed = 2*fft(s_win);

%% Compute RCS

load ('Gain_DPWH.mat');
R = 1;
S11 = S_processed(501:1801);    % Only consider values in 5-18 GHz band
freq = ff(501:1801);
Antenna_Gain = g_dpwh;
lambda = 3e8./freq;

RCS_knife = abs(S11).^2.*((4*pi)^3*R^4)./(Antenna_Gain.^2.*lambda.^2);
```

```
figure(4);
hold on;
plot(freq/1e9, 10*log10(RCS_knife))
xlim([6 18]);grid;
xlabel('Frequency [GHz]');ylabel('RCS [dBsm]');
title('Monostatic RCS of a knife, measured with Dual Polarized Wideband Horn
antenna');

save ('Measured_MoRCS_knife_DPWH', 'RCS_knife','freq')
```

B.1.3 Function process_metal_plate

```
function process_metal_plate

load('MP_50cm001.mat');
S = CpxData;

load('BG_MP50cm001.mat');
BG_S = CpxData;

%% Background subtraction

S_NoBG = S - BG_S; % S_NoBG here is in the form <1x2001x2>

%% Preprocessing

[s,t,Sp_full,ff,H,ph,fh]=tim_freq2time(S_NoBG(1,:,1),5e9,25e9,5.3e9,5.9e9,18e9,2
0e9,4); % position 1

win = ETWin(20008, 620, 720, 1050, 1150); % Metal_plate_NoBG, position 1 and 2

s_win = s.*win';

 % plot the results
figure(1);
hold on;
plot (t,s,'r');
plot (t,s_win,'b');
ylabel('Voltage, [V]')
xlabel('Time [s]')
title('Time domain signal due to reflection from a metal plate at 0.5 m
distance');
legend ('before time gating', 'after time gating');

%% FFT
S_processed = 2*fft(s_win);
% S_processed and ff are defined from 0 to 200 GHz
% in order to have them in 5-18 GHz band:

S_fft_5_18_GHz_MP1 = S_processed(501:1801);
freq = ff(501:1801);

figure(2);
hold on;
```

```
plot(freq/1e9, abs(S_fft_5_18_GHz_MP2).^2)
xlim([6 18]);grid;
xlabel('Frequency [GHz]');ylabel('Magnitude [dBm]');
title('Magnitude of reflection from metal plate at a distance of 0.5 m');

save ('S_fft_MP1', 'S_fft_5_18_GHz_MP1', 'freq')
```

B.1.4 Function process_human_body

```
function process_human_body

load('Tim001.mat');
S = CpxData;
clear CpxData;

load('BG_Tim001.mat');
BG_S = CpxData;
clear CpxData;


%% Background subtraction

S_NoBG = S - BG_S; % S_NoBG here is in the form <1x2001x2>

%% Preprocessing

[s,t,Sp_full,ff,H,ph,fh]=tim_freq2time(S_NoBG(1,:,1),5e9,25e9,5.3e9,5.9e9,18e9,2
0e9,4); % position 1


win = ETWin(20008, 550, 650, 1250, 1350); % Human_NoBG, position 1 and 2

s_win = s.*win';

 % plot the results
figure(1);
hold on;
plot (t,s,'r');
plot (t,s_win,'b');
ylabel('Voltage, [V]')
xlabel('Time [s]')
title('Time domain signal due to reflection from a human body at 0.5 m
distance');
legend ('before time gating', 'after time gating')


%% FFT
S_processed = 2*fft(s_win);
% S_processed and ff are defined from 0 to 200 GHz
% in order to reduce them to 5-18 GHz band:

S_fft_5_18_GHz_human1 = S_processed(501:1801);
freq = ff(501:1801);


figure(2);
hold on;
```

```
plot(freq/1e9, abs(S_fft_5_18_GHz_human2).^2)
xlim([5 18]);grid;
xlabel('Frequency [GHz]');ylabel('Magnitude [?]');
title('Magnitude of reflection from human body at a distance of 0.5 m');


save ('S_fft_human1', 'S_fft_5_18_GHz_human1', 'freq')
```

B.1.5 Function estimate_reflectivity_human_MP

```
function [RCS_MP, RCS_human, freq] = estimate_reflectivity_human_MP

%% Compute RCS

load ('Zhuge_Vivaldi_Gains_5_18_GHz.mat');

R = 0.5; % to be used for human body and metal plate
Antenna_Gain = Gain_rw_5_18_GHz_intp;
lambda = 3e8./freq;
freq = freq;

load ('S_fft_human1.mat');
load ('S_fft_MP1.mat');

RCS_human =
abs(S_fft_5_18_GHz_human1).^2.*((4*pi)^3*R^4)./(Antenna_Gain.^2.*lambda.^2);
RCS_MP =
abs(S_fft_5_18_GHz_MP1).^2.*((4*pi)^3*R^4)./(Antenna_Gain.^2.*lambda.^2);
save ('RCS_human_body_MP', 'RCS_human', 'RCS_MP', 'freq')
```

B.1.6 Function compare_RCS

```
function compare_RCS

load ('Meas_MoRCS_gun_DPWH.mat');
load ('Meas_MoRCS_knife_DPWH.mat');
load ('RCS_human_body_MP');

figure(4);
hold on;
plot(freq/1e9, 10*log10(RCS_human), 'k')
plot(freq/1e9, 10*log10(RCS_MP), 'g')
plot(freq/1e9, 10*log10(RCS_gun), 'b')
plot(freq/1e9, 10*log10(RCS_knife), 'r')
xlim([6 18]);grid;
xlabel('Frequency [GHz]');ylabel('RCS [dBsm]');
legend('Human Body', 'Metal Plate', 'Gun','Knife', 'Location', 'SouthWest')
title('Comparison of RCS of human body, metal plate, gun and knife, measured in
DUCAT');

figure(5);
hold on;
plot(freq/1e9, RCS_human, 'k')
plot(freq/1e9, RCS_MP, 'g')
plot(freq/1e9, RCS_gun, 'b')
```

```
plot(freq/1e9, RCS_knife, 'r')
xlim([6 18]);grid;
xlabel('Frequency [GHz]');ylabel('RCS [m^2]');
legend('Human Body', 'Metal Plate', 'Gun','Knife', 'Location', 'SouthWest')
title('Comparison of RCS of human body, metal plate, gun and knife, measured in
DUCAT');

save ('RCS_comparison', 'RCS_human', 'RCS_MP', 'RCS_gun', 'RCS_knife', 'freq')
```

B.1.7 Function compute_propagation_loss_received_power

```
function compute_propagation_loss_received_power

%% Compute propagation loss for power analysis

load ('RCS_comparison');

Gt = 10^(0.6);      % transmit gain = 6 dBi
Gr = 10^(0.6);      % receive gain = 6 dBi
lambda = 3e8./freq; % wavelenght in the bandwith 6-18 GHz
R = 0.5;            % range to target [m]
Pnoise_dBm = -66.7; % Noise floor at RX input [dBm]
Pt = 10^(1.824-3);  % Transmit power 18.24 dBm
Antenna_Gain = 10^(0.6);                % 6 dBi

L_fs_human = 10*log10(RCS_human.*(Gt*Gr/(4*pi)).*(lambda./(4*pi*R^2)).^2);
L_fs_gun = 10*log10(RCS_gun.*(Gt*Gr/(4*pi)).*(lambda./(4*pi*R^2)).^2);
L_fs_knife = 10*log10(RCS_knife.*(Gt*Gr/(4*pi)).*(lambda./(4*pi*R^2)).^2);

L_fs_gun_1m = 10*log10(RCS_gun.*(Gt*Gr/(4*pi)).*(lambda./(4*pi*(2*R)^2)).^2);
L_fs_knife_1m =
10*log10(RCS_knife.*(Gt*Gr/(4*pi)).*(lambda./(4*pi*(2*R)^2)).^2);

L_fs_gun_1p5m = 10*log10(RCS_gun.*(Gt*Gr/(4*pi)).*(lambda./(4*pi*(3*R)^2)).^2);
L_fs_knife_1p5m =
10*log10(RCS_knife.*(Gt*Gr/(4*pi)).*(lambda./(4*pi*(3*R)^2)).^2);

L_fs_gun_2m = 10*log10(RCS_gun.*(Gt*Gr/(4*pi)).*(lambda./(4*pi*(4*R)^2)).^2);
L_fs_knife_2m =
10*log10(RCS_knife.*(Gt*Gr/(4*pi)).*(lambda./(4*pi*(4*R)^2)).^2);

Pr_human_dBm = 18.24 + L_fs_human;
Pr_gun_50cm_dBm = 18.24 + L_fs_gun;
Pr_knife_50cm_dBm = 18.24 + L_fs_knife;

Pr_gun_1m_dBm = 18.24 + L_fs_gun_1m;
Pr_knife_1m_dBm = 18.24 + L_fs_knife_1m;

Pr_gun_1p5m_dBm = 18.24 + L_fs_gun_1p5m;
Pr_knife_1p5m_dBm = 18.24 + L_fs_knife_1p5m;

Pr_gun_2m_dBm = 18.24 + L_fs_gun_2m;
Pr_knife_2m_dBm = 18.24 + L_fs_knife_2m;

figure(1);
```

```
hold on;
plot(freq/1e9, L_fs_human,'k')
plot(freq/1e9, L_fs_gun,'b')
plot(freq/1e9, L_fs_knife,'r')
xlim([6 18]);grid;
xlabel('Frequency [GHz]');ylabel('Propagation loss [dB]');
title('Propagation loss due to reflections from human body and typical
targets');
legend('Human Body at 0.5 m', 'Gun at 0.5 m', 'Knife at 0.5 m', 'Location',
'SouthWest')
save ('Propagation_Loss@0.5m', 'L_fs_human', 'L_fs_gun', 'L_fs_knife', 'freq')

figure(2);
hold on;
plot(freq/1e9, L_fs_human,'k')
plot(freq/1e9, L_fs_gun_1m,'b')
plot(freq/1e9, L_fs_knife_1m,'r')
xlim([6 18]);grid;
xlabel('Frequency [GHz]');ylabel('Propagation loss [dB]');
title('Propagation loss due to reflections from human body and typical
targets');
legend('Human Body at 0.5 m', 'Gun at 1 m', 'Knife at 1 m', 'Location',
'SouthWest')
save ('Propagation_Loss_strong_weak', 'L_fs_human', 'L_fs_gun_1m',
'L_fs_knife_1m', 'freq')

figure(3);
hold on;
plot(freq/1e9, L_fs_human,'k')
plot(freq/1e9, L_fs_gun_1p5m,'b')
plot(freq/1e9, L_fs_knife_1p5m,'r')
xlim([6 18]);grid;
xlabel('Frequency [GHz]');ylabel('Propagation loss [dB]');
title('Propagation loss due to reflections from human body and typical
targets');
legend('Human Body at 0.5 m', 'Gun at 1.5 m', 'Knife at 1.5 m', 'Location',
'SouthWest')
save ('Propagation_Loss_strong_weak', 'L_fs_human', 'L_fs_gun_1m',
'L_fs_knife_1m', 'freq')

figure(4);
hold on;
plot(freq/1e9, L_fs_human,'k')
plot(freq/1e9, L_fs_gun_2m,'b')
plot(freq/1e9, L_fs_knife_2m,'r')
xlim([6 18]);grid;
xlabel('Frequency [GHz]');ylabel('Propagation loss [dB]');
title('Propagation loss due to reflections from human body and typical
targets');
legend('Human Body at 0.5 m', 'Gun at 2 m', 'Knife at 2 m', 'Location',
'SouthWest')
save ('Propagation_Loss_strong_weak', 'L_fs_human', 'L_fs_gun_1m',
'L_fs_knife_1m', 'freq')


figure(5);
hold on;
plot(freq/1e9, Pr_human_dBm,'k')
plot(freq/1e9, Pr_gun_dBm,'b')
plot(freq/1e9, Pr_knife_dBm,'r')
```

```
plot(freq/1e9, Pnoise_dBm,'g')
xlim([6 18]);grid;
xlabel('Frequency [GHz]');ylabel('Received Power [dBm]');
legend('Human Body at 0.5 m', 'Gun at 0.5 m', 'Knife at 0.5 m', 'Noise floor',
'Location', 'SouthWest')
title('Received power at RX input due to reflections from human body and typical
targets');

figure(6);
hold on;
plot(freq/1e9, Pr_human_dBm+15,'k')
plot(freq/1e9, Pr_gun_dBm+15,'b')
plot(freq/1e9, Pr_knife_dBm+15,'r')
xlim([6 18]);grid;
xlabel('Frequency [GHz]');ylabel('Received Power [dBm]');
title('Received power at mixer output due to reflections from human body and
typical targets');
legend('Human Body at 0.5 m', 'Gun at 0.5 m', 'Knife at 0.5 m', 'Location',
'SouthWest')

figure(7);
hold on;
plot(freq/1e9, Pr_human_dBm,'k')
plot(freq/1e9, Pr_gun_1m_dBm,'b')
plot(freq/1e9, Pr_knife_1m_dBm,'r')
plot(freq/1e9, Pnoise_dBm,'g')
xlim([6 18]);grid;
xlabel('Frequency [GHz]');ylabel('Received Power [dBm]');
title('Received power at RX input due to reflections from human body and typical
targets');
legend('Human Body at 0.5 m', 'Gun at 1 m', 'Knife at 1 m', 'Noise floor',
'Location', 'SouthWest')

figure(8);
hold on;
plot(freq/1e9, Pr_human_dBm+15,'k')
plot(freq/1e9, Pr_gun_1m_dBm+15,'b')
plot(freq/1e9, Pr_knife_1m_dBm+15,'r')
xlim([6 18]);grid;
xlabel('Frequency [GHz]');ylabel('Received Power [dBm]');
legend('Human Body at 0.5 m', 'Gun at 1 m', 'Knife at 1 m', 'Location',
'SouthWest')
title('Received power at mixer output due to reflections from human body and
typical targets');

figure(9);
hold on;
plot(freq/1e9, Pr_human_dBm,'k')
plot(freq/1e9, Pr_gun_1p5m_dBm,'b')
plot(freq/1e9, Pr_knife_1p5m_dBm,'r')
plot(freq/1e9, Pnoise_dBm,'g')
xlim([6 18]);grid;
xlabel('Frequency [GHz]');ylabel('Received Power [dBm]');
title('Received power at RX input due to reflections from human body and typical
targets');
legend('Human Body at 0.5 m', 'Gun at 1.5 m', 'Knife at 1.5 m', 'Noise floor',
'Location', 'SouthWest')

figure(10);
hold on;
```

```
plot(freq/1e9, Pr_human_dBm+15,'k')
plot(freq/1e9, Pr_gun_1p5m_dBm+15,'b')
plot(freq/1e9, Pr_knife_1p5m_dBm+15,'r')
xlim([6 18]);grid;
xlabel('Frequency [GHz]');ylabel('Received Power [dBm]');
legend('Human Body at 0.5 m', 'Gun at 1.5 m', 'Knife at 1.5 m', 'Location',
'SouthWest')
title('Received power at mixer output due to reflections from human body and
typical targets');


figure(11);
hold on;
plot(freq/1e9, Pr_human_dBm,'k')
plot(freq/1e9, Pr_gun_2m_dBm,'b')
plot(freq/1e9, Pr_knife_2m_dBm,'r')
plot(freq/1e9, Pnoise_dBm,'g')
xlim([6 18]);grid;
xlabel('Frequency [GHz]');ylabel('Received Power [dBm]');
title('Received power at RX input due to reflections from human body and typical
targets');
legend('Human Body at 0.5 m', 'Gun at 2 m', 'Knife at 2 m', 'Noise floor',
'Location', 'SouthWest')

figure(12);
hold on;
plot(freq/1e9, Pr_human_dBm+15,'k')
plot(freq/1e9, Pr_gun_2m_dBm+15,'b')
plot(freq/1e9, Pr_knife_2m_dBm+15,'r')
xlim([6 18]);grid;
xlabel('Frequency [GHz]');ylabel('Received Power [dBm]');
legend('Human Body at 0.5 m', 'Gun at 2 m', 'Knife at 2 m', 'Location',
'SouthWest')
title('Received power at mixer output due to reflections from human body and
typical targets');

figure(13);
hold on;
plot(freq/1e9, Pr_gun_dBm-Pnoise_dBm,'b')
plot(freq/1e9, Pr_knife_dBm-Pnoise_dBm,'r')
xlim([6 18]);grid;
xlabel('Frequency [GHz]');ylabel('Signal-to-Noise Ratio [dB]');
title('SNR at RX input due to reflections from typical targets at 0.5 m
distance');
legend('Gun', 'Knife', 'Location', 'SouthWest')

figure(14);
hold on;
plot(freq/1e9, Pr_gun_1m_dBm-Pnoise_dBm,'b')
plot(freq/1e9, Pr_knife_1m_dBm-Pnoise_dBm,'r')
xlim([6 18]);grid;
xlabel('Frequency [GHz]');ylabel('Signal-to-Noise Ratio [dB]');
title('SNR at RX input due to reflections from typical targets at 1 m
distance');
legend('Gun', 'Knife', 'Location', 'SouthWest')

figure(15);
hold on;
plot(freq/1e9, Pr_gun_1p5m_dBm-Pnoise_dBm,'b')
plot(freq/1e9, Pr_knife_1p5m_dBm-Pnoise_dBm,'r')
```

```
xlim([6 18]);grid;
xlabel('Frequency [GHz]');ylabel('Signal-to-Noise Ratio [dB]');
title('SNR at RX input due to reflections from typical targets at 1.5 m
distance');
legend('Gun', 'Knife', 'Location', 'SouthWest')

figure(16);
hold on;
plot(freq/1e9, Pr_gun_2m_dBm-Pnoise_dBm,'b')
plot(freq/1e9, Pr_knife_2m_dBm-Pnoise_dBm,'r')
xlim([6 18]);grid;
xlabel('Frequency [GHz]');ylabel('Signal-to-Noise Ratio [dB]');
title('SNR at RX input due to reflections from typical targets at 2 m
distance');
legend('Gun', 'Knife', 'Location', 'SouthWest')
```

B.2 Phase noise

B.2.1 Function Receiver_noise

```
function [N_out_dBm] = Receiver_noise

%% Receiver's parameters

F_sw = 10^(0.4);              % F switch plus RF-cable = 4 dB
G_sw = 10^(0-0.4);            % G switch plus RF-cable = -4 dB
F_lna = 10^(0.25);            % F LNA = 2.5 dB
G_lna = 10^(2.8);             % G LNA = 28 dB
F_mix = 10^(1.05);            % F mixer = 10.5 dB
G_mix = 10^(0-1.2);           % G mixer = -12 dB
Gtot  = G_mix*G_lna*G_sw;     % Total gain of receiver


%% Receiver's Noise factor
F = F_sw + (F_lna-1)/G_sw + (F_mix-1)/(G_sw*G_lna);

%% Receiver's Noise figure
N_F = 10*log10(F);          % Noise figure of receiver

%% Receiver's Noise temperature:

T0 = 290;                     % Ambient temperature [K]
Tn = (F-1)*T0;                % Receiver's Noise temperature [K]

%% Thermal noise at receiver's input

k = 1.38e-23;                 % Boltzmann's constant [J/K]
B = 12e9;                     % Operational Bandwidth [Hz]

% Time domain:

N0 = k*B*T0;                  % Thermal noise at receiver's input due to
environmental temp.[W]
```

```
N0_dBm = 30+10*log10(N0);      % Thermal noise at receiver's input [dBm]

%% Total noise power at receiver's input

k = 1.38e-23;                          % Boltzmann's constant [J/K]
B = 12e9;                              % Operational Bandwidth [Hz]

% Time Domain:
N_in = k*B*F*T0;                       % Total noise power at receiver's input
[W]
N_in_dBm = 30+10*log10(N_in);          % Total noise power at receiver's input
[dBm]

%% Noise Power at mixer's output

T_sw = 5e-4;                           % Sweep Time [s] scheme

% Frequency Domain:
N_out = k*F*T0*Gtot/T_sw;              % Total noise power at receiver's output
[W]
N_out_dBm = 30+10*log10(N_out);        % Total noise power at receiver's output
[dBm]
```

B.2.2 Function N_ant

```
function [N_ant]= N_ant (R, d_ant)

%% Phase noise due to antenna reflections at mixer IF output

B = 12e9;                      % Operational Bandwidth [Hz]
c = 2.3e8;                     % Speed of electromagnetic wave in RF-cables [m/s]
P_rf = 10^(1.824-3);           % Power driven at antenna [W]or 18.24 dBm
G_sw = 10^(0-0.4);             % G switch plus RF_cable = -4 dB
G_lna = 10^(2.8);              % G LNA = 28 dB
G_mix = 10^(0-1.2);            % G mixer = -12 dB
Grec = G_mix*G_lna*G_sw;       % Total gain of receiver
Iant = 10^(2.5);               % Antenna isolation 25 dB
Tsw = 5e-4;                    % Sweep Time (s)
SS = 10^(0-12.96+2*log10(2)); % Single-sideband oscillator phase noise density
                               % w.r.t. carrier [dBc/Hz]; -129.6 dBc/Hz @ 320 Khz
offset

% Phase noise correlation coefficient antenna:
K_ant = 4*(sin(pi*2*R*B/(c*Tsw).*d_ant/c)).^2;

% Phase noise due to antenna reflections at mixer IF output:
N_ant = P_rf*SS.*K_ant.*Grec./(Tsw*Iant); % [W]
```

B.2.3 Function N_mix

```
function [N_mix]= N_mix (R, d_mix)
```

```
%% Phase noise due to antenna reflections at mixer IF output



B = 12e9;                       % Operational Bandwidth [Hz]
c = 2.3e8;                      % Speed of electromagnetic wave in RF-cables [m/s]
Lcpl_f = 10^(1.046);            % Coupling Loss Coupler 10+0.46 dB
P_rf = 10^(2.95);               % Input Power at coupler's [W] or 29.5 dBm
G_sw = 10^(0-0.4);              % G switch and RF-cable = -4 dB
G_lna = 10^(2.8);               % G LNA = 28 dB
G_mix = 10^(0-1.2);             % G mixer = -12 dB
Grec  = G_mix*G_lna*G_sw;       % Total gain of receiver
Lmix_iso = 10^(2);              % Mixer LO-to-RF isolation 20 dB
Tsw = 5e-4;                     % Sweep Time (s)
SS = 10^(0-12.96+2*log10(2)); % Single-sideband oscillator phase noise density
                                % w.r.t. carrier [dBc/Hz]; -129.6 dBc/Hz @ 320 Khz
offset
Refl = 10^((0-10)/10);          % Reflection coefficient, given 10 dB return loss

% Phase noise correlation coefficient antenna:
K_mix = 4*(sin(pi*2*R*B/(c*Tsw).*d_mix/c)).^2;

% Phase noise due to antenna reflections at mixer IF output:
N_mix = P_rf*(abs(Refl)^2)*SS.*K_mix*Grec/(Tsw*Lcpl_f*Lmix_iso); % [W]
```

B.2.4 Function N_obj

```
function [N_obj, freq] = N_obj (R_obj, RCS_obj)

%% Phase noise due to short-range object at mixer IF output

B = 12e9;                     % Operational Bandwidth [Hz]
c = 2.3e8;                      % Speed of light [m/s]
Gtx = 10*log10(6/10);         % Transmit Gain 6 dBi
Grx = 10*log10(6/10);         % Receive Gain 6 dBi
freq = (60:180)*1e8;          % range of frequencies 6-18 GHz [Hz] with 121
values
lambda = c./freq;             % Wavelength [m]
P_rf = 10^(1.824-3);          % Power driven at antenna [W] or 18.24 dBm
Tsw = 5e-4;                   % Sweep Time [s]
G_sw = 10^(0-0.4);            % G switch and RF-cable = -4 dB
G_lna = 10^(2.8);             % G LNA = 28 dB
G_mix = 10^(0-1.2);           % G mixer = -12 dB
Grec  = G_mix*G_lna*G_sw;     % Total gain of receiver
SS = 10^(0-11.76+2*log10(2)); % Single-sideband oscillator phase noise density
                               % w.r.t. carrier [dBc/Hz]; -117.6 dBc/Hz @ 80 Khz
offset

% Phase noise correlation coefficient antenna:
K_obj = 4*(sin(pi*2.*R_obj*B/(c*Tsw)*2.*R_obj/c)).^2;

% Phase noise due to short-range pbject at mixer IF output:
N_obj =
P_rf*Gtx*Grx*SS.*K_obj*Grec.*RCS_obj.*(lambda.^2)./((4*pi)^3*Tsw.*R_obj.^4);   %
[W]
```

B.2.4 Function Total_noise_power

```
function Total_noise_power

%% Common Variables

% R = (10:2:250)/100;          % Range to target between 0.1 and 2.5 [m] with 121
values

%% Thermal noise and Noise figure

[Nf_out_dBm] = Receiver_noise;

Nf_out = 10^((Nf_out_dBm-30)/10);

%% Phase noise due to antenna crosstalk at mixer IF output

d_ant = 0.05;               % time diff. source-to-LO mixer port and source-to-
tx-antenna-to-rx-antenna-RF port mixer [m]

[N_antenna] = N_ant (R, d_ant);        % Phase Noise [W]
N_ant_dBm = 30+10*log10(N_antenna);    % Phase Noise [dBm]

%% Phase noise due to Mixer LO leakage at mixer IF output

d_mix = 4;

[N_mixer] = N_mix (R, d_mix);          % Phase Noise [W]
N_mix_dBm = 30+10*log10(N_mixer);      % Phase Noise [dBm]

%% Phase noise due to short-range object at mixer IF output

RCS_obj = 1;                              % RCS of target [m^2]

[N_object, freq] = N_obj(R,RCS_obj);     % Phase Noise [W]
N_obj_dBm = 30+10*log10(N_object);       % Phase Noise [dBm]



%% Total Phase Noise

N_ph = N_antenna+N_mixer+max(N_object); % [W]
N_tot = N_ph+Nf_out;                    % [W]

% save ('Phase_noise@IF_output_vs_range.mat','N_antenna', 'N_mixer', 'N_object',
'N_ph', 'N_tot', 'R')
% save ('Phase_noise@IF_output_vs_delta.mat','N_antenna', 'N_mixer', 'N_object',
'N_ph','N_tot', 'delta')


%% Plot Noise vs Range

figure(1);
```

```
hold on;
plot(R, 30+10*log10(N_antenna),'r' )
plot(R, 30+10*log10(N_mixer),'g' )
plot(R, 30+10*log10(N_object),'b' )
plot(R, 30+10*log10(N_ph),'k')

grid; xlabel('Range to target [m]'); ylabel('Noise Power [dBm]');
title('Phase noise contributions at mixer IF output, with maximum path length
difference');
legend('Phase noise antenna', 'Phase noise Mixer', 'Phase noise short-range
target', 'Total phase noise','Location', 'SouthEast')

figure(4);
hold on;
plot(R, 30+10*log10(N_ph),'b' )
plot(R, 30+10*log10(N_tot),'k' )
plot(R, Nf_out_dBm,'r' )
grid; xlabel('Range to target [m]'); ylabel('Noise Power [dBm]');
title('Total noise spectral density at mixer IF output, with maximum path lenght
difference');
legend('Total phase noise','Total Noise', 'Receiver Noise' ,'Location', 'Best')
```

B.3 Load and plot ADS dataset

B.3.1 Function load_and_plot_ADS_dataset

```
function load_and_plot_ADS_dataset

fid                 = fopen(strcat('ADS_dataset_filename.txt'));
[freq, beat_signal] = extract_data (fid);


%% Plot data

figure(1);
hold on;
plot(freq/1e6,beat_signal)
grid;
xlabel('Beat Frequency [MHz]');ylabel('Beat Signal [dBm]');
title('Beat signal of RF-scheme simulated in ADS')
```

B.3.2 Function extract_data

```
function [freq, beat_signal] = extract_data (fid)

data_cellarray      = textscan(fid , '%s'); % extract data in a cell-array
new_cell_array      = data_cellarray{1};
char_array          = char(new_cell_array); %transform data to char for better
handling
max_index           = size(char_array);
freq                = [];
```

```
beat_signal         = [];

counter             = 0;
for index=3:2:max_index
    counter             = counter+1;
    X_axis(1,counter)   = textscan(char_array(index,:), '%f');
    freq (1,counter)    = X_axis {1,counter};
end;

counter             =0;
for index=4:2:max_index
    counter             = counter+1;
    Y_axis(1,counter)   = textscan(char_array(index,:), '%f');
    beat_signal (1,counter)    = Y_axis {1,counter};

end;
```

Appendix C: Selected RF-components' datasheets

YIG-tuned Oscillator:

MICRO LAMBDA WIRELESS, INC.

MLMH SERIES HIGH SPEED YIG TUNED OSCILLATORS VXI/ VME

FEATURES

- 2-8 GHz Frequency Coverage
- 80 uS/GHz Tuning Speed
- FM/Phase Lock Port
- 1% Linearity Under Sweep
- High Reliability

DESCRIPTION

Micro Lambda, Inc. a leader in the development of next generation YIG devices now offers "High Speed" miniature YIG sources covering octave and multi-octave frequencies in the 2 to 8 GHz range. Designed specifically for speed, these oscillators tune 10 times faster than conventional YIG oscillators for new fast acquisition Test Equipment, Synthesizers, Single Slot VXI or VME based Instruments, as well as a multitude of general applications.

This series of YIG oscillators have been specifically designed for "Fast Tuning" applications. They incorporate a low inductance tuning coil in a small magnet structure covering standard frequency bands of 2-4, 3-6, 4-8 and 2-8 GHz. Performance characteristics of this family of oscillators is consistent with the standard MLMY-Series miniature oscillators. Typical phase noise of a 2-8 GHz "Fast Tune" oscillator at 100 kHz offset is -120 dBc/Hz. They provide +13 dBm power output, frequency linearity under sweep conditions of 1% with a 500 us ramp. Utilizing standard analog driver techniques with +24 Volt & -15 Volt inputs, the tuning speed of a 2-8 GHz oscillator is 80 uS per GHz to an accuracy of ±10 MHz. With +15 Volt / -15 Volt driver inputs, the tuning speed is 100 us per GHz to an accuracy of ±10 MHz.

ELECTRICAL AND PERFORMANCE SPECIFICATIONS

Guaranteed Specifications at –0° to +65° C Case Temperature

Model No.	MLMH-0204	MLMH-0306	MLMH-0408	MLMH-0208
Frequency Range, Min.	2-4 GHz	3-6 GHz	4-8 GHz	2-8 GHz
Power Output, Min.	+14 dBm	+14 dBm	+14 dBm	+13 dBm
Power Output Variation, Max.	+/- 2 dB	+/- 2 dB	+/- 2 dB	+/- 2 dB
Frequency Drift over Temperature, Max.	15 MHz	15 MHz	15 MHz	15 MHz
Pulling Figure (12 dB RL), Typ.	1 MHz	1 MHz	1 MHz	1 MHz
Pushing Figure +15 Vdc Supply, Typ.	0.1 MHz/V	0.1 MHz/V	0.1 MHz/V	0.1 MHz/V
-5 Vdc Supply, Typ.	1 MHz/V	1 MHz/V	1 MHz/V	1 MHz/V
Magnetic Susceptability @ 60 Hz, Typ.	110 kHz/gauss	110 kHz/gauss	110 kHz/gauss	110 kHz/gauss
2nd Harmonic, Min.	-12 dBc	-12 dBc	-12 dBc	-12 dBc
3rd Harmonic, Min.	-20 dBc	-20 dBc	-20 dBc	-20 dBc
Spurious Output, Min.	-70 dBc	-70 dBc	-70 dBc	-70 dBc
Phase Noise @ 10kHz Offset	-103 dBc/Hz	-100 dBc/Hz	-100 dBc/Hz	-98 dBc/Hz
@ 100kHz Offset	-123 dBc/Hz	-123 dBc/Hz	-120 dBc/Hz	-120 dBc/Hz
Main Coil				
Sensitivity, Typ.	10 MHz/mA	10 MHz/mA	10 MHz/mA	10 MHz/mA
3 dB Bandwidth, Typ.	25 kHz	25 kHz	25 kHz	25 kHz
Linearity, Typ.	+/- 0.25 %	+/- 0.25 %	+/- 0.25 %	+/- 0.25 %
Hysteresis, Typ.	3 MHz	3 MHz	5 MHz	8 MHz
Input Impedance @ 1 kHz, Typ.	4 Ohm / 4 mH	4 Ohm / 4 mH	4 Ohm / 4 mH	4 Ohm / 4 mH
FM Coil				
Sensitivity, Typ.	310 kHz/ma	310 kHz/ma	310 kHz/ma	310 kHz/ma
3 dB Bandwidth, Typ.	3 MHz	3 MHz	3 MHz	3 MHz
Deviation @ 400 kHz Rate, Min.	+/- 50 MHz	+/- 50 MHz	+/- 50 MHz	+/- 50 MHz
Input Impedance @ 1 MHz, Typ.	0.3 Ohm / 1.4uH	0.3 Ohm / 1.4uH	0.3 Ohm / 1.4uH	0.3 Ohm / 1.4uH
DC Circuit Power, Max.+15 Vdc +/- 5%	100 mA	100 mA	100 mA	100 mA
-5 Vdc +/- 5%	50 mA	50 mA	50 mA	50 mA
YIG Heater Power				
Input Voltage Range	+24 +/- 4 Vdc	+24 +/- 4 Vdc	+24 +/- 4 Vdc	+24 +/- 4 Vdc
Current Surge/Steady State, Max.	250 mA / 25 mA	250 mA / 25 mA	250 mA / 25 mA	250 mA / 25 mA
Case Style	81-041-1	81-041-1	81-041-1	81-041-1

Micro Lambda Wireless, Inc. - 46515 Landing Parkway, Fremont California 94538 * Phone (510) 770-9221 * Fax (510) 770-9213

Sales Quotation

Date : [redacted]
Customer No. : [redacted]
Doc. Number : [redacted]
Currency : **EUR**
Your Reference : [redacted]

TU Delft
Attn. Mr. E. Pasqua
Julianalaan 136
2628 BL DELFT

Dear Mr. Pasqua,

We thank you for your interest in our products and we herewith have the pleasure of sending you our quotation without engagement in accordance with the main terms & conditions of the Instrument Branch FHI.

	Item Code	*Quantity*	*Price*	*VAT*	*Total*
1	**MLMH-xxxx** Oscillator, High Speed Frequency: 3.0 - 9.0 GHz Output Power: +14 dBm min. Warranty : 12 months Country of origin : US Statistics number : 85299097 Manufacturer : Micro Lambda	1	1.890,00	H	1.890,00

Frequency Doubler FDMP20401 by Teledyne Cougar:

TELEDYNE COUGAR
A Teledyne Technologies Company

Rev. 5/10

FDMP20401 2.0 TO 10.0 GHz: INPUT 4.0 TO 20.0 GHz: OUTPUT FREQUENCY DOUBLER

Typical Values	FDMP20401
Input Frequency	2.0 - 10.0 GHz
Output Frequency	4.0 - 20.0 GHz
Conversion Loss	10.5 dB
Input Drive (nominal)	+10.0 dBm
High Fundamental Suppression	40.0 dBc
Seam Sealed Hermetic Cougar MixerPak Package	

SPECIFICATIONS*

Parameter	Port	Frequency (GHz)	Typ. (dB)	Guaranteed -55 to +85 °C Max. (dB)
SSB Conversion Loss and SSB Noise Figure	f_{IN}	3.0 to 8.0	10.0	11.5
	f_{OUT}	6.0 to 16.0	10.0	11.5
		2.0 to 10.0	10.5	12.0
		4.0 to 20.0	10.5	12.0
			Typ. (dB)	Min. (dB)
Suppression^				
Fundamental	f_{IN}	2.0 to 10.0	32	25
Third Harmonics	f_{IN}	2.0 to 4.0	50	40
	f_{IN}	4.0 to 8.0	38	28
	f_{IN}	8.0 to 10.0	45	32
Fifth Harmonics	f_{IN}	2.0 to 10.0	50	40

* Measured in a 50-ohm system with nominal input drive of +10 dBm.
^ Fundamental and harmonic suppression is referenced to the fundamental input.

ABSOLUTE MAXIMUM RATINGS

Storage Temperature	-65 to +125 °C
Peak Input Power	+23 dBm @ 25 °C
	derate to +17 dBm @ 100 °C
Peak Input Current @ 25°C	50 mA DC

FDMP20401

Cougar MixerPak for Frequency Doubler

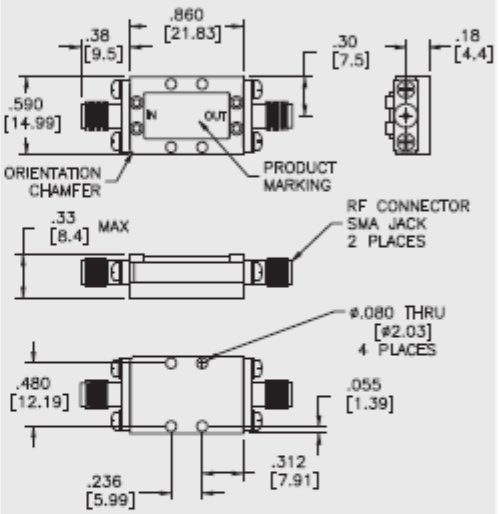

TYPICAL PERFORMANCE

KEY: +25 []C ——
+85 []C -·-·-
-55 []C – – –

Conversion Loss vs Input Frequency

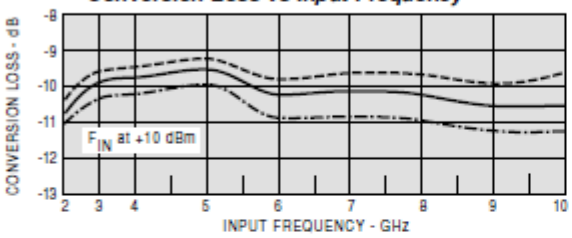

Conversion Loss vs Input Frequency

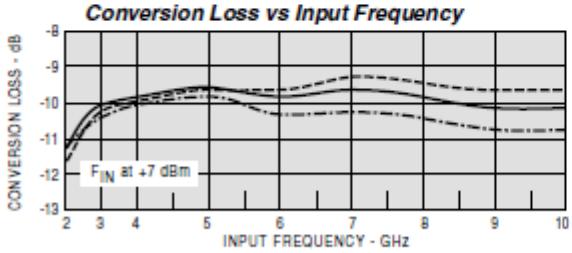

Fundamental Suppression vs Input Frequency[1]

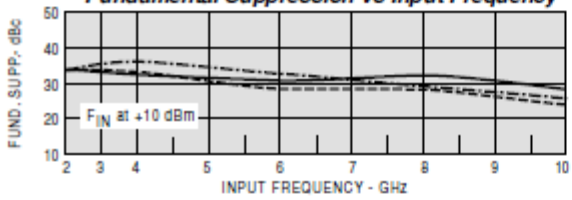

Fundamental Suppression vs Input Frequency[1]

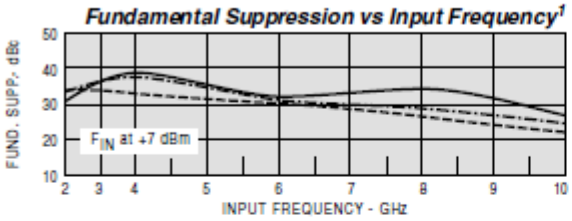

Input VSWR vs Input Frequency

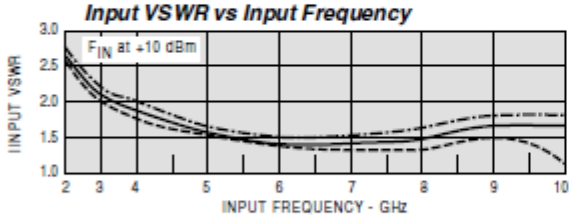

Input VSWR vs Input Frequency

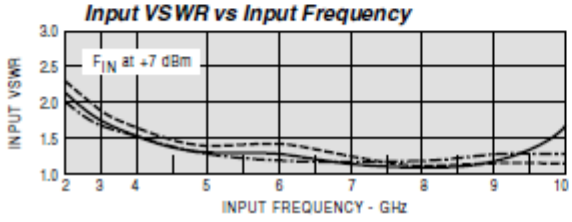

Conversion Loss vs Input Power

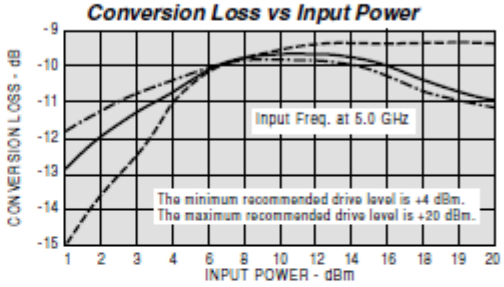

3rd Harm. Suppression vs Input Freq.[1]

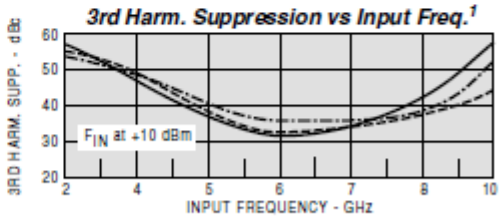

3rd Harm. Suppression vs Input Freq.[1]

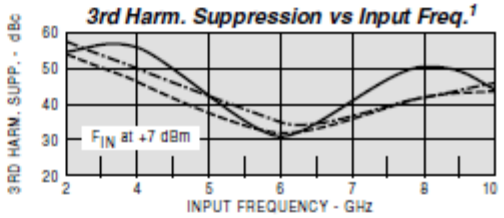

5th Harm. Suppression vs Input Freq.[1]

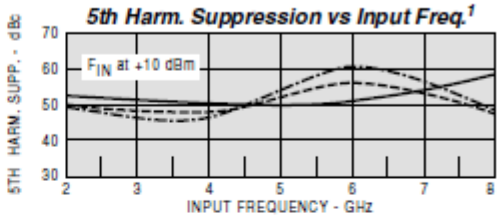

5th Harm. Suppression vs Input Freq.[1]

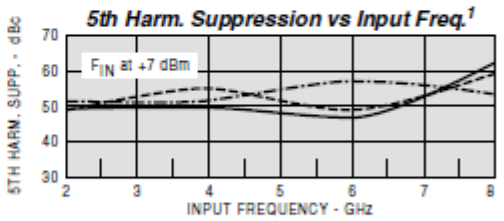

Power Amplifier by AML-Microsemi:

Model Number	Frequency Range (GHz)	Gain (dB min)	Flatness (±dB max)	Noise Figure (dB max)	P-1dB (dBm min)	IP3 (dBm typ)	VSWR In/Out (nom)	DC Current (mA nom)	Outline
AML618P2301	6.0 - 18.0	22 - 26	1.5	7	30	37	2.0:1	1075	SP10

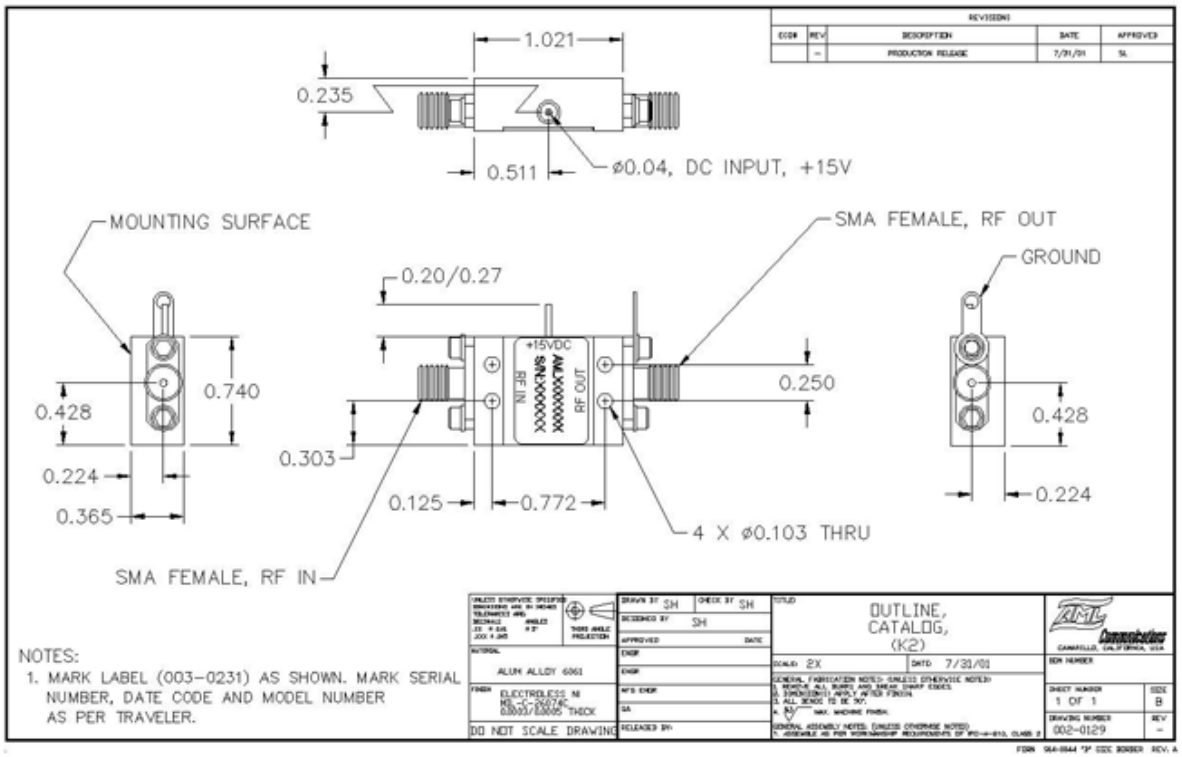

Power Amplifier model n. A2CP18629, by Teledyne Cougar:

TELEDYNE COUGAR
A Teledyne Technologies Company

Typical and guaranteed specifications vary versus frequency; see detailed data sheets for specification variations.

High Performance Amplifiers

Typical and Guaranteed Specifications—50 Ω System

Model	Frequency Range GHz	Small Signal Gain dB			Gain Flatness ±dB		Noise Figure dB			Power Output At 1dB Compression dBm			Rev. Iso. dB	Intercept Point dBm	SWR In/Out		D.C.	
		Typ.	Min. 0/50C	Min. -55/85C	Max. 0/50C	Max. -55/85C	Typ.	Max. 0/50C	Max. -55/85C	Typ.	Min. 0/50C	Min. -55/85C	Typ.	3rd/2nd Typ.	Max. 0/50C	Max. -55/85C	Volts Nom.	mA Typ.
A2CP18629	6.0-18.0	15.0	13.5	12.5	1.5	1.5	4.5	6.5	7.0	28.5	27.0	26.0	35	36/45	2.0	2.0	12	350

Directional Coupler CD-602-183-20S-R by Miteq:

Model: CD-602-183-10S-R

Add To Quote

Description

Coupler

Features

Uni-directional	✔
ROHS	✔

Frequency Range

Frequency Minimum	6000 (MHz)
Frequency Max	18000 (MHz)

Electrical Specifications

Coupling	10 (db)
Frequency Flatness	1.5 (dB)
Directivity	12 (dB)
Insertion Loss (True)	1.2 (dB)
VSWR Primary	1.4:1 (Ratio)
VSWR Secondary	1.6:1 (Ratio)
Average Power	50 (W)
Peak Power	1 (W)

Temperature Ranges

Specs Guaranteed	25 (°C)
Operating Maximum	-55 to 85 (°C)
Storage Maximum	-65 to 100 (°C)

Humidity

NonCondensing	0

Package Types

Package	Coaxial

Delivery

Delivery	60 Days

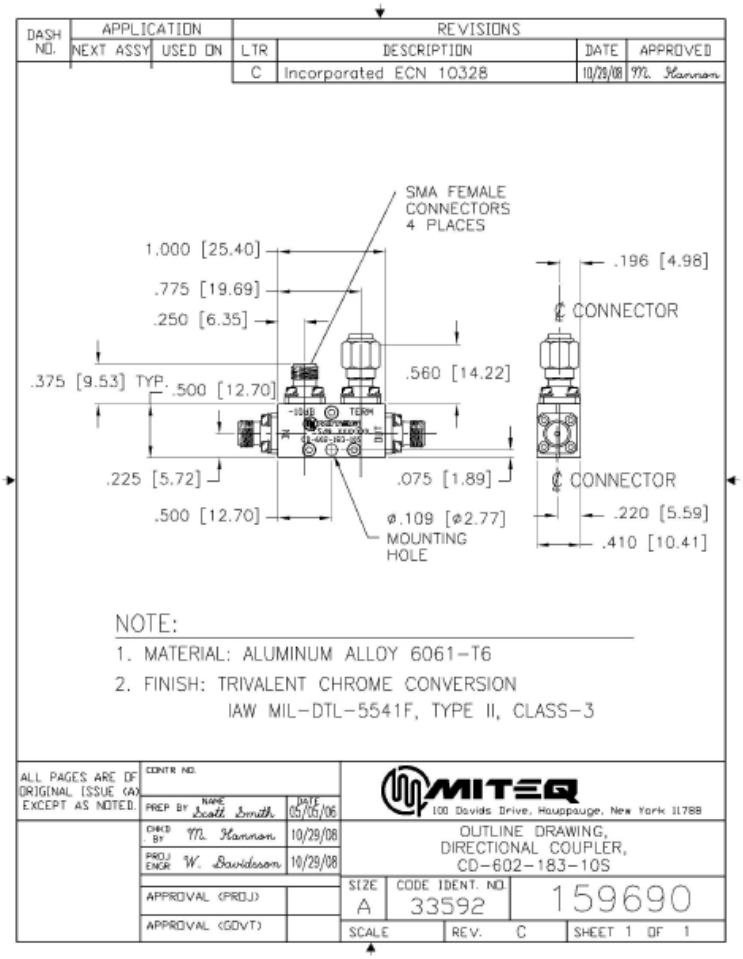

10-way Power Divider, model n. PS10-11, by Microwave Communications Laboratories, Inc.:

10-Way Power Divider and Combiner (PS10 Series)

FEATURES:

- High Isolation, High Reliability
- Low Insertion Loss, Low VSWR
- Ultra Wide band
- Stripline Construction

MODEL NUMBER	FREQUENCY RANGE (GHz)	INSERTION LOSS (dB) Max.	ISOLATION (dB) Min.	VSWR In/Out Max.	AMPLITUDE BALANCE (+/- dB) Max.	POWER AVERAGE (Watts) Load VSWR
PS10-11	6-18	3.8	10	2.00:1/1.90:1	1.9	10@1.20:1

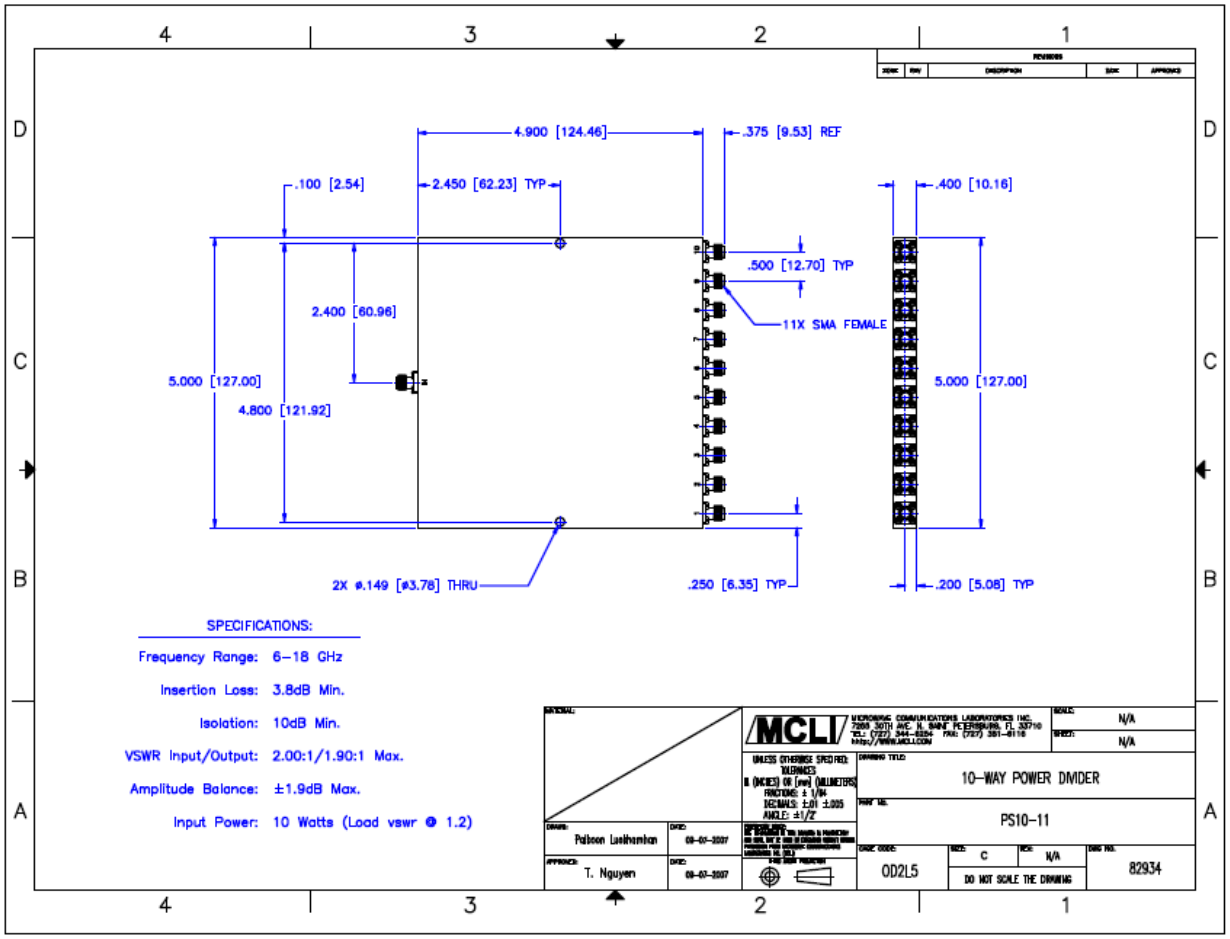

IQ Mixer model n. IRM0618HC2Q, by MITEQ:

6 TO 18 GHz IMAGE REJECTION OR I/Q MIXERS

MODELS: IRM0618LC2A, IRM0618LC2B, IRM0618LC2C AND IRM0618LC2Q

FEATURES

- RF/LO coverage ..... 6 to 18 GHz
- IF operation ..... DC to 0.5 GHz
- Conversion loss..... 9 dB typical
- Image rejection..... 20 dB typical

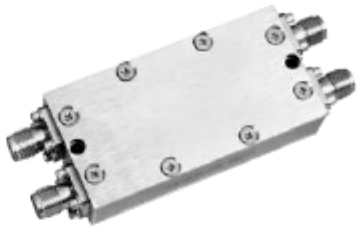

ELECTRICAL SPECIFICATIONS

INPUT PARAMETERS	CONDITION	UNITS	MIN.	TYP.	MAX.
RF frequency range		GHz	6		18
RF VSWR (RF = -10 dBm)		Ratio		2:1	
LO frequency range		GHz	6		18
LO power range	IRM0618LC2 IRM0618MC2 IRM0618HC2	dBm dBm dBm	+10 +13 +17	+12 +15 +18	+13 +16 +20
LO VSWR		Ratio		2.5:1	
TRANSFER CHARACTERISTICS	**CONDITION**	**UNITS**	**MIN.**	**TYP.**	**MAX.**
Conversion loss (Note 1)	RF > LO IRM0618LC2Q	dBm dB		9 12	10 13
Single-sideband noise figure		dB		10.5	
Image rejection (Note 1)	RF < LO	dB	18	20	
LO-to-RF isolation		dB	18	20	
LO-to-IF isolation		dB		20	
Input power at 1 dB compression	IRM0618LC2 IRM0618MC2 IRM0618HC2	dBm dBm dBm		+6 +10 +15	
Input two-tone third-order intercept point	IRM0618LC2 IRM0618MC2 IRM0618HC2	dBm dBm dBm		+16 +20 +25	
Amplitude balance	IRM0618LC2Q	dB			±1.5
Phase balance	IRM0618LC2Q	Degrees			±15
Truth table	IRM0618LC2Q		PORT	RF < LO	RF > LO
			I	0	-90
			Q	-90	0
OUTPUT PARAMETERS	**CONDITION**	**UNITS**	**MIN.**	**TYP.**	**MAX.**
IF frequency (Image rejection mode)	IRM0618LC2A IRM0618LC2B IRM0618LC2C	MHz MHz MHz	20 40 100		40 80 200
IF frequency (QIFM, I/Q demodulator mode)	IRM0618LC2Q	MHz	DC		500
IF VSWR (IF = -10 dBm)		Ratio		1.5:1	

MITEQ 100 Davids Drive, Hauppauge, NY 11788 • TEL: (631) 436-7400 • FAX: (631) 436-7430 • www.miteq.com

IRM0618LC2C TYPICAL TEST DATA

VSWR
(LO = +10 dBm)

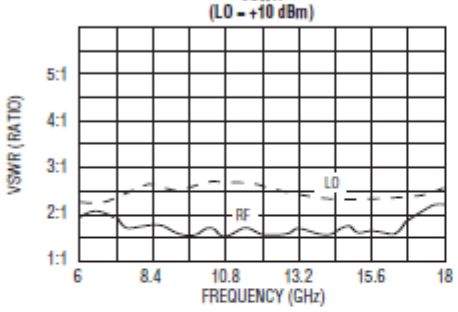

IMAGE REJECTION/CONVERSION LOSS
(LO = +10 dBm/IF = 150 MHz)

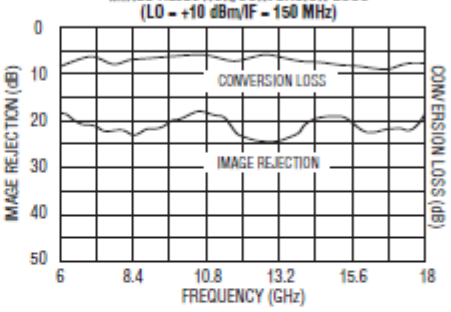

AMPLITUDE AND PHASE BALANCE
(I/Q, LO = +10 dBm)

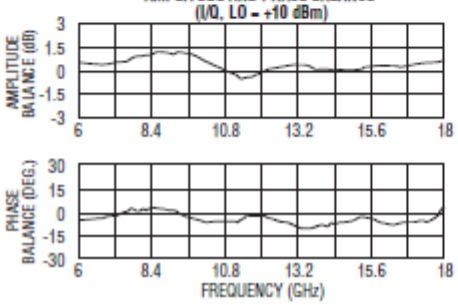

LO-TO-RF ISOLATION
(LO = +10 dBm)

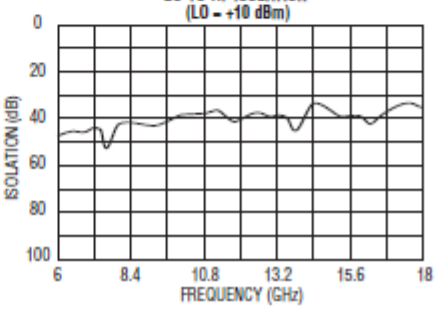

MAXIMUM RATINGS

Specification temperature..... +25°C
Operating temperature ..... -54 to +85°C
Storage temperature ..... -65 to +125°C

GENERAL NOTES

1. Standard catalog unit aligned and tested for guaranteed RF > LO performance. RF < LO guaranteed performance is available, please contact MITEQ.
2. For upconverter applications, please order Model Number SSM0618 Series. See Modulator section of catalog.

NOTE: Test data supplied at 25°C; conversion loss, LO-to-RF isolation, image rejection (IF Options A, B and C), phase and amplitude balance (IF Option Q).

OUTLINE DRAWINGS

IRM0618LC2A, B and C

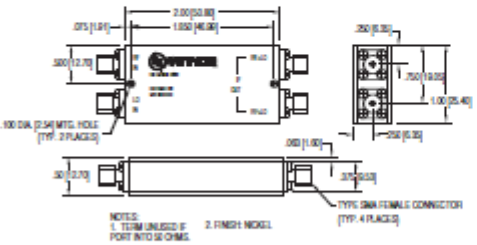

IMAGE REJECTION

IRM0618LC2Q

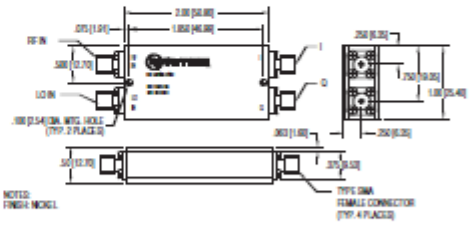

QIFM, I/Q DEMODULATOR

NOTE: All dimensions shown in brackets [ ] are in millimeters.

MITEQ 100 Davids Drive, Hauppauge, NY 11788 • TEL: (631) 436-7400 • FAX: (631) 436-7430 • www.miteq.com

Low Noise Amplifier, model n. CBL06182825, by Cernex, Inc.:

CERNEX, Inc.

Broadband Low Noise Amplifiers

FEATURES:

- Coverage From 0.01 to 110.0 GHz (Octave/Multioctave)
- Noise Figure As Low As 1.5 dB
- Wide Dynamic Range
- Compact/Rugged Thin-Film Construction
- Economically Priced

DESCRIPTION:

CBL Series

Cernex's CBL series are general purpose amplifiers suitable for a wide range of applications in commercial and military systems where low to high gain block amplifiers are required. CBL series are compact, rugged, and may be designed into commercial and military systems where stringent environments are encountered.

SPECIFICATIONS:

Model Number	Frequency Range (GHz)	Gain (dB) Min.	SS Flatness (+/-dB) Max.	NF (dB) Max.	P1dB (dBm) Min.	VSWR In/Out Max.	Current @ 12-15 VDC (mA) Typ.	Case Type
CBL06182825	6-18	28	1.50	2.50	15	2:1	200	HN4 ▲

SP6T Switch by G.T. Microwave:

G.T Microwave Features:

Frequency Ranges: From 100 MHz to 24 GHz any optimized bandwidth is available.

TTL Compatible Logic: Logic '1' = Isolation and Logic '0' = Insertion Loss. For switches without TTL driver, +1VDC @ +50mA = Isolation and -1VDC @ -50mA = Insertion Loss. For logic options, please consult factory.

High Speed Switching: Switches listed are measured from 50% TTL to 10% / 90% RF.

Low DC Power Consumption: Switches with TTL drivers require ± 5VDC @ +250/ -75mA

High RF Power Handling: For power levels greater than listed please consult factory.

Absorptive Switches: On these models the J2 – J7 ports are NON-REFLECTIVE.

Standard Interfaces: RF port connectors are 'SMA' , female per MIL-C-39012. DC/LOGIC connections are solder terminals. Call factory for optional connectors.

Matched Phase & Amplitude: Models listed are available with matched ports. Otherwise add .25 dB loss to ports J2 & J7.

Electrical Specifications for REFLECTIVE and ABSORPTIVE switches – SP6T

FREQ. RANGE GHz	ISOLATION dB	INSERTION LOSS dB & SWITCHING SPEED			INSERTION LOSS dB & SWITCHING SPEED			INSERTION LOSS dB & SWITCHING SPEED			V.S.W.R. MAX	INPUT POWER WATTS	
		REFL	ABSP	uSEC	REFL	ABSP	nSEC	REFL	ABSP	nSEC		TYP	MAX
6.0-18.0	30	2.4	2.8	1.0	2.6	3.0	100	2.7	3.1	30	2.0:1	0.2	1.0
	60	2.6	3.0		2.8	3.2		2.9	3.3				
	80	2.8	3.2		3.0	3.4		3.1	3.5				

SP10T Switch by Herley Microwave:

Model 2553-B39 SP10T Switch Specifications

PERFORMANCE SPECIFICATIONS

CHARACTERISTIC	FREQUENCY RANGE (GHz)	
	6.0 to 12.0	12.0 to 18.0
Min. Isolation (dB)	70	70
Max. Insertion Loss (dB)	4.3	5.6
Max. VSWR one port ON	2.0:1	2.0:1
Max. VSWR OFF	2.2:1	2.2:1

Amplitude Matching
(between ports) .....±1.2 dB

Phase Matching
(between ports)..... ±30°

Switching Time
ON Time.....700 nsec max.
OFF Time.....700 nsec max.

Power Handling Capability
Without Performance
Degradation.....600 mW cw or peak
Survival Power .....1.5W cw

Power Supply Requirements

+5V ±5%, 350 mA max
–12V ±5%, 100 mA max

Control Characteristics

Control Input
Impedance .....Schottky TTL, two unit loads. (A unit load is 2 mA sink current and 50 µA source current.)

Control logic .....Logic "0" (–0.3 to +0.8V) for "ON" state. Logic "1" (+2.0 to +5.0V) for "OFF" state.

Operating Temperature.....0°C to +70°C

List of Acronyms

ADC: Analog-to-Digital Converter

ADS: Advanced Design System.

AM: Amplitude Modulation.

ATOM: Airport detection and Tracking Of dangerous Materials by passive and active sensors arrays.

BPF: Band-Pass Filter.

CW: Continuous Wave.

DUCAT: Delft University Chamber for Antenna Tests.

EEMCS: Electrical Engineering, Mathematics, and Computer Engineering.

EIRP: Equivalent Isotropic Radiated Power.

FFC: Federal Communications Commission.

FM: Frequency Modulation.

FMCW: Frequency Modulated Continuous Wave.

LO: Local Oscillator.

LPF: Low-Pass Filter.

MIMO: Multiple Input Multiple Output.

MMW: MilliMeter Wave

MTS-R: Microwave Technology and Systems for Radar.

PSD: Power Spectral Density.

RAR: Real Aperture Radar.

RCS: Radar Cross Section.

RF: Radar Frequency.

SAR: Synthetic Aperture Radar.

SFCW: Stepped Frequency Continuous Wave.

SNR: Signal-to-Noise Ratio.

UWB: Ultra Wide-Band.

VCO: Voltage Controlled Oscillator.

YIG: Yttrium Iron Garnet.

YTO: YIG-tuned Oscillator.